SEARCH FOR MSSM HIGGS BOSON PRODUCTION IN $p\bar{p}$ COLLISIONS AT $\sqrt{s} = 1.96$ TeV, WITH A HIGGS DECAYING INTO τ's

A Dissertation

Submitted to the Graduate School

of the University of Notre Dame

in Partial Fulfillment of the Requirements

for the Degree of

Doctor of Philosophy

by

Peter Svoisky, M.S.

Anna Goussiou, Director

Randal Ruchti, Director

Graduate Program in Physics

Notre Dame, Indiana

April 2008

© Copyright by

PETER V. SVOISKY

2008

All rights reserved

SEARCH FOR MSSM HIGGS BOSON PRODUCTION IN $p\bar{p}$ COLLISIONS AT $\sqrt{s} = 1.96$ TeV, WITH A HIGGS DECAYING INTO τ's

Abstract

by

Peter Svoisky

We present a search for the production of neutral Higgs bosons in association with bottom quarks in $p\bar{p}$ collisions at $\sqrt{s} = 1.96$ TeV. The cross section for this process is enhanced in many extensions of the Standard Model (SM), such as in its Minimal Supersymmetric extension (MSSM) at large tan β. The data, corresponding to a recorded integrated luminosity of 1 fb^{-1}, were collected with the DØ detector at the Fermilab Tevatron Collider. In the absense of a signal a 95% C.L. limit is set on the production cross section times branching ratio, and the results are also interpreted in the MSSM.

To my parents

"Knowledge is power", but to a degree only. Its possession per se will raise a man to mediocrity, but not to distinction.

G. S. Patton, Jr., Major

The Secret of Victory

March 26, 1926

CONTENTS

FIGURES vi

TABLES xiii

ACKNOWLEDGMENTS xv

CHAPTER 1: INTRODUCTION 1

CHAPTER 2: THEORY 5
2.1 Standard Model Electroweak Symmetry Breaking 5
2.2 Supersymmetry 9

CHAPTER 3: THE EXPERIMENTAL APPARATUS 17
3.1 The Fermilab Accelerators 17
3.1.1 The Pre-accelerator 18
3.1.2 The Linac 19
3.1.3 The Booster Synchrotron 20
3.1.4 The Main Injector 21
3.1.5 The Anti-proton Source 21
3.1.6 The Recycler 22
3.2 The Run II DØ Detector 23
3.2.1 Luminosity monitor 24
3.2.2 Tracking System 25
3.2.3 Preshowers 28
3.2.4 Calorimetry 30
3.2.5 Muon System 34
3.2.6 Trigger System and Data Acquision 38

CHAPTER 4: ANALYSIS 41
4.1 Reconstruction of Physics Objects at DØ 41
4.1.1 Luminosity 42
4.1.2 Tracking and Primary Vertexing 43

4.1.3 Calorimeter Energy Clusters 47
4.1.4 Reconstruction of Electromagnetic Objects 49
4.1.5 Muon Reconstruction 50
4.1.6 Jet Reconstruction 54
4.1.7 B-quark identification 60
4.1.8 τ Recontstruction 64
4.1.9 Missing Transverse Energy 69
4.2 Event Samples 74
4.2.1 Data Sample 75
4.2.2 Monte Carlo Samples 75
4.3 Trigger 76
4.4 Object Identification and Selection 77
4.4.1 Muons 77
4.4.2 Hadronic Taus 77
4.4.3 Jets 80
4.4.4 B-tagging 80
4.4.5 Preselection 80
4.5 Backgrounds 81
4.5.1 W+jets estimation 81
4.5.2 $Z + jets \rightarrow \mu^+\mu^- + jets$ estimation from Monte Carlo 86
4.5.3 QCD estimation 86
4.5.4 $Z + jets \rightarrow \tau^+\tau^- + jets$ estimation from Monte Carlo 97
4.5.5 $Z + jets \rightarrow ll + jets$ estimation from data 103
4.5.6 $t\bar{t}$ background 105
4.6 Monte Carlo cross check. Event Kinematic Distributions. 111
4.7 Systematic Uncertainties 121

CHAPTER 5: EXPERIMENTAL RESULTS 123
5.1 Final Selection and Results 123
5.1.1 Event Cut Flow 128
5.2 Interpretation within the MSSM framework 136

CHAPTER 6: CONCLUSIONS 138

BIBLIOGRAPHY 142

FIGURES

1.1 Standard model building blocks. Adapted from [2]. 3

2.1 Cross section of the Standard Model Higgs boson production at the Fermilab Tevatron. Adapted from [1]. 7

2.2 Branching ratios of the Standard Model Higgs boson decay. Adapted from [1] 8

2.3 The lower [4] and the upper [5] Higgs mass bounds as a function of the energy scale Λ at which the Standard Model breaks down, assuming $M_t = 175$ GeV and $\alpha_s(m_Z) = 0.118$. The shaded areas above reflect the theoretical uncertainties in the calculations of the Higgs mass bounds. This figure is taken from [6]. 9

2.4 Lightest CP-even Higgs mass m_h, heaviest CP-even Higgs mass m_H and charged Higgs mass (mH) as a function of mA for two choices of $\tan\beta = 3$ and $\tan\beta = 30$. 11

2.5 Leading-Order Feynmann diagrams for neutral Higgs boson production in associated with b-quarks in the 4-flavor scheme. Adapted from [10] 13

2.6 Leading-Order Feynmann diagrams for neutral Higgs boson production in associated with b-quarks in the 5-flavor scheme. Adapted from [10] 13

2.7 Production crosssections for neutral CP-even Higgs bosons h, H in MSSM, for $\tan\beta = 6$ (left) and $\tan\beta = 30$ (right). Adapted from [1] . 14

2.8 Production crosssections for neutral CP-odd Higgs boson A in MSSM, for $\tan\beta = 6$ (left) and $\tan\beta = 30$ (right). Adapted from [1]. 14

2.9 Widths of the neutral Higgs bosons at $\tan\beta = 60$ GeV. A is solid, h is dashed, and H is dotted. Adapted from [9]. 15

2.10 Branching ratios of the MSSM neutral CP-even Higgs bosons h and H decay at $\tan\beta = 6$ (left) and $\tan\beta = 30$ (right). Adapted from [1]. 15

2.11 Branching ratios of the MSSM neutral CP-odd Higgs boson A decay at $\tan\beta = 6$ (left) and $\tan\beta = 30$ (right). Adapted from [1]. 16

3.1 The Fermilab accelerator complex. Adapted from [9]. 19

3.2 Schematic view of H^- source operation principle. Adapted from [2]. . 20

3.3 Schematic of Linac operation principle. Adapted from [2]. 21

3.4 Schematic of $\bar{p}$ production. Adapted from [2]. 22

3.5 The upgraded DØ detector. Adapted from [9]. 24

3.6 Tracking detectors, preshowers, and luminosity monitor (Level 0). Adapted from [9]. 25

3.7 Silicon microstrip detector. Adapted from [17]. 26

3.8 Central Fiber Tracker. Adapted from [2]. 27

3.9 Preshower detectors. Adapted from [2]. 29

3.10 DØ calorimeter. Adapted from [2]. 31

3.11 Schematic view of a portion of the DØ calorimeters showing the transverse and longitudinal segmentation pattern. The shading pattern indicates cells grouped together for signal readout. The rays indicate pseudorapidity intervals from the center of the detector. Adapted from [16]. 32

3.12 Calorimeter unit cell. Adapted from [16]. 33

3.13 Schematic of the calorimeter readout electronics. Adapted from [16]. . 34

3.14 The DØ Muon System. Adapted from [9]. 35

3.15 The DØ Muon System, PDT and MDT. Adapted from [16]. 36

3.16 The DØ Muon System, Scintillators, Cosmic Cap, Bottom counters. Adapted from [16]. 37

3.17 Schematic of the DØ trigger and data acquisition systems. Adapted from [16]. 39

3.18 Block diagram of DØ L1 and L2 trigger systems. Adapted from [16]. 40

4.1 The Hough transform, used by the HTF track reconstruction algorithm, applied to a toy simulation of a single 1.5 GeV track coming from the center of the detector. a) shows the family of trajectories (circular arcs) through a given hit. b) shows the line in Hough transformed space corresponding to the locus of points which corresponds to each trajectory through the given hit. c) shows the family of lines corresponding to each of the five hits on the single 1.5 GeV simulated track. d) shows the histogram of the 5 Hough transformed hits. The peak in the histogram corresponds to the parameters (curvature and angle) of the original 1.5 GeV simulated track. Adapted from [9]. . . 45

4.2 An axial view (looking down the beam-pipe) of an event recorded with the DØ inner trackers, showing the reconstructed hits and tracks. The CFT hits are square and form the 8 layers on the outside. Silicon hits are drawn as small circles, and are innermost. Hits are colored solid if they are associated with a reconstructed track. The tracks are shown as solid lines, and are curved by the solenoidal magnetic field pointing out of the page. Adapted from [9]. 48

4.3 Muon reconstruction correction factor as a function of muon detector η and ϕ. Adapted from [30]. 52

4.4 Muon track reconstruction correction factor as a range of the track z-position. Adapted from [30]. 53

4.5 Evolution of a parton coming from a hard scattering process into a jet in the calorimeter. Adapted from [30]. 55

4.6 Offset energy correction for different primary vertex multiplicities as a function of the jet detector pseudorapidity. Adapted from [30]. . . . 57

4.7 Non-uniformity correction in data as a function of jet detector pseudorapidity. Adapted from [30]. 57

4.8 Absolute response correction in data after offset and relative response corrections as a function of partially-corrected jet energy. Adapted from [30]. 58

4.9 Schematic illustration of the MPF method. Adapted from [30]. 59

4.10 Showering correction in data as a function of corrected jet transverse energy. Adapted from [30]. 60

4.11 The jet correction factor for the measured muon energy associated with a jet. The fraction of the muon energy to add back to the jet is derived from simulated bjets containing muons. The correction factor is shown for low (< 50 GeV) and high (> 50 GeV) energy jets and the inclusive jet sample. Adapted from [9]. 61

4.12 Fractional jet energy scale uncertainties as a function of uncorrected jet transverse energy, plotted for three different pseudorapidity values.Adapted from [30]. 62

4.13 A schematic illustration of b-jet parameters. 63

4.14 A schematic of the three types of taus. Adapted from [30]. 67

4.15 NN_τvariables for type 1. Red histograms are the $Z \to \tau^+\tau^-$ Monte Carlo, green are the anti-isolated muon data. 70

4.16 NN_τvariables for type 2. Red histograms are the $Z \to \tau^+\tau^-$ Monte Carlo, green are the anti-isolated muon data. 71

4.17 NN_τvariables for type 3. Red histograms are the $Z \to \tau^+\tau^-$ Monte Carlo, green are the anti-isolated muon data. 72

4.18 NN_τoutput for the three τ types. Red histograms are the $Z \to \tau^+\tau^-$ Monte Carlo, green are the anti-isolated muon data. 73

4.19 μ-$\not{E}_T$transverse mass (Wmass) for the three τ-types (top left - type 1, top right - type 2, bottom left - type 3, and bottom right - all types) before the normalization. 82

4.20 Jet multiplicity for the three τ-types (top left - type 1, top right - type 2, bottom left - type 3, and bottom right - all types) before the normalization. 83

4.21 μ-$\not{E}_T$transverse mass (Wmass) for the three τ-types (top left - type 1, top right - type 2, bottom left - type 3, and bottom right - all types) after the normalization. 84

4.22 Jet multiplicity for the three τ-types (top left - type 1, top right - type 2, bottom left - type 3, and bottom right - all types) after the normalization. 85

4.23 μ, $\sum \tau_{pT}^{trk}$ invariant mass (Zmass) for the three τ-types (top left - type 1, top right - type 2, bottom left - type 3, and bottom right - all types) before the normalization. 87

4.24 Jet multiplicity for the three τ-types (top left - type 1, top right - type 2, bottom left - type 3, and bottom right - all types) before the normalization. 88

4.25 μ, $\sum \tau_{pT}^{trk}$ invariant mass (Zmass) for the three τ-types (top left - type 1, top right - type 2, bottom left - type 3, and bottom right - all types) after the normalization. 89

4.26 Jet multiplicity for the three τ-types (top left - type 1, top right - type 2, bottom left - type 3, and bottom right - all types) after the normalization. 90

4.27 μ track isolation vs. $NN_\tau$for the SS events in data. 92

4.28 NN_τdistributions with muon isolation applied and an isolated jet required, for the three τ-types (top left - type 1, top right - type 2, bottom left - type 3, and bottom right - all types). QCD is represented by SS events. 93

4.29 Muon track isolation distributions with $minNN_\tau$ cuts applied and an isolated jet required, for the three τ-types (top left - type 1, top right - type 2, bottom left - type 3, and bottom right - all types). QCD is represented by SS events corrected for the τ fake rate. 94

4.30 Muon track isolation distributions with $minNN_\tau$ cuts applied and a NN_TIGHT b-tag required, for the three τ-types (top left - type 1, top right - type 2, bottom left - type 3, and bottom right - all types). QCD is represented by SS events corrected by all three rates. Signal with Higgs mass 150 GeV is shown in red. 96

4.31 Muon, τ and $\not{E}_T$ invariant mass (visible mass) with reference final selection cuts, Sec. 4.4, without requiring an extra isolated jet for the three τ-types (top left - type 1, top right - type 2, bottom left - type 3, and bottom right - all types) before the normalization. 98

4.32 Isolated jet multiplicity with reference final selection cuts, Sec. 4.4, for the three τ-types (top left - type 1, top right - type 2, bottom left - type 3, and bottom right - all types) before the normalization. . . . 99

4.33 Muon, τ and $\not{E}_T$ invariant mass (visible mass) with reference final selection cuts, Sec. 4.4, without requiring an extra isolated jet for the three τ-types (top left - type 1, top right - type 2, bottom left - type 3, and bottom right - all types) after the normalization. 100

4.34 Isolated jet multiplicity with reference final selection cuts, Sec. 4.4, for the three τ-types (top left - type 1, top right - type 2, bottom left - type 3, and bottom right - all types) after the normalization. 101

4.35 Muon p_T, with reference cuts, without requiring an extra isolated jet for the three τ-types (top left - type 1, top right - type 2, bottom left - type 3, and bottom right - all types). $Z \to \tau^+\tau^-$ background is simulated with PYTHIA. 102

4.36 μ, τ, and $\not{E}_T$ invariant mass (visible mass) with reference final selection cuts and NN_TIGHT b-tag, for the three τ-types (top left - type 1, top right - type 2, bottom left - type 3, and bottom right - all types).104

4.37 KNN variable HT with reference final selection cuts and $\Delta\phi(\mu,\tau) > 0.5$ cut, Sec. 4.4, with a NN_TIGHT b-tag for the three τ-types (top left - type 1, top right - type 2, bottom left - type 3, and bottom right - all types). Signal with Higgs mass 150 GeV is shown in red. 106

4.38 KNN variable MHT with reference final selection cuts and $\Delta\phi(\mu,\tau) > 0.5$ cut, Sec. 4.4, with a NN_TIGHT b-tag for the three τ-types (top left - type 1, top right - type 2, bottom left - type 3, and bottom right - all types). Signal with Higgs mass 150 GeV is shown in red. 107

4.39 KNN variable Njet with reference final selection cuts and $\Delta\phi(\mu,\tau) > 0.5$ cut, Sec. 4.4, with a NN_TIGHT b-tag for the three τ-types (top left - type 1, top right - type 2, bottom left - type 3, and bottom right - all types). Signal with Higgs mass 150 GeV is shown in red. 108

4.40 KNN variable mutau_dphi with reference final selection cuts and $\Delta\phi(\mu,\tau) > 0.5$ cut, Sec. 4.4, with a NN_TIGHT b-tag for the three τ-types (top left - type 1, top right - type 2, bottom left - type 3, and bottom right - all types). Signal with Higgs mass 150 GeV is shown in red. 109

4.41 KNN output with reference final selection cuts and $\Delta\phi(\mu,\tau) > 0.5$ cut, Sec. 4.4, with a NN_TIGHT b-tag for the three τ-types (top left - type 1, top right - type 2, bottom left - type 3, and bottom right - all types). Signal with Higgs mass 150 GeV is shown in red. 110

4.42 p_T^μ with reference final selection cuts, without requiring an extra isolated jet, for the three τ-types (top left - type 1, top right - type 2, bottom left - type 3, and bottom right - all types). 111

4.43 muon det η with reference final selection cuts, without requiring an extra isolated jet, for the three τ-types (top left - type 1, top right - type 2, bottom left - type 3, and bottom right - all types). 112

4.44 muon ϕ with reference final selection cuts, without requiring an extra isolated jet, for the three τ-types (top left - type 1, top right - type 2, bottom left - type 3, and bottom right - all types). Color code is the same as in Fig. 4.43 113

4.45 p_T^τ with reference final selection cuts, without requiring an extra isolated jet, for the three τ-types (top left - type 1, top right - type 2, bottom left - type 3, and bottom right - all types). 114

4.46 τ det η with reference final selection cuts, without requiring an extra isolated jet, for the three τ-types (top left - type 1, top right - type 2, bottom left - type 3, and bottom right - all types). 115

4.47 τ ϕ with reference final selection cuts, without requiring an extra isolated jet, for the three τ-types (top left - type 1, top right - type 2, bottom left - type 3, and bottom right - all types). Color code is the same as in Fig. 4.46 116

4.48 $\not{E}_T$ with reference final selection cuts, without requiring an extra isolated jet, for the three τ-types (top left - type 1, top right - type 2, bottom left - type 3, and bottom right - all types). 117

4.49 Leading isolated taggable jet p_T with reference final selection cuts, for the three τ-types (top left - type 1, top right - type 2, bottom left - type 3, and bottom right - all types). 118

4.50 Leading isolated taggable jet $det\eta$ with reference final selection cuts, for the three τ-types (top left - type 1, top right - type 2, bottom left - type 3, and bottom right - all types). 119

4.51 Leading isolated taggable jet ϕ with reference final selection cuts, for the three τ-types (top left - type 1, top right - type 2, bottom left - type 3, and bottom right - all types). 120

5.1 μ, τ, and $\not{E}_T$ invariant mass (visible mass) with reference final selection cuts, for the three τ-types (top left - type 1, top right - type 2, bottom left - type 3, and bottom right - all types). 124

5.2 μ, τ, and $\not{E}_T$ invariant mass (visible mass) with reference final selection cuts, for the three τ-types (top left - type 1, top right - type 2, bottom left - type 3, and bottom right - all types). $Z{+}jets \rightarrow ll{+}jets$ background is estimated normalizing to data in the no signal hypothesis. 125

5.3 μ, τ, and $\not{E}_T$ invariant mass (visible mass) with reference final selection cuts, NN_TIGHT b-tag, and KNN cut 0.6, where all backgrounds are estimated from MC, for the three τ-types (top left - type 1, top right - type 2, bottom left - type 3, and bottom right - all types). . . 126

5.4 μ, τ, and $\not{E}_T$ invariant mass (visible mass) with reference final selection cuts, NN_TIGHT b-tag, and KNN cut 0.6, where $Z + jets \rightarrow ll + jets$ background is estimated from data, for the three τ-types (top left - type 1, top right - type 2, bottom left - type 3, and bottom right - all types). 127

5.5 Limits on the $bg \rightarrow b(h/H/A) \rightarrow b\tau^+\tau^-$ production times branching ratio as a function of the Higgs mass. 135

5.6 Excluded region in the $(m_A, \tan\beta)$ plane for the m_h^{max} (left) and the no-mixing (right) scenario of the MSSM, for $\mu = +200$ GeV and $\mu = -200$ GeV. Also shown is the region excluded by the LEP experiments. 137

TABLES

4.1 INPUT VARIABLES FOR THE NEURAL-NETWORK B-TAGGING ALGORITHM. 63

4.2 τ DECAY BRANCHING RATIOS [20]. 65

4.3 NN_τINPUT VARIABLES USED FOR EACH τ TYPE. 74

4.4 PYTHIA MC SIGNAL AND BACKGROUND SAMPLES. 76

4.5 INTEGRATED LUMINOSITY RECORDED WITH DIFFERENT TRIGGER VERSIONS. 78

4.6 $W + jets$ JET MULTIPLICITY SCALE FACTORS. QUOTED UNCERTAINTIES ARE STATISTICAL. 83

4.7 $Z + jets \rightarrow \mu\mu + jets$ JET MULTIPLICITY SCALE FACTORS. QUOTED UNCERTAINTIES ARE STATISTICAL. 87

4.8 OS VS SS ASYMMETRY AND B-TAGGING RATE IN THE QCD DATA SAMPLE. QUOTED UNCERTAINTIES ARE STATISTICAL AS PER BIN IN FIGURE 4.29. 95

4.9 $Z + jets \rightarrow \tau^+\tau^- + jets$ JET MULTIPLICITY SCALE FACTORS. QUOTED UNCERTAINTIES ARE STATISTICAL. 97

4.10 RELATIVE SYSTEMATIC UNCERTAINTIES (IN %) ON THE NUMBER OF SIGNAL AND BACKGROUND EVENTS. 122

5.1 DATA AND MC CUT FLOW TABLE FOR τ TYPE 1 128

5.2 DATA AND MC CUT FLOW TABLE FOR τ TYPE 2 129

5.3 DATA AND MC CUT FLOW TABLE FOR τ TYPE 3 129

5.4 OPTIMAL CUTS FOR THE 95% C.L. CROSS SECTION TIMES BRANCHING RATIO LIMIT CALCULATION 131

5.5 τ TYPE 1 SIGNAL ACCEPTANCES AND EVENT YIELDS FOR DIFFERENT HIGGS MASSES. THE EXPECTED SIGNAL IS NORMALIZED TO THE EXPECTED CROSS SECTION AT 95% C.L. LIMIT. QUOTED UNCERTAINTIES REPRESENT STATISTICAL AND SYSTEMATIC ADDED IN QUADRATURE 132

5.6 τ TYPE 2 SIGNAL ACCEPTANCES AND EVENT YIELDS FOR DIFFERENT HIGGS MASSES. THE EXPECTED SIGNAL IS NORMALIZED TO THE EXPECTED CROSS SECTION AT 95% C.L. LIMIT. QUOTED UNCERTAINTIES REPRESENT STATISTICAL AND SYSTEMATIC ADDED IN QUADRATURE 133

5.7 τ TYPE 3 SIGNAL ACCEPTANCES AND EVENT YIELDS FOR DIFFERENT HIGGS MASSES. THE EXPECTED SIGNAL IS NORMALIZED TO THE EXPECTED CROSS SECTION AT 95% C.L. LIMIT. QUOTED UNCERTAINTIES REPRESENT STATISTICAL AND SYSTEMATIC ADDED IN QUADRATURE 134

ACKNOWLEDGMENTS

I want to thank Professors Anna Goussiou and Randal Ruchti for their invaluable support and patience with me during my stay with the University of Notre Dame High Energy Physics Group.

CHAPTER 1

INTRODUCTION

Physics tries to understand the fundamental concepts underlying the existence of the observable world. It gives us immensely powerful analytical tools to explain a lot of the phenomena that humankind has had access to throughout its history. Particle physics is one of them. What we observe in nature has been proven to be the cumulative effect of micro-particle interactions that could be broken down into a few fundamental forces: the strong force, electroweak force, and gravity. However, this powerful tool has until now failed to unfold some of the mysteries natural sciences face today. It has yet to explain massiveness of the fermionic particles from the first principles, which allows existence of different particle generations and formation of stable systems like atoms. It also has to explain the relationship between fundamental interactions and the emergence of the gravitational force between massive bodies.

Strong and electroweak interactions, together with the observed particles, constitute one of physics biggest successes - the Standard Model (SM). It classifies particles into similarly structured groups called generations. It describes particles and interactions between them in terms of a gauge field theory, which allows us to write down all interactions as minimal couplings of fermions to bosonic gauge fields.

The Standard Model identifies fermionic particles (with spin 1/2) participating in both the strong and electroweak interactions - quarks, and those that interact only

electroweakly - leptons. The gauge force bosonic (spin 1) mediators are represented by 8 types of gluons for the strong interaction and 4 types of electroweak bosons. Building blocks of the Standard Model are graphically shown in the Figure 1.1. The whole system of these particles obeys $SU(3)_C \otimes SU(2)_L \otimes U(1)_Y$ group symmetry, where $SU(3)_C$ is an exact symmetry responsible for the strong interaction (C stands for color), and $SU(2)_L \otimes U(1)_Y$ is believed to be spontaneously broken under normal conditions through the Higgs Mechanism (L stands for weak isospin, and Y for hypercharge). Had it been preserved, the weak interaction would have appeared long-range which would contradict the experimental data. The Higgs Mechanism also makes electroweak bosons, $W^{\pm}$ and Z, massive. It predicts the existence of a spin 0 scalar particle called the Higgs Boson, which couples to fermions and gauge bosons through Yukawa couplings. The electroweak symmetry is also believed to be restored at energies of the order of 1 TeV.

The Standard Model is remarkably well-confirmed by experimental measurements; however there are minor flaws. First of all, the Higgs field has not been discovered yet; secondly, its existence introduces a hierarchy problem. For example, it is manifested through a delicate cancellation between radiative corrections and the bare mass of the Higgs. The radiative corrections bring in terms proportional to a large cut off scale which may be as large as the Plank scale (10^{19} GeV). To maintain the scale of the electroweak symmetry breaking at the order of 1 TeV, the parameters of the theory have to be extremely finely tuned.

One of the solutions to the hierarchy problem is proposed in the form of Supersymmetry. This theory suggests that each particle in the Standard Model has a superpartner (with a spin different from that of its partner by 1/2). It introduces a symmetry between bosons and fermions, which leads to the cancellation of anomalously divergent loop terms in radiative corrections. For example, the cancellation

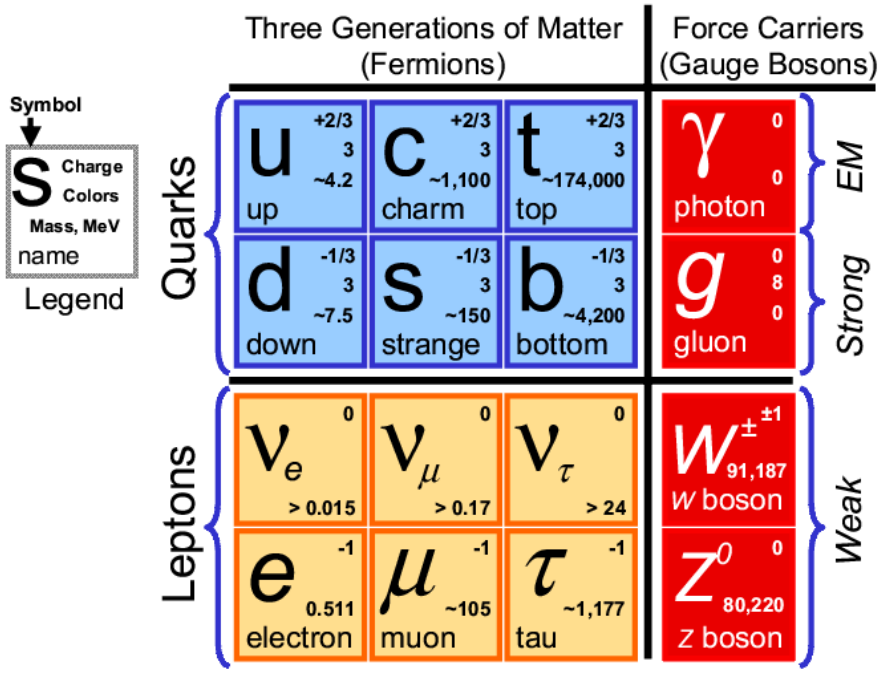

Figure 1.1. Standard model building blocks. Adapted from [2].

of the divergent Higgs loop is realized by adding a fermionic partner to the Higgs boson, the Higgsino.

This thesis describes a search for a Minimally Supersymmetric Standard Model (MSSM) scalar Higgs field. The MSSM opens up an opportunity for the Higgs boson to be discovered at the Fermilab TeVatron collider, although the Standard Model Higgs does not yet seem to be accessible at this experiment. A particular combination of MSSM parameters allows the Higgs boson to couple strongly to b-quarks and enhance the Higgs production cross section in association with b-quarks by 2-3 orders of magnitude compared to the Standard Model.

In Chapter 2, theoretical aspects of the analysis are described; Chapter 3 shows briefly the parts of the TeVatron collider and the DØ Experiment, where this analysis

is done; Chapter 4 discusses the technical aspects of the actual analysis; results are discussed and interpreted within the theoretical model in Chapter 5; and the thesis conclusions are finalized in Chapter 6.

CHAPTER 2

THEORY

2.1 Standard Model Electroweak Symmetry Breaking

The Standard Model Lagrangian (2.1) proposes Electro-Weak Symmetry Breaking (EWSB) by means of a complex scalar doublet Higgs field (denoted by ϕ), which couples to both fermions and electroweak gauge bosons. It acquires a vacuum expectation value (VEV) when the Higgs potential ($V(\phi)$) is minimized. This optimal value lies away from zero (246 GeV) and gives non-zero rest masses.

$$\begin{aligned} L &= \bar{q}\gamma^{\mu}(i\partial_{\mu} - g_s T_a G^a_{\mu})q - \frac{1}{4}G^a_{\mu\nu}G^{\mu\nu}_a \\ &+ \bar{L}\gamma^{\mu}(i\partial_{\mu} - \frac{g}{2}\boldsymbol{\tau}\cdot\boldsymbol{W}_{\mu} - \frac{g'}{2}B_{\mu}Y)L \\ &+ \bar{R}\gamma^{\mu}(i\partial_{\mu} - g'B_{\mu}Y)R \\ &- \frac{1}{4}W_{\mu\nu}W^{\mu\nu} - \frac{1}{4}B_{\mu\nu}B^{\mu\nu} \\ &+ \left|(i\partial_{\mu} - \frac{g}{2}\boldsymbol{\tau}\cdot\boldsymbol{W}_{\mu} - \frac{g'}{2}B_{\mu}Y)\phi\right|^2 - V(\phi) \\ &- G_e(\bar{L}\phi R + \bar{R}\phi^{\dagger}L + h.c.). \end{aligned} \tag{2.1}$$

In (2.1) the first line determines the strong interaction, where T_a are 8 Gell-Mann matrices and G^a_{μ} are the corresponding 8 gluon fields; q are the quark fields. The second, third, and fourth lines describe the electroweak interaction, where L are the left-handed fermion doublets, R are the right-handed fermion singlets, and **W** and B represent the electroweak bosons.

Three degrees of freedom from the Higgs doublet become the longitudinal components of the weak bosons, and the fourth one remains in the physical spectrum and becomes the CP-even scalar Higgs boson. This is only one model of electroweak symmetry breaking. One could also introduce new fermions and new dynamics, in which the Goldstone bosons would be a consequence of the strong binding of the new fermion fields (dynamic symmetry breaking).

The Standard Model Higgs boson could be produced at the Fermilab Tevatron mainly through gluon-gluon fusion in a top quark triangle loop ($gg \rightarrow h_{SM}$); less important are Higgs production through a virtual vector boson ($q\bar{q}' \rightarrow V^* \rightarrow Vh_{SM}$), vector boson fusion (shown in the Figure 2.1 as $qq \rightarrow h_{SM}qq$), and associated production with pairs of top and b-quarks, see [1]. The importance of the last channel will be discussed in the context of the Minimal Supersymmetric extension of the Standard Model below.

When estimating the sensitivity of a particle search, one needs to take into account not only the particle production cross section, but also the decay channel that has the largest branching ratio. As shown in Figure 2.2, most significant in this respect are channels where the Higgs boson decays into b-quarks and τ-leptons. Both of them are interesting for the Higgs search, despite the ratio of $\sim 9:1$ in their braching fractions, because the τ channel QCD backgrounds are less of a hindrance.

The Standard Model is a very good approximation to the physics of elementary particles and their interactions at the scales below 100 GeV. However, it clearly does not describe the onset of possible quantum gravitational effects at energies much higher than 1 TeV and most probably of the order of the Plank scale of 10^{19} GeV. It is not a fundamental theory of Nature but rather an effective field theory. Among other things, it does not have a satisfactory solution to the hierarchy problem. The mass of the Higgs boson is also not determined by the SM. There is a possible range

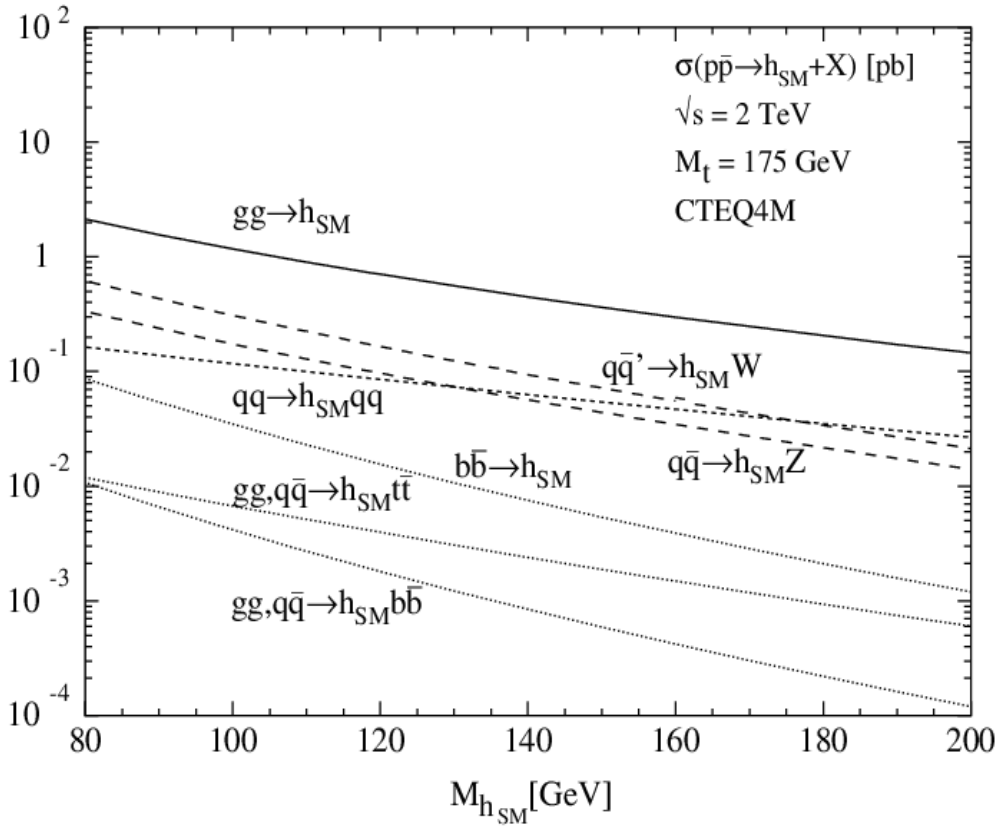

Figure 2.1. Cross section of the Standard Model Higgs boson production at the Fermilab Tevatron. Adapted from [1].

of Higgs boson masses (130 GeV $\lesssim h_{SM} \lesssim$ 180 GeV, see Figure 2.3), where the SM does not preclude its own viability up to the Plank scale. However, most theorists consider the possibility that the SM is unchanged up the Planck scale unlikely, based on the following "naturalness" argument.

The larger the cut-off scale Λ, the more fine tuning is needed between the terms in the expression for the physical mass of the Higgs boson, like in Eq. 2.2.

$$m_h^2 = (m_h^2)_0 + cg^2\Lambda^2, \tag{2.2}$$

where m_h^2 is the physical Higgs boson mass squared, $(m_h^2)_0$ is the bare Higgs boson

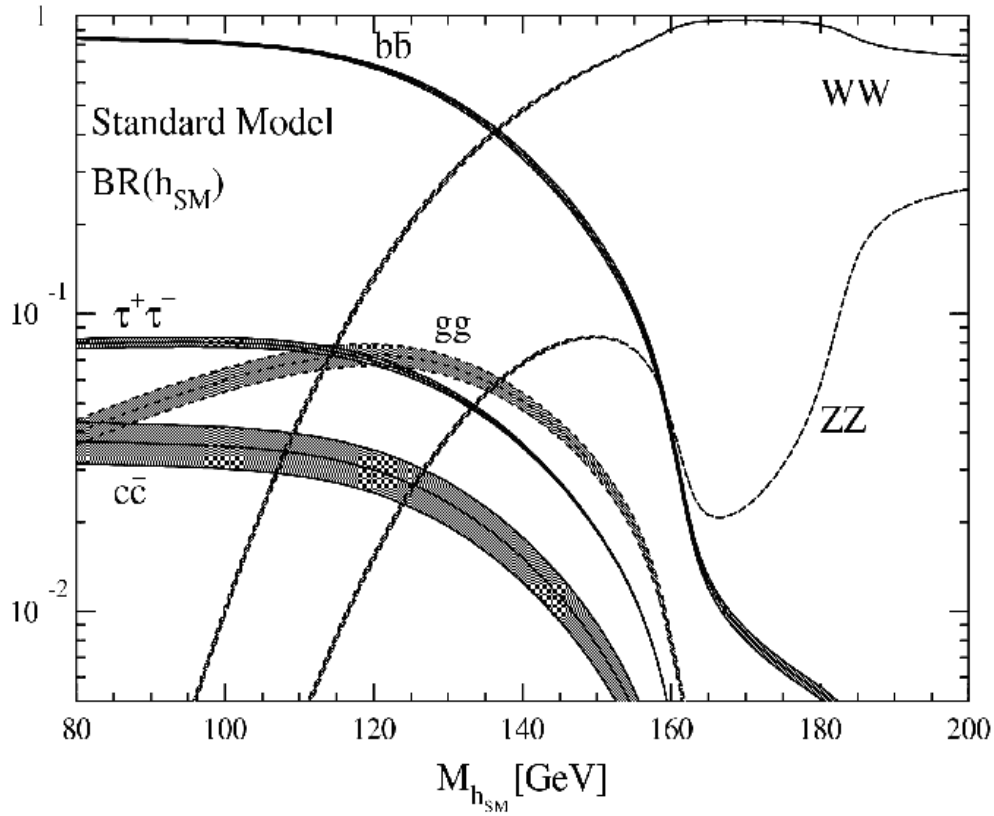

Figure 2.2. Branching ratios of the Standard Model Higgs boson decay. Adapted from [1]

mass squared, c is a constant of $\mathcal{O}(1)$, and g is the electroweak coupling constant.

There, two very large terms of different nature have to cancel almost exactly to produce the actual physical mass of the Higgs boson m_h, which is supposed to be constrained between the lower and upper bounds, like in Figure 2.3. The lower bound is derived from the requirement of vacuum stability [4]. The upper bound is related to the scale of the Higgs mass where the behaviour of the quartic self-coupling term in the Higgs potential $V(\phi)$ becomes unsatisfactory [5].

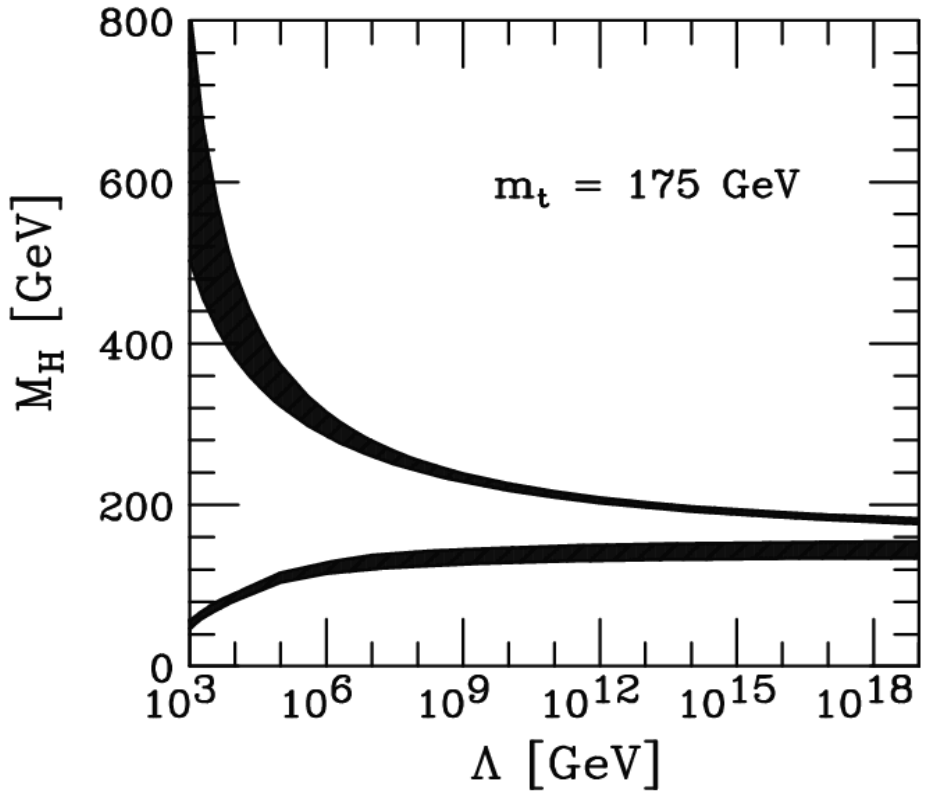

Figure 2.3. The lower [4] and the upper [5] Higgs mass bounds as a function of the energy scale Λ at which the Standard Model breaks down, assuming $M_t = 175$ GeV and $\alpha_s(m_Z) = 0.118$. The shaded areas above reflect the theoretical uncertainties in the calculations of the Higgs mass bounds. This figure is taken from [6].

2.2 Supersymmetry

In supersymmetric theories, in contrast to the SM, both bosonic and fermionic particle masses are only logarithmically sensitive to Λ. This is why an effective low-energy supersymmetric theory will still have weakly coupled Higgs bosons, but will be valid up to Planck scale. The simplest realistic model of low-energy supersymmetry is a minimal supersymmetric extension of the Standard Model (MSSM) [7].

Most of the 124-dimensional MSSM parameter space is ruled out because of the presense of large lepton family number non-conservation, unsuppressed flavor changing neutral currents (FCNC's), and observable electric dipole moments of the electron and neutron, inconsistent with the experimental bounds. It also requires two complex Higgs doublets to cancel quantum anomalies and generate masses for both "up"-type and "down"-type quarks and charged leptons [8]; the hypercharge $Y = -1$ one $\Phi_d = (\Phi_d^0, \Phi_d^-)$ and $Y = +1$ one $\Phi_u = (\Phi_u^+, \Phi_u^0)$, which give 8 degrees of freedom in total. EWSB results in the absorption of three of them by EW bosons longitudinal components, and five physical Higgs bosons remain: neutral CP-even h and H, CP-odd A, and a charged pair, $H^\pm$. The Higgs sector mass spectrum is constrained in the MSSM and is usually described in terms of $\tan\beta$, which is equal to the ratio of the two doublet neutral components vacuum expectation values $\tan\beta = \frac{v_u}{v_d}$, and m_A, the mass of the pseudoscalar A.

What is remarkable about the behaviour of the Higgs sector in the MSSM is that the couplings of the Higgs bosons to "down"-type quarks and leptons are generally enhanced compared to the SM ones by roughly a factor of $\tan\beta$. However, there is also a CP-even Higgs boson mixing parameter α, which depends on m_A and $\tan\beta$ as in Eq. 2.3, and influences the relative sizes of "down"-type couplings to the light and heavy Higgs bosons ($g_{hb\bar{b}}, g_{h\tau^+\tau^-} \sim -\frac{\sin\alpha}{\cos\beta}$, $g_{Hb\bar{b}}, g_{H\tau^+\tau^-} \sim \frac{\cos\alpha}{\cos\beta}$).

$$\cos^2(\beta - \alpha) = \frac{m_h^2(m_Z^2 - m_h^2)}{m_A^2(m_H^2 - m_h^2)} \tag{2.3}$$

The light CP-even Higgs boson mass has an upper bound that can be calculated in the MSSM with arbitrary accuracy in terms of m_A, $\tan\beta$, and some other MSSM soft-supersymmetry-breaking parameters that affect the Higgs mass through virtual loops. The tree-level upper bound $m_h \lesssim m_Z$ is shifted upward by the radiative corrections. The upper bound is between 122 GeV and 135 GeV depending on

the top squark (supersymmetry partner of the top quark) mixing parameter X_t[1], supersymmetric higgs mass parameter μ, in the limit where $\tan\beta$ is large [1]. The upper bound corresponds to $\mu = -200$ GeV and large values of X_t of the order of 2 TeV (maximal mixing). The lower bound corresponds to $X_t = 0$ (no-mixing). As one can see from Figure 2.4, with the increase of $\tan\beta$, masses of CP-even Higgs bosons become degenerate with the mass of the pseudoscalar A.

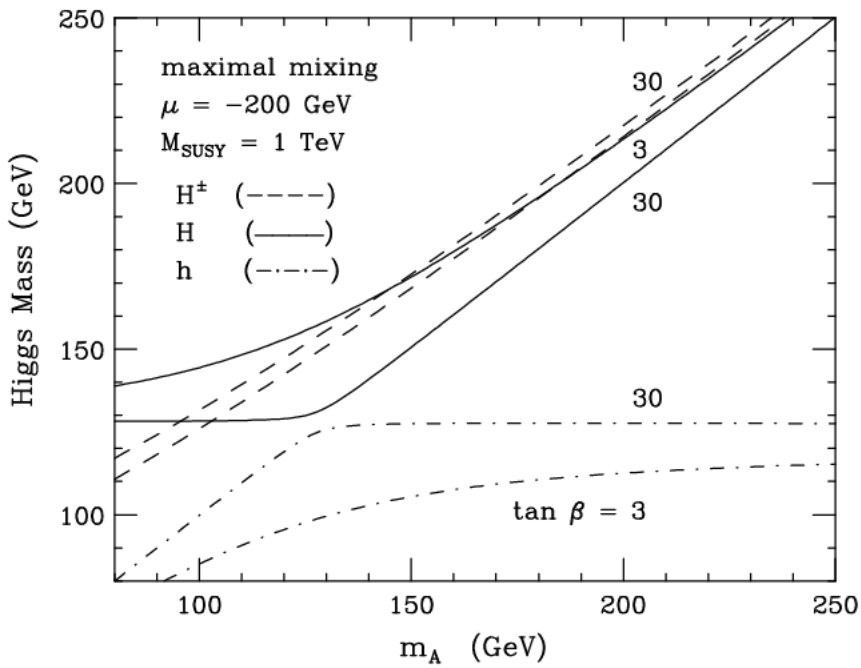

Figure 2.4. Lightest CP-even Higgs mass m_h, heaviest CP-even Higgs mass m_H and charged Higgs mass (mH) as a function of mA for two choices of $\tan\beta = 3$ and $\tan\beta = 30$.

This analysis looks for the MSSM neutral Higgs boson production in association with b-quarks at high $\tan\beta$. They are produced in processes similar to the SM Higgs production in association with b-quarks, which are dominated by gluon fusion or

[1]Incomplete cancellation of the top quark and top squark loops dominates the upward shift of the m_h upper bound.

b-quark - gluon fusion. Figures 2.5 and 2.6 show leading order SM diagrams involved in the 4-flavor scheme and 5-flavor scheme, respectively. The 4-flavor scheme has no b-quarks at the initial stage, and either places no cuts on the final stage b-quarks or requires only 1 b-quark at high transverse momentum. The 5-flavor scheme stabilizes the perturbative cross section by resumming the large logarithms into the b-quark parton distribution function (PDF) [10]. Figures 2.7 and 2.8 show their production cross sections for small and large $\tan\beta$, including all known QCD corrections. We can see that the cross sections of processes, where the Higgs bosons are produced in association with b-quarks, tend to grow much faster with $\tan\beta$. At high $\tan\beta$ the values of the production cross section of A, h, or H, in the corresponding m_A range become very close. And because the experimental signatures of these processes are indistinguishable, one should normalize the hypothetical signal cross section to double that of a single Higgs boson. The widths of the Higgs bosons are directly proportional to the b-quark coupling but are small enough to be less than the detector resolution ($\sim$ 20 GeV) up to $\tan\beta \lesssim 60$, and do not affect the search sensitivity within the range of this search ($90 \lesssim m_A \lesssim 160$ GeV). Figure 2.9 shows the widths of the neutral Higgs bosons at $\tan\beta = 60$. Depending on the supersymmetric mass parameter μ[2], the Higgs resonance widens into the low mass region (mostly for the negative values of this parameter), which means lower signal acceptances, see Chapter 5. However, the enhancement of the cross section with the increase of $\tan\beta$ compensates for the loss. Moreover, FEYNHIGGS calculations [62] show that these two effects almost cancel each other for $\tan\beta \lesssim 80$, so that the overall effect is negligible. The effect of the Higgs widths is not taken into account explicitly in this analysis.

As in the SM, the leading neutral Higgs bosons decay channels are $b\bar{b}$ and $\tau^+\tau^-$.

[2]The scenarios, considered in this analysis, involve $\mu = \pm 200$ GeV.

Figure 2.5. Leading-Order Feynmann diagrams for neutral Higgs boson production in associated with b-quarks in the 4-flavor scheme. Adapted from [10]

Figure 2.6. Leading-Order Feynmann diagrams for neutral Higgs boson production in associated with b-quarks in the 5-flavor scheme. Adapted from [10]

There is a specific range of MSSM parameters where radiative corrections lead to suppression of both these channels compared to other decay processes or with respect to each other, but generally these decay channels dominate, especially at high $\tan\beta$, and maintain a ratio around 9:1. Figure 2.10 shows MSSM CP-even Higgs bosons h and H decay branching ratios and Figure 2.11 shows the same for CP-odd A. In these plots, top-squark mixing is maximal and superparticle decay modes are outside the given mass range.

As it has been mentioned in [46], the $\tau^+\tau^-$ decay channel has sensitivity comparable to the $b\bar{b}$ channel in case of associated production with b-quark.

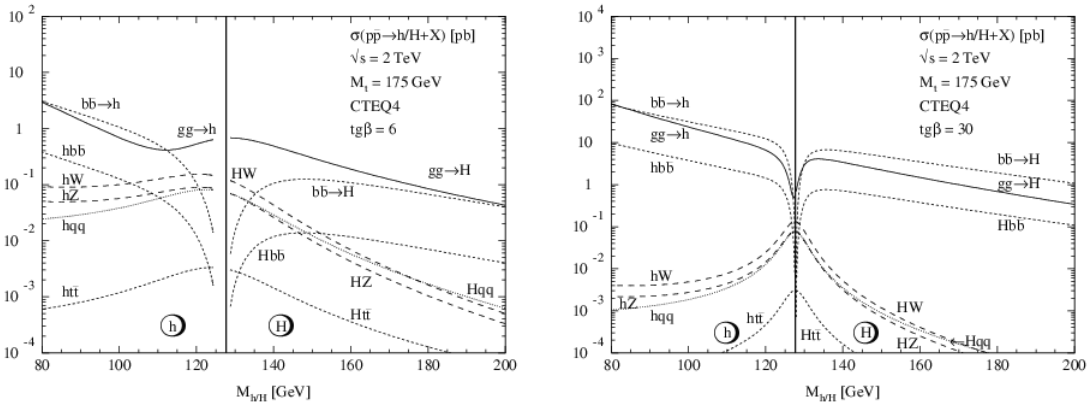

Figure 2.7. Production crosssections for neutral CP-even Higgs bosons h, H in MSSM, for $\tan\beta = 6$ (left) and $\tan\beta = 30$ (right). Adapted from [1]

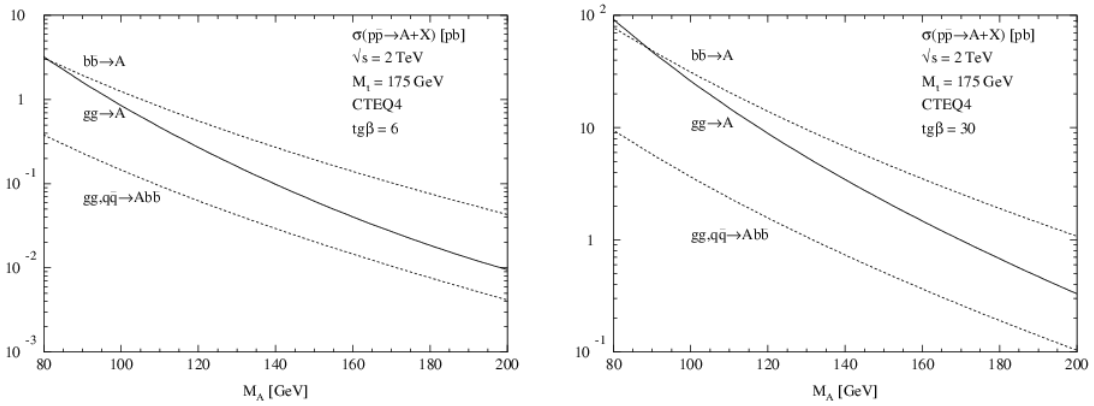

Figure 2.8. Production crosssections for neutral CP-odd Higgs boson A in MSSM, for $\tan\beta = 6$ (left) and $\tan\beta = 30$ (right). Adapted from [1].

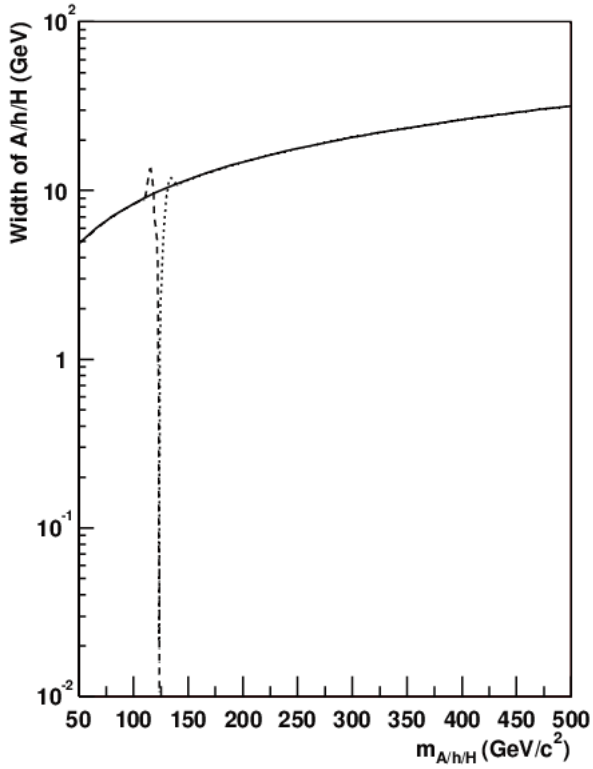

Figure 2.9. Widths of the neutral Higgs bosons at $\tan\beta = 60$ GeV. A is solid, h is dashed, and H is dotted. Adapted from [9].

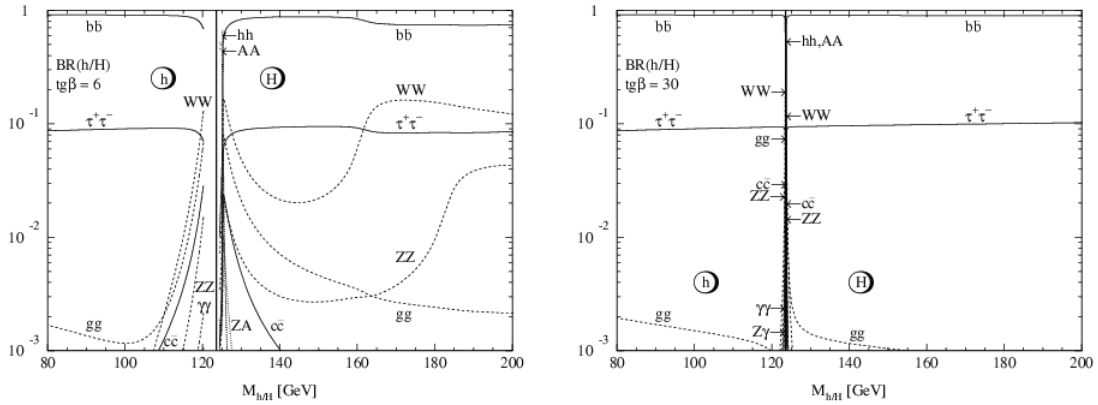

Figure 2.10. Branching ratios of the MSSM neutral CP-even Higgs bosons h and H decay at $\tan\beta = 6$ (left) and $\tan\beta = 30$ (right). Adapted from [1].

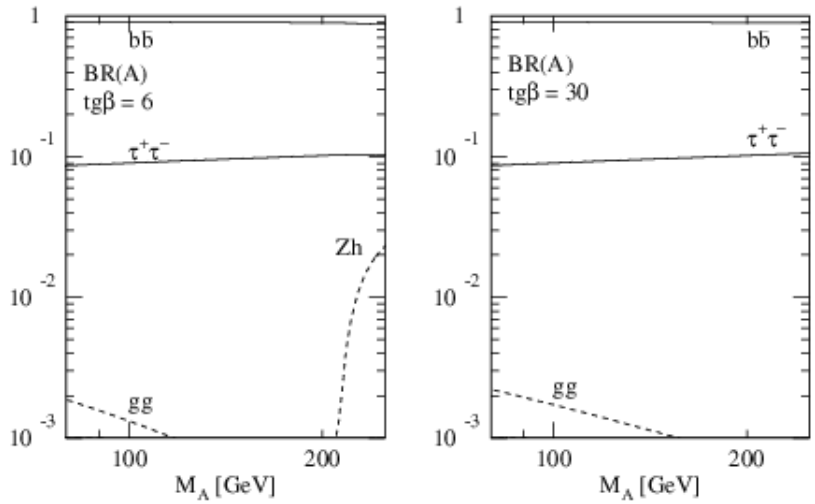

Figure 2.11. Branching ratios of the MSSM neutral CP-odd Higgs boson A decay at $\tan\beta = 6$ (left) and $\tan\beta = 30$ (right). Adapted from [1].

CHAPTER 3

THE EXPERIMENTAL APPARATUS

The data for this analysis were recorded at the Fermilab DØ Detector, which is a part of the diverse Fermilab experimental program. The DØ detector measures the final state particles coming from the colliding $p\bar{p}$ beams provided by the Tevatron accelerator. Since Run I, which ended in 1996 and led to the discovery of the top quark, the Fermilab accelerator complex and detectors have been significantly upgraded. The Tevatron Run II started in 2001 and plans to deliver more than $4fb^{-1}$ of integrated luminosity by the end of the year 2009. For Run II, a new Main Injector replaced the old Main Ring, and a new anti-proton storage ring, the Recycler, was constructed, using a common tunnel with the Main Injector [11], [12]. The Tevatron was upgraded to operate at a higher center-of-mass energy, 1.96 GeV (compared to 1.8 GeV in Run I), and to accomodate 36 proton-antiproton bunches, colliding almost every 396 ns, instead of 6 bunches, separated by 3500 ns, in Run I.

3.1 The Fermilab Accelerators

The Tevatron is the largest of a series of Fermilab particle accelerator machines and provides the final stage of acceleration of proton-antiproton beams to bring them to a head-on collision at a number of points around its circumference. It has a 1 km-radius synchrotron made of about 1000 superconducting magnets able to maintain steady 980 GeV $p\bar{p}$ beams for more than 24 hours. The Tevatron is the

only cryogenically cooled accelerator at Fermilab. Its magnets use a superconducting niobium-titanium alloy which has to be kept below 4 K to remain a superconductor. The Tevatron is not a perfect circle. The ring is divided into 6 sectors named A through F. Each has 5 service buildings: "0" through "4". Each "0" location contains a large straight section. A0 connects the Tevatron to the Switchyard. CDF detector is located at B0, C0 is unused, the D0 detector is located where the name suggests, and the busiest section is F0, where the RF cavities are, as well as the connection point of P1 and A1 transfer lines [14], Figure 3.1.

The proton-antiproton beams are supplied to the Tevatron by a number of other units, like the Pre-accelerator with a Cockcroft-Walton accelerator; Linac, Booster, Main Injector, Antiproton Source with a Debuncher and Accumulator, and Recycler. They are all schematically shown in Figure 3.1 and are described in more detail below.

3.1.1 The Pre-accelerator

There are two Cockcroft-Walton electrostatic preaccelerators using a separate H^- ion source inside a dome kept at a potential -750 kV. Each is capable of producing beams of negatively charged hydrogen ions at energies of up to 750 keV. The sources are direct-extraction magnetron type and produce short pulses of negative ions at the Linac repetition rate of 15 Hz. H^- ions are produced in a source when protons from a plasma between the molybdenum cathode and anode occasionally pick up extra electrons from the cathode and are repelled from the cathode. Charge exchange of these ions with neutral hydrogen atoms produces a flow of ions with a smaller energy spread. After that, ions are pulsed out of the source by an electrostatic extractor to the accelerating column. Cesium vapor, introduced into the source, coats the electrodes and lowers the surface work function, enhancing the

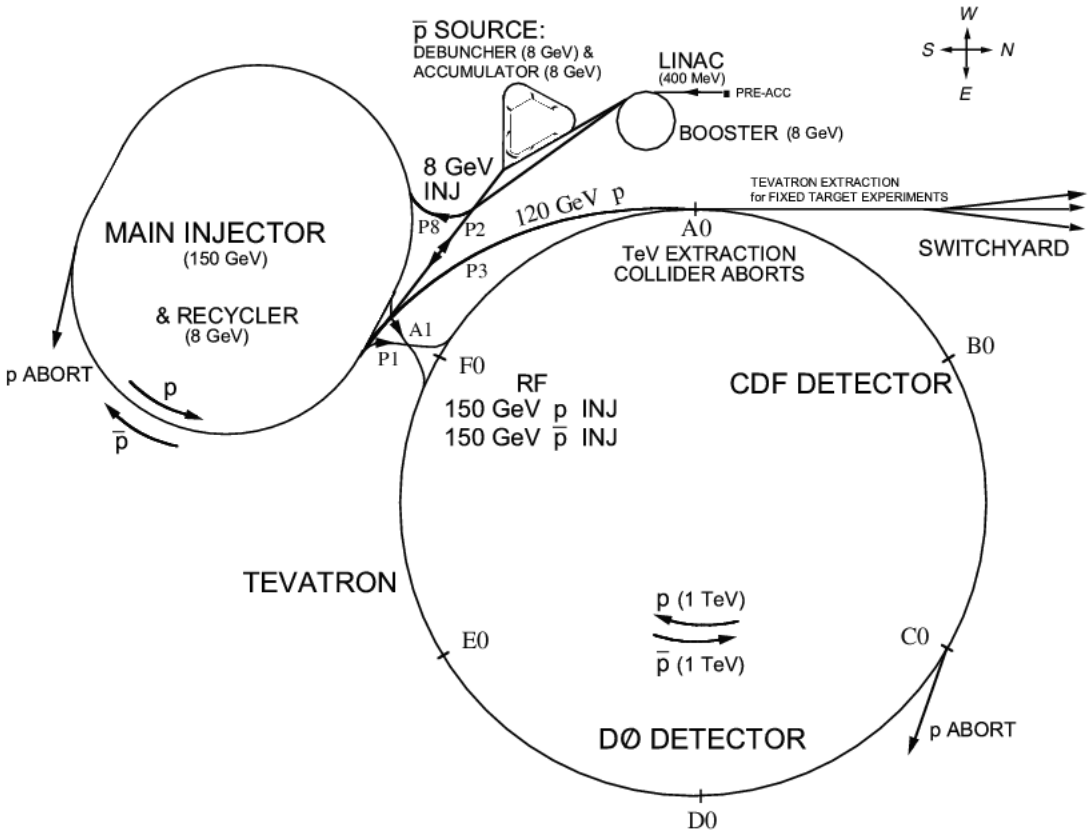

Figure 3.1. The Fermilab accelerator complex. Adapted from [9].

production of negative ions by the cathode [13]. The schematic of this process is shown in Figure 3.2.

3.1.2 The Linac

The Linear Accelerator (Linac) accelerates the H^- ions from 750 keV to 400 MeV. Its total length is about 500 feet. The Linac consists of two main sections: the Drift Tube Linac (DTL), making up the first 5 RF stations; and the Side Coupled Cavity Linac (SCL), making up the last 7 RF stations. An ion beam is accelerated by a 201 MHz signal in the DTL and a 805 MHz signal in the SCL through a series of RF cavities. Cavity lenghth increases with the increasing speed of the beam. The

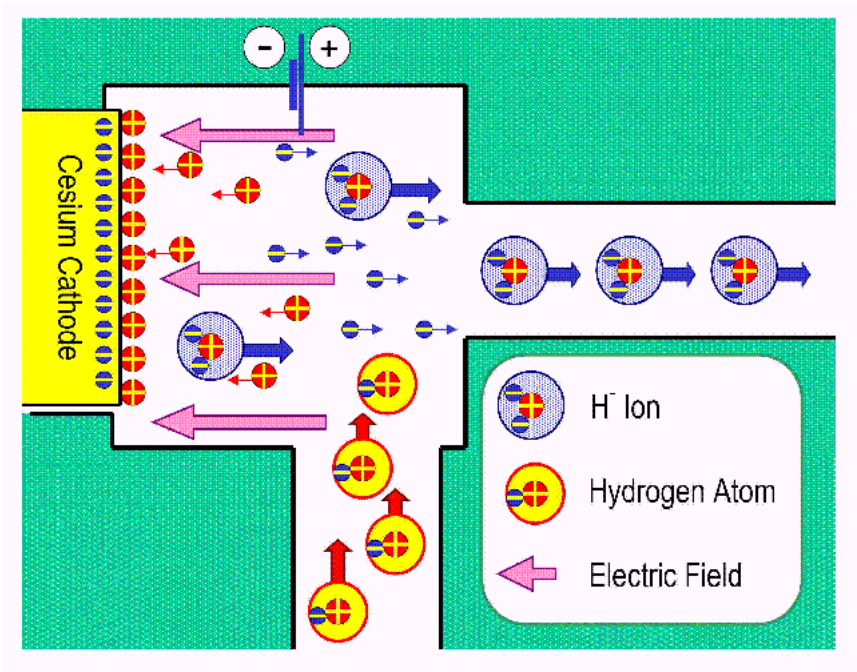

Figure 3.2. Schematic view of H^- source operation principle. Adapted from [2].

Linac can supply H^- beam to either the Booster or the Neutron Therapy Facility [14]. The schematic of the Linac operation is shown in the Figure 3.3.

3.1.3 The Booster Synchrotron

The Booster is the first intermediate synchrotron accelerator used to accelerate the proton beam coming out of the Linac at 400 MeV. The injection system puts the hydrogen ions through a carbon foil, stripping the 2 electrons off, and stacks several turns of beam from one Linac pulse on top of each other. After about 20,000 revolutions around the 1,500 foot Booster, a batch of 5-7 bunches is accelerated to 8 GeV (in about 0.03 seconds) and is transfered to the Main Injector. Each bunch contains $5 \sim 6 \times 10^{10}$ protons.

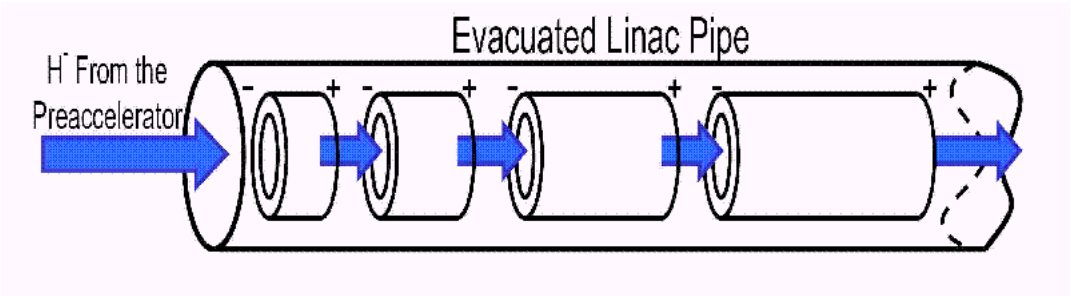

Figure 3.3. Schematic of Linac operation principle. Adapted from [2].

3.1.4 The Main Injector

The Main Injector is another circular synchrotron multi-purpose accelerator. It can accelerate 8 GeV protons up to 120 or 150 GeV, depending on the destination. The 120 GeV beams are sent to the Anti-proton source during stacking, or producing anti-protons. For that purpose two Booster batches are usually merged together. During shot setup when protons are transfered to the Tevatron, seven bunches are loaded from the Booster and accelerated to 150 GeV. They are coalesced together into one bunch and injected into the Tevatron [14]. The Main Injector can also send 120 GeV beams to fixed targed and neutrino experiments.

3.1.5 The Anti-proton Source

The Anti-proton source consists of a target station, Debuncher and Accumulator. At the target station, a 120 GeV proton beam from the Main Injector hits one of a stack of nickel disks. The target can be rotated to prevent potential damage to the disk in use. Its position can be also adjusted vertically and horisontally for disk switching or alignment relative to the Collection Lens [15]. The lens is a cylindrical Lithium conductor designed to operate at 670 kA currents to produce solenoidal magnetic fields with the gradient 1kT/m to focus negative secondary particles. A

pulsed dipole magnet collects the 8 GeV particles and bends them towards the Debuncher, as shown in Figure 3.4.

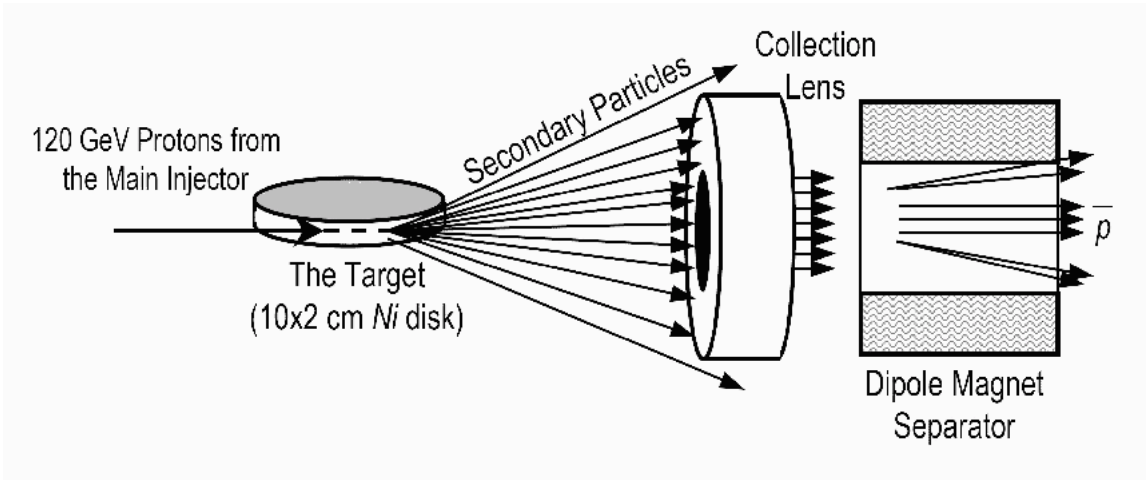

Figure 3.4. Schematic of $\bar{p}$ production. Adapted from [2].

The Debuncher is a 1,700 foot rounded-triangular shaped synchrotron using RF bunch rotation and adiabatic debunching to reduce the anti-protons momentum spread. It also uses stochastic cooling to reduce beam transverse size during the time between the Main Injector cycles.

The Accumulator is a 1,500 foot synchrotron, also rounded-triangular, housed in the same tunnel as the Debuncher. It cools the anti-protons further with stacktail momentum, core momentum, and core transverse cooling systems. This process takes from several hours to several days to accumulate 2×10^{12} anti-protons.

3.1.6 The Recycler

The Recycler is an antiproton storage ring located along the ceiling of the Main Injector tunnel. The proposed purpose of the Recycler was to "recycle" the antiprotons from a Tevatron store, cooling them and storing them alongside those sent from the Anti-proton Source. This was abandoned after early problems in Collider Run

II. The Recycler now accepts transfers only from the Anti-proton source and cools them further than the antiproton Accumulator is capable. The Recycler uses both a stochastic cooling system (like the Antiproton Source) and an electron cooling system.

3.2 The Run II DØ Detector

The Run II DØ detector consists of three major subsystems: central tracking detectors, uranium/liquid-argon calorimeters, and a muon spectrometer. The central tracking system has been completely replaced since Run I. The new system includes a silicon microstrip tracker and a scintillating fiber tracker located inside a 2T solenoidal magnet. In addition, preshower detectors have been placed between the solenoidal magnet and the central calorimeter, and in front of the forward calorimeters. Proportional drift chambers in the forward muon system have been replaced with mini drift tubes, and trigger scintillation counters have been installed in both central and forward muon systems. With the significant increase of the collision rate major upgrades have been also made to the calorimeter and muon system electronics, and to the trigger system [16]. A schematic of the DØ detector is shown in Figure 3.5.

The Coordinate system used below is the right-hand one with the z-axis along the proton beam direction (North to South) and the y-axis upward. (r, θ, ϕ) are the corresponding spherical coordinates in these axes. The pseudorapidity, $\eta = -\ln[\tan(\frac{\theta}{2})]$, approximates the true rapidity, $y = 1/2\ln[(E + p_z c)/(E - p_z c)]$, for finite angles in the relativistic limit. The term "forward" describes the regions at large $|\eta|$.

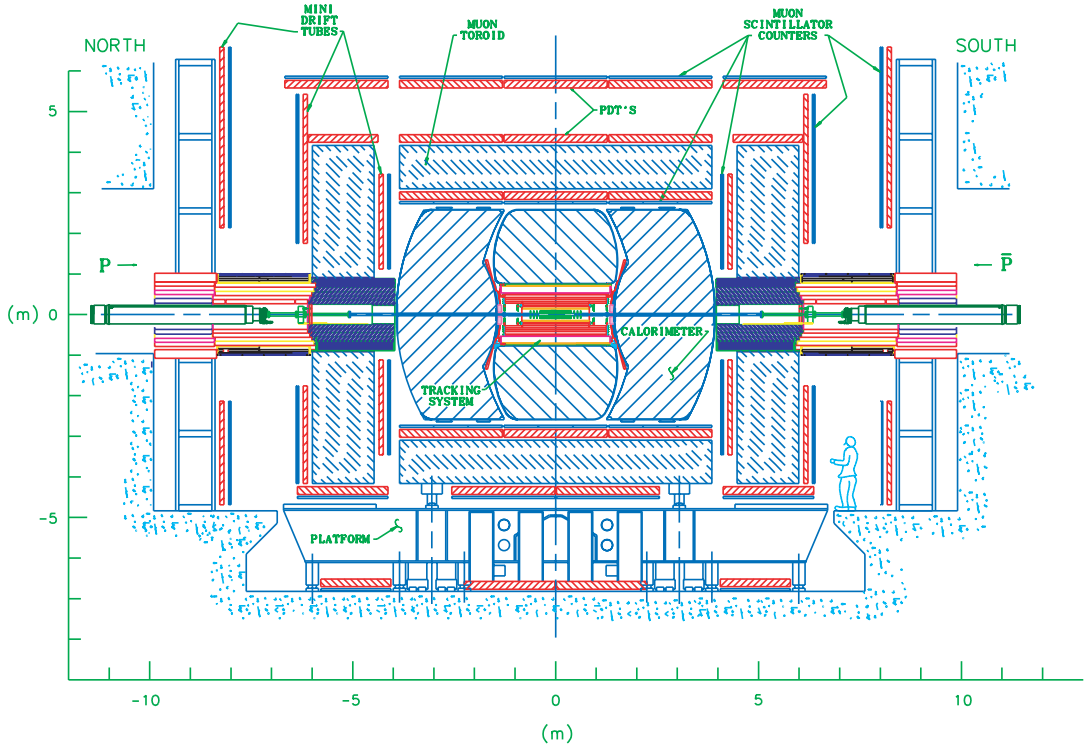

Figure 3.5. The upgraded DØ detector. Adapted from [9].

3.2.1 Luminosity monitor

Rates of events are measured as $N = \mathcal{L}\sigma$, where $\mathcal{L}$ is the integrated luminosity (instantaneous luminosity integrated over time), and σ is the effective interaction area for the given process, or cross section. Instantaneous luminosity is measured by detecting inelastic $p\bar{p}$ collisions in the luminosity monitor (LM). The LM also serves to measure beam halo rates and make a fast measurement of the z coordinate of the interaction vertex. It consists of two arrays of 24 plastic scintillation counters, located at ± 140 cm from the middle of the detector, marked as Level 0 in Figure 3.6. They cover $|\eta|$'s from 2.7 to 4.4. The time resolution of the scintillator detectors is $\lesssim 0.3$ ns, needed to discriminate between particles originating from the interaction region and those in either of the remaining beam halos [16].

3.2.2 Tracking System

The Silicon microstrip detector (SMT) surrounds the DØ berillium beam pipe and does both tracking and vertexing (locating interaction and decay vertices) over nearly the full η coverage of both the calorimeter and muon systems, Figure 3.6.

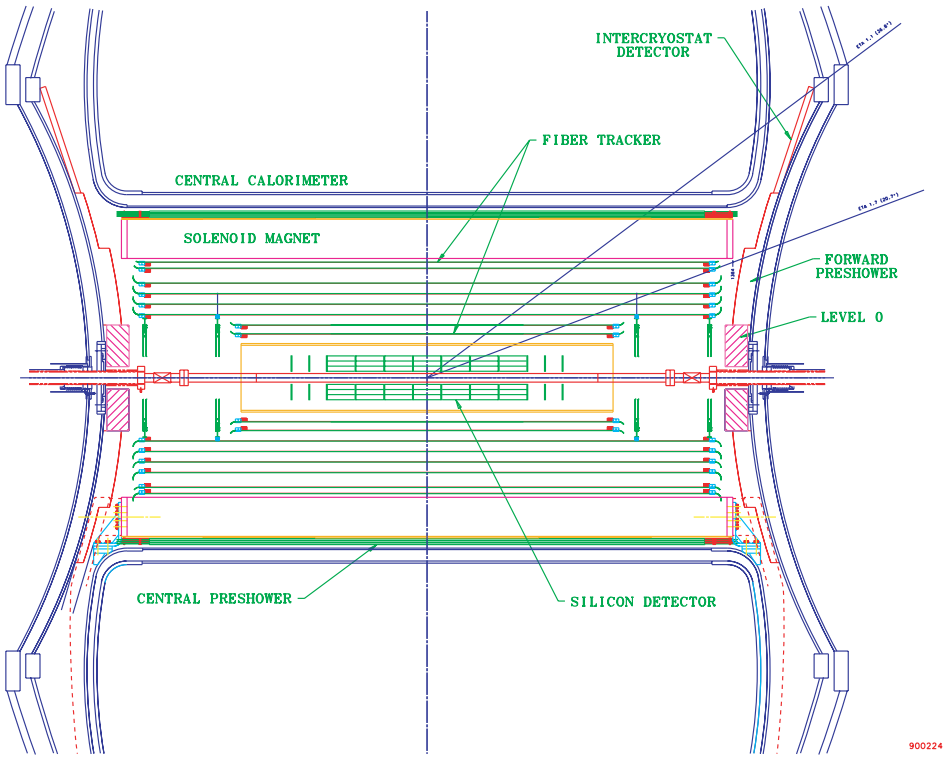

Figure 3.6. Tracking detectors, preshowers, and luminosity monitor (Level 0). Adapted from [9].

It makes use of the electron-hole pairs produced at a p-n junction in silicon when a charged particle passes through. These pairs are separated by an applied voltage and drift through the 300 μm thick wafers towards 50 μm wide conducting strips implanted in the silicon. The charge collected from each strip is stored in a capacitor, until it is readout and digitized by specialized electronics.

The length of the interaction region, $\sim$ 25 cm, suggests barrel-disk design, where

there are always elements that tracks traverse at small incident angles. The barrels are each 12 cm long and consist of 4 layers of silicon wafers and readout chips. Layers 1 and 2 have 12 silicon modules ("ladders"), and layers 3 and 4 have 24 of them, with a total of 432 ladders. Each barrel is capped at high $|z|$ with an "F-disk", a disk-shaped group of 12 double sided wedge detectors. There are three additional F-disks forward of each of the 3-barrel-disk assembly (Figure 3.7). Even further forward, there are 3 large "H-disks", each having 24 back-to-back pairs of single-sided wedges. Each side (if double-sided) of a wedge is read out independently, which makes 912 read out units with 792,576 channels. The SMT is read out using the 128-channel SVXIIe chip [18]. The chip includes preamp, analog delay, digitization, and data sparsification. Input charge is integrated on the preamplifier for a train of beam crossings (typically twelve) and reset during inter-bunch gaps. This charge is delivered to a 32-cell analog pipeline.

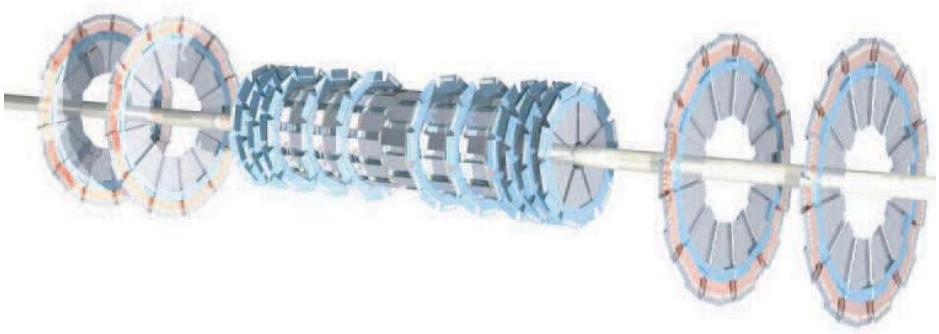

Figure 3.7. Silicon microstrip detector. Adapted from [17].

The Central Fiber Tracker (CFT) surrounds the SMT and together with the SMT participates in the charged particle reconstruction. It consists of scintillating fibers mounted on 8 concentric support cylinders. It occupies the radial space from 20 to 52 cm from the center of the beampipe. To accomodate the forward SMT H-

disks, the two innermost cylinders are 1.66 m long; the outer six cylinders are 2.52 m long. The outer cylinder provides coverage up to $|\eta| \lesssim 1.7$. Each cylinder has one doublet layer of fibers oriented in the beam direction (z) and a second doublet layer oriented at an angle $+3°$ (u) or $-3°$ (v). The innermost cylinder has zu layer combination, the second innermost has zv combination and so on (Figure 3.8).

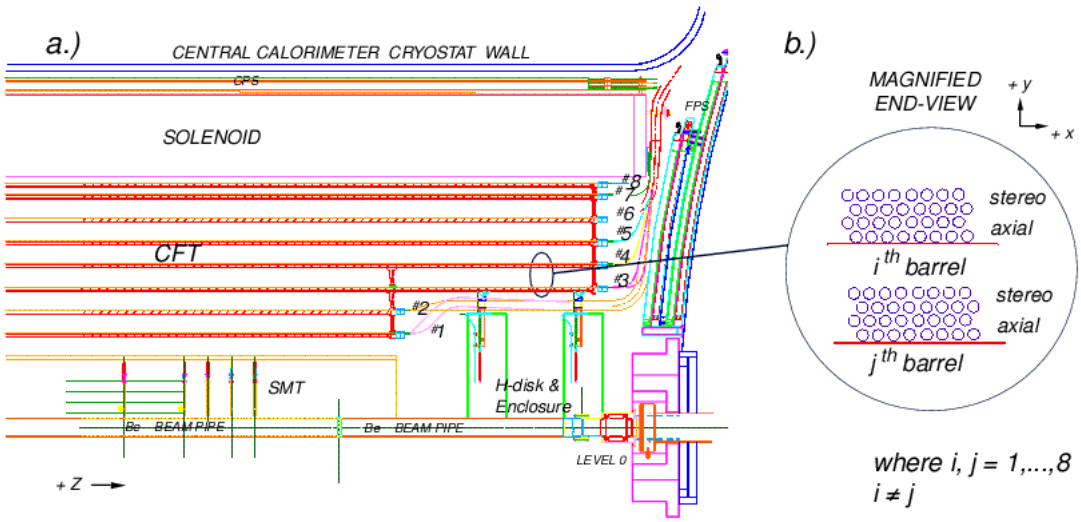

Figure 3.8. Central Fiber Tracker. Adapted from [2].

Each scintillating fiber is 835 μm in diameter, composed of a 775 μm core surrounded by a coating with a high index of refraction, providing total internal reflection. The base core material is doped with organic fluorescent dye to about 1% and a small quantity of a wave-shifting dye. Excitations produced by a charged particle in the core material are transfered to the fluorescent dye molecules through non-radiative dipole-dipole interactions; dye molecules emit light at ≈ 340 nm with a short mean free path, but the wave-shifter re-emits light at 530 nm, which is well transmitted in the base core material. An ionizing particle can produce 8 photons per fiber on average.

The fibers are optically connected to clear fiber waveguides from 7.8 to 11.9 m long, and through them to Visible Light Photon Counters (VLPC). VLPCs are silicon devices, converting photons to electron-hole pairs, and are normally operated at cryogenic temperatures of 9K to reduce electron noise. Application of a bias voltage of around 6V produces avalanches of electrons. A gain of up to 65,000 can be achieved with a quantum efficiency of $\lesssim 80\%$ per photon. The electrons from photon conversions are collected within $\lesssim 100$ ns, before the next bunch crossing takes place. 1024 VLPCs are combined into cassettes which carefully regulate the temperature of the devices and contain the readout electronics [16].

The digitization and readout of the CFT is performed nearly identically to that of the SMT. The two tracking detectors locate the primary interaction vertex with a resolution of about 35 μm along the beamline. They can tag b-quark jets with an impact parameter resolution of better than 15 μm in r-ϕ for particles with transverse momentum $p_T > 10$ GeV/c at $|\eta| = 0$.

3.2.3 Preshowers

Preshowers aid in electron identification at both triggering and offline reconstruction stages, and tau identification offline. They function as calorimeters as well as tracking detectors, enhancing the spatial matching between tracks and calorimeter showers [19]. The detectors can be used offline to correct the electromagnetic energy measurement of the central and end calorimeters for losses in the solenoid and upstream material, such as cables and supports. Their fast energy and position measurements allow preshower information to be included in the Level 1 trigger.

The preshower detectors share common elements with the central fiber tracker, beginning with the waveguides and continuing through the entire readout electronics. Both preshower detectors are made from triangular strips of scintillator, as

shown in Figure 3.9, with the wave-shifting round fibers embedded at centers of the strips.

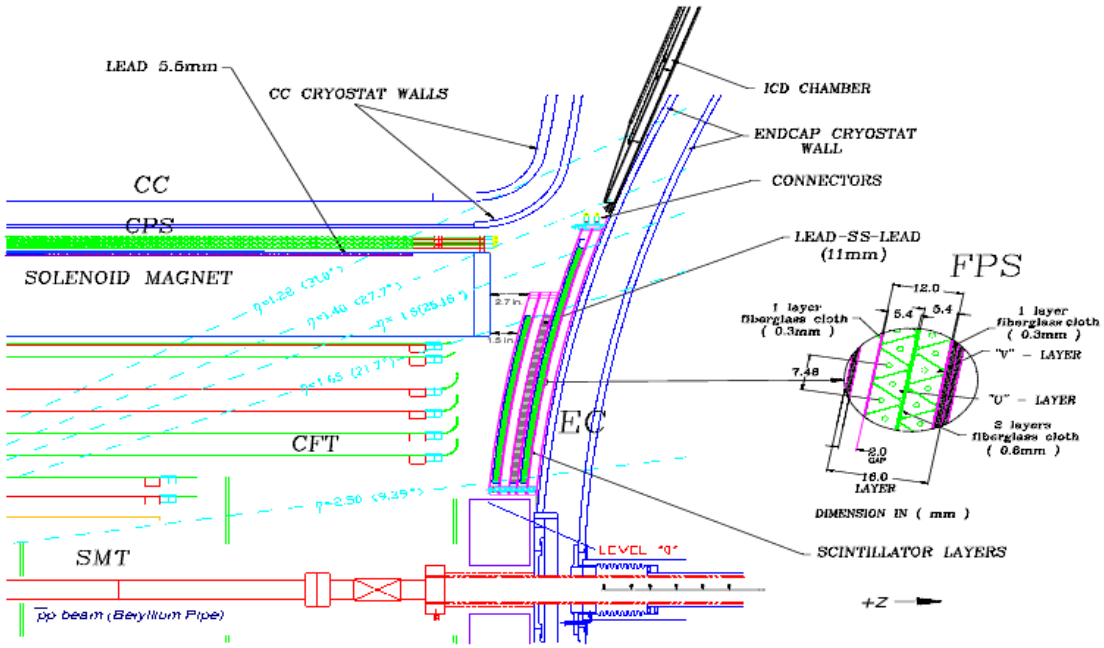

Figure 3.9. Preshower detectors. Adapted from [2].

The central preshower detector (CPS) covers the region $|\eta| < 1.3$ and is located between the solenoid and the central calorimeter with an inner radius of 28.25" and an outer radius of 29.21". The two forward preshower detectors (FPS) cover $1.5 < |\eta| < 2.5$ and are attached to the faces of the end calorimeters. Between the CPS and the solenoidal magnet a lead radiator 7/32" (around 1 radiation length) is placed. The CPS consists of three doublet layers of scintillating strips. The innermost layer is an axially arranged layer, while the two outer layers are interleaved at stereo angles of $\pm 23°$. The CPS has a total of 7,680 channels of readout.

The FPS consists of two doublet two-plane layers (Figure 3.9). The one that is closest to the interaction region is a Minimal Ionizing Particle layer (MIP) while the

outermost is the shower layer. They are separated by 2 radiation length stainless steel absorbers. Strips in the two planes in each layer also cross at around 23°. Readout of the FPS detectors, together totaling 14,968 channels, is done similarly to the CFT and CPS, using the same VLPC system.

3.2.4 Calorimetry

The DØ calorimeter system consists of three sampling calorimeters (primarily uranium/liquid-argon) and an intercryostat detector. It is used to measure energies of electrons, photons, jets, assist in identification of muons and taus, and measure transverse energy balance in events.

The calorimeters themselves are unchanged from Run I. The Central Calorimeter (CC) covers $|\eta| \lesssim 1$ and the two End Calorimeters, ECN (North) and ECS (South) extend the coverage up to $|\eta| \lesssim 4$, see Figure 3.11. The active medium for the calorimeters is liquid argon and each of the three calorimeters (CC, ECN, and ECS) is located within its own cryostat that maintains the detector temperature at approximately 90K. Each calorimeter has an electromagnetic section closest to the interaction region followed by fine hadronic and coarse hadronic ones, as in Figure 3.10.

Particles reaching the calorimeter create showers by interacting with the dense material in the absorber plates. Different absorber plates are used at different locations. The electromagnetic sections (EM) use thin plates (3 and 4 mm in the CC and EC, respectively), made from nearly pure depleted uranium. The fine hadronic sections are made from 6-mm-thick uranium-niobium (2%) alloy. The coarse hadronic modules contain relatively thick (46.5 mm) plates of copper (in the CC) or stainless steel (EC). Showers are sampled at many points to determine their shape and energy. Between the absorber plates there are 2.3 mm wide unit cells,

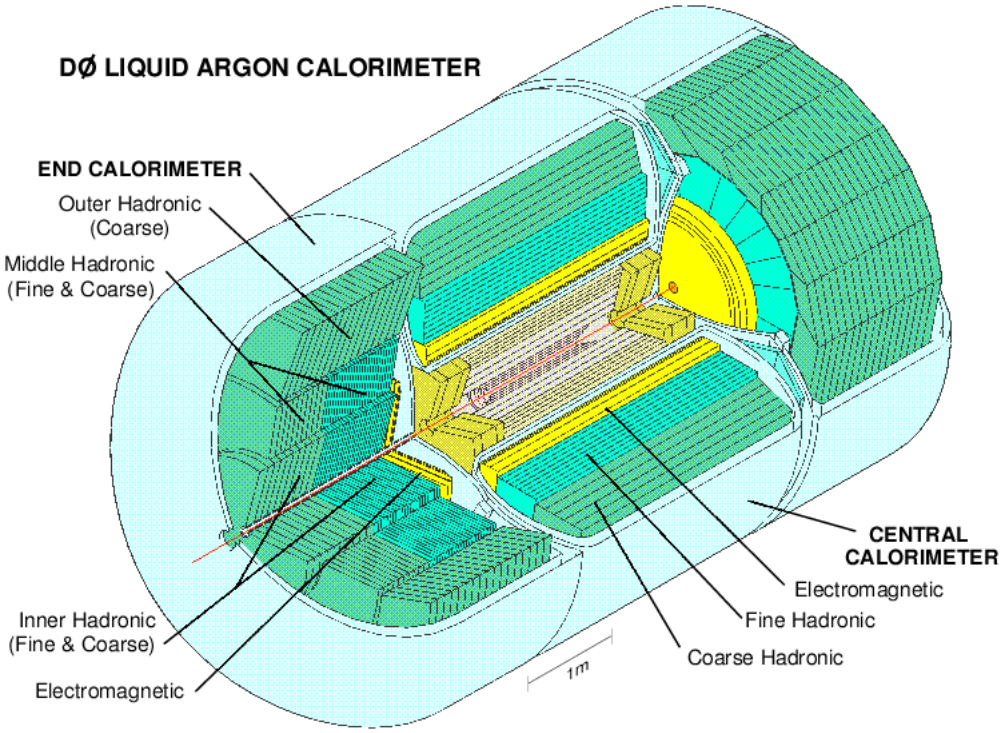

Figure 3.10. DØ calorimeter. Adapted from [2].

which measure the ionization created by the showering particles in liquid Argon. Absorbtion plates are grounded and the resistive surfaces of the signal boards are connected to high voltage (typically 2 kV). Signal boards are made of two 0.5 mm G-10 sheets covered with resistive epoxy coating. From the inside they sandwich copper readout pads, as in Figure 3.12. Several such pads at approximately the same η and ϕ are combined together in depth to form a readout cell. There are 4 layers or readout cells in the electromagnetic section (EM1-EM4), 3 layers in the fine hadronic section in the CC, and 4 layers in the EC, see Figure 3.11. The electromagnetic layers contain the electromagnetic showers, since their 65.6 mm total thickness of uranium is over 20 electromagnetic radiation lengths, while the two hadronic calorimeters make up about 6.4 hadronic interaction lengths, thus

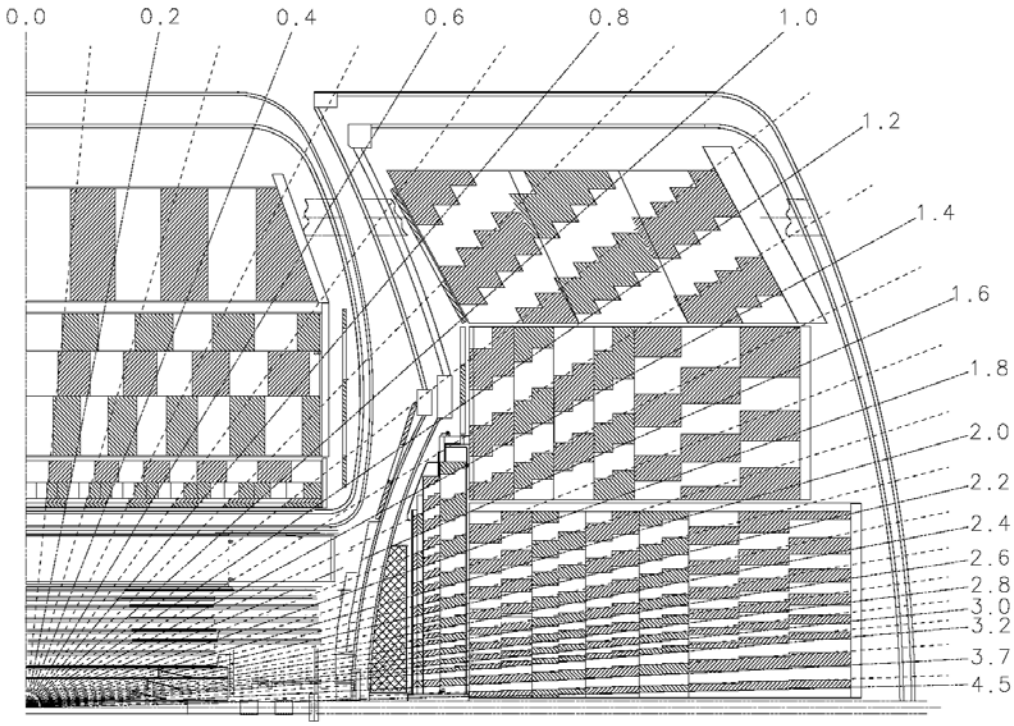

Figure 3.11. Schematic view of a portion of the DØ calorimeters showing the transverse and longitudinal segmentation pattern. The shading pattern indicates cells grouped together for signal readout. The rays indicate pseudorapidity intervals from the center of the detector. Adapted from [16].

containing nearly all of the hadronically showering particles.

A typical calorimeter readout cell has size $\delta\eta \times \delta\phi = 0.1 \times 0.1$, except for the EM3 layer, which has double the granularity $\delta\eta \times \delta\phi = 0.5 \times 0.5$, as shown in Figure 3.11. The readout cells are grouped together into pseudo-projective towers, with each tower subdivided in depth. Centers of the cells lie on the rays of increasing shower depth, but the cell boundaries are aligned perpendicular to the absorber plates.

The region between $0.8 < |\eta| < 1.4$ is not covered properly by the three cryostats. There is substantial unsampled material in this region degrading the energy reso-

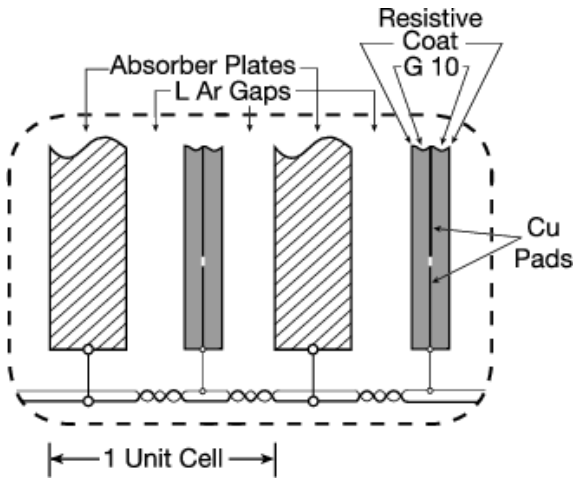

Figure 3.12. Calorimeter unit cell. Adapted from [16].

lution. Additional layers of sampling are provided to address this problem. There are single cell layers within the CC between $0.75 < |\eta| < 1.2$ and the EC between $1.0 < |\eta| < 1.3$ called massless gaps (MG), and a scintillator sampling layer attached to the exterior surfaces of the EC, covering $1.1 < |\eta| < 1.4$, called the intercryostat detector (ICD). The scintillating tiles match the calorimeter readout cell size, Figure 3.11.

Calorimeter readout is accomplished in three principal stages. At the first stage, signals from the detector are transported to charge preamplifiers located on the cryostats via low impedance coaxial cables. At the second stage, signals from the preamplifiers are transported by the twisted-pair cables to the analog signal shaping and storage circuits on baseline subtractor (BLS) boards. Baseline subtraction is necessary, for example, for removal of the signal pileup, because the electron drift time through the 2.3 mm liquid argon gap is approximately 450 ns, longer than the bunch spacing of 396 ns. The precision signals from the BLS's are transmitted through an analog bus and driven by analog drivers over 130 m of twisted-pair cables to ADC's, Figure 3.13. These signals participate in the Level 3 trigger decision (Sec-

tion 3.2.6) of the data acquisition system and are stored to tape. The preamplifiers and BLS's are completely new for Run II, and were necessary to accomodate the significant reduction in the Tevatron bunch spacing. There are 55,296 calorimeter electronics channels to be read out; 47,032 correspond to the channels connected to the physical readout modules in the cryostats.

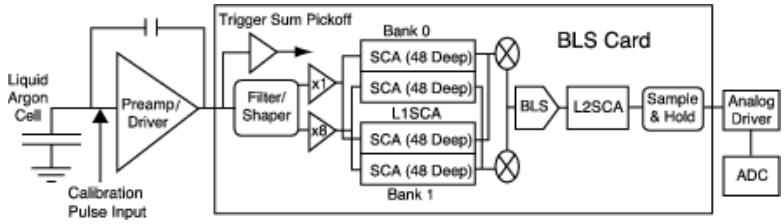

Figure 3.13. Schematic of the calorimeter readout electronics. Adapted from [16].

3.2.5 Muon System

Muons in the range $1 < p_T < 1000$ GeV have very low energy loss [20] in matter and sufficient lifetime to pass through the calorimeter. A dedicated muon system outside the calorimeter is used for muon measurement and triggering. It consists of the central muon system with proprotional drift tubes (PDT), central scintillation counters, toroidal magnets, retained since Run I, and a completely new forward muon system. The central muon system provides coverage up to $|\eta| \lesssim 1$ (central region), and the forward muon system extends it to $|\eta| \approx 2$ (forward region), see Figure 3.14.

The central muon system consists of an 1.8 T toroidal magnet, 3 layers of drift chambers located inside (layer A) and outside the toroid (layers B and C), cosmic cap and bottom scintillation counters, and the Aϕ scintillation counters, Figures 3.15, 3.16.

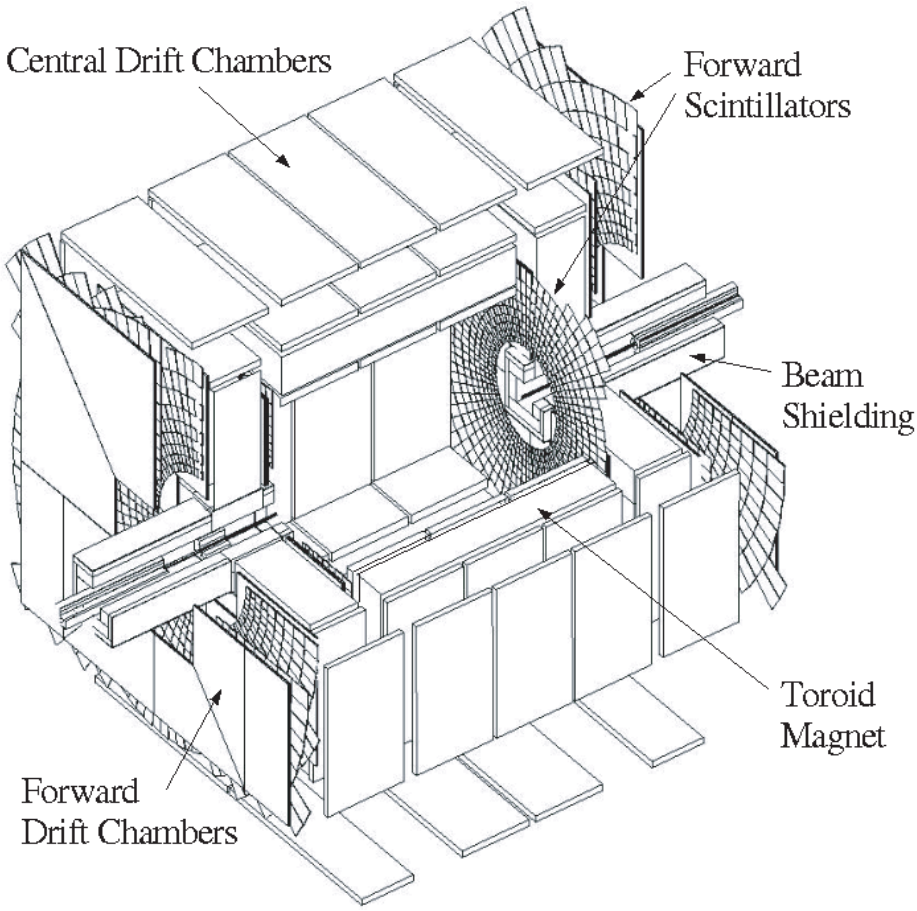

Figure 3.14. The DØ Muon System. Adapted from [9].

The toroidal magnet allows a stand-alone muon momentum measurement. It is useful for having a low p_T cut off in the Level 1 muon trigger (Section 3.2.6); it also allows cleaner matching with central detector tracks, rejects K/π decays, and improves momentum resolution for high p_T muons.

Approximately 55 % of the central region is covered by 3 layers of PDT's; close to 90 % is covered by at least two layers, Figure 3.5. The drift chambers are large, typically 2.8×5.6 m^2, and made of rectangular extruded aluminum tubes. The PDTs outside the magnet have three decks of drift cells; the A layer has four decks with the exception of the bottom A-layer PDT's which have three decks. The cells

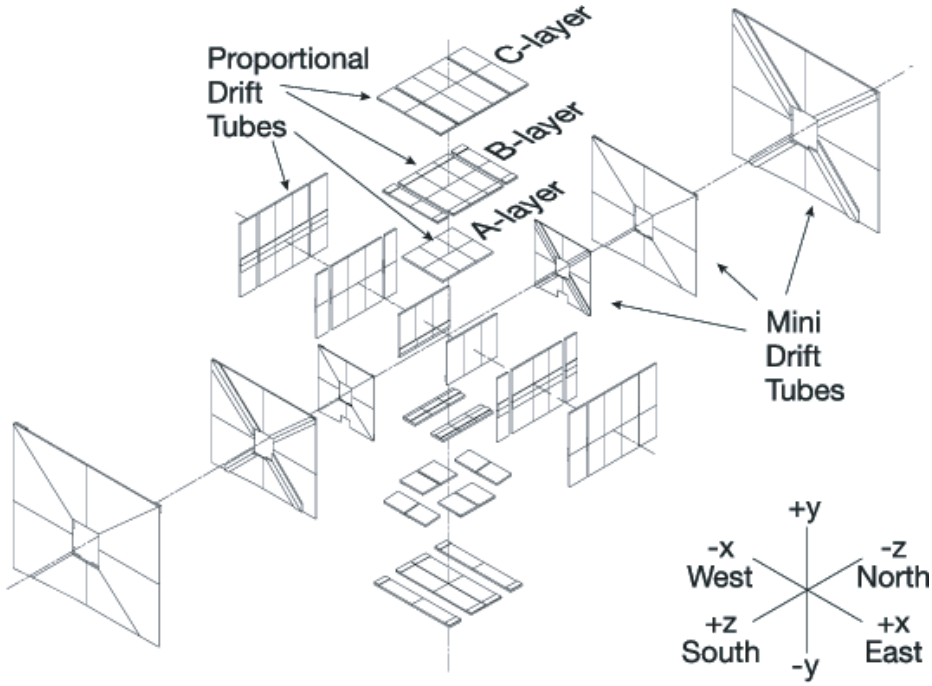

Figure 3.15. The DØ Muon System, PDT and MDT. Adapted from [16].

are 10.1 cm across; typical chambers are 24 cells wide and contain 72 or 96 cells [16], Figure 3.15. Each cell contains a wire in the center, kept at 4.6 kV, and two vernier cathode pads, above and below the wire, with 2.3 kV applied to each. Wires are paired within a deck and are read out at the end of each chamber.

The Aϕ scintillation counters cover the A-layer PDT's in the azimuthal angle ϕ, and are located between the calorimeter and the toroid. They provide a fast detector for triggering and identifying muons and for rejecting out-of-time backscatter from the forward direction. The cosmic cap and bottom counters are installed on the top, sides and bottom of the outer layer of the central muon PDT's. They provide a fast timing signal to associate a muon in a PDT with the appropriate bunch crossing and discriminate against the cosmic ray background, Figure 3.16.

The forward muon system consists of 3 layers of Mini Drift Tubes (MDT) for

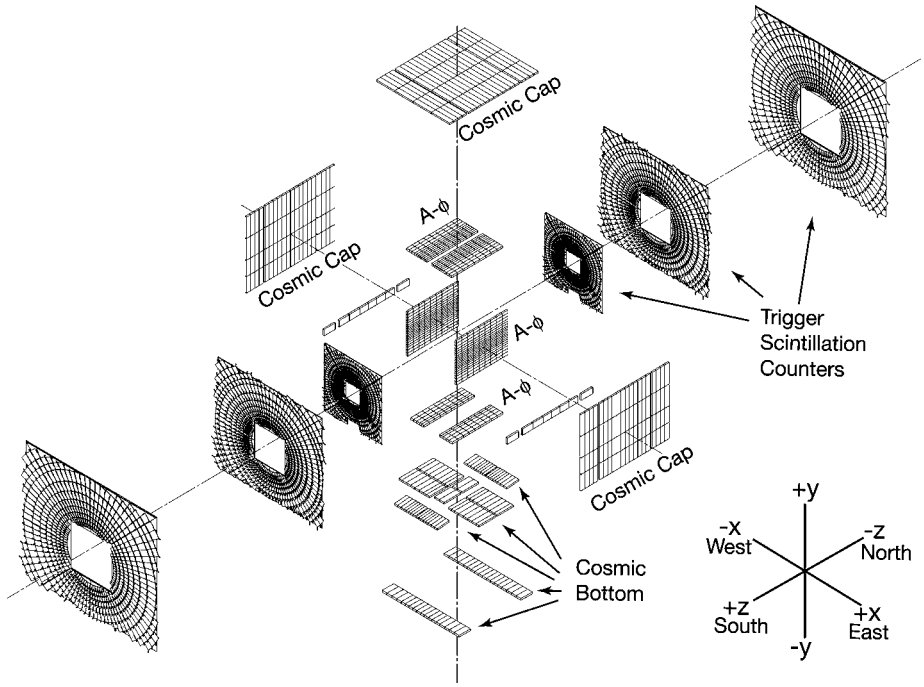

Figure 3.16. The DØ Muon System, Scintillators, Cosmic Cap, Bottom counters. Adapted from [16].

muon track reconstruction, three layers of scintillation counters for triggering on the events with muons, and shielding around the beam pipe. MDT's were a choice for their short electron drift time (132 ns), that would allow three times more beam bunches, good coordinate resolution (≈ 1 mm), radiation hardness, high segmentation, and low occupancy. MDT layer A is inside the forward toroidal magnet and layers B and C are outside. Layer A consists of four planes of tubes mounted along the magnetic field lines; layers B and C have 3 planes of MDTs (Figure 3.15), each divided into 8 octants. An MDT tube consists of eight cells, each with a 9.4×9.4 mm^2 internal cross section and a 50 μm W-Au anode wire in the center. The entire MDT system contains 48,640 wires; the maximum tube length is 5,830 mm in layer C.

3.2.6 Trigger System and Data Acquision

Reconstruction of products of every collision would be an enormous task and would require writing to tape several hundred gigabytes of information per second. Moreover, only few of these events have significant physical interest. Both these circumstances require installation of a multi-level trigger system, where each succeeding level examine fewer events but in greater detail and with more complexity. Increasing the luminosity and interaction rates requires a more sophisticated trigger system than in Run I.

The new trigger system consists of three distinct levels. Level 1 (L1) comprises a collection of hardware trigger elements that provide a trigger accept rate of about 2 kHz. Level 2 (L2) uses detector-specific preprocessing engines and a global stage processor (L2Global) to form a trigger decision based on individual objects and correlations in physical signatures across detector subsystems. The L2 system reduces the trigger rate by a factor of about two, to 1 kHz. The data acquisition system (L3DAQ) transports detector component data, accepted by L1 and L2, from the readout crates to the processing nodes of the Level 3 (L3) filtering farm. L3 software algorithms reduce the rate to about 50 Hz, and these events are recorded for the offline reconstruction [16], Figure 3.17.

Trigger framework (TFW) gathers digital information from each of the L1 trigger devices like the calorimeter trigger (L1Cal), central track trigger (L1CTT), and muon system trigger (L1Muon), and decides if a particular event is to be accepted for further examination. In addition, it coordinates various vetoes that can inhibit triggers, and implements prescaling of triggers too copious to pass on without rate reduction. All events waiting for a L1 trigger decision are pipelined and make only a minimal contribution to the deadtime. At the level of data acquision, the detector is divided into 128 geographic sectors, each served by a serial command link (SCL).

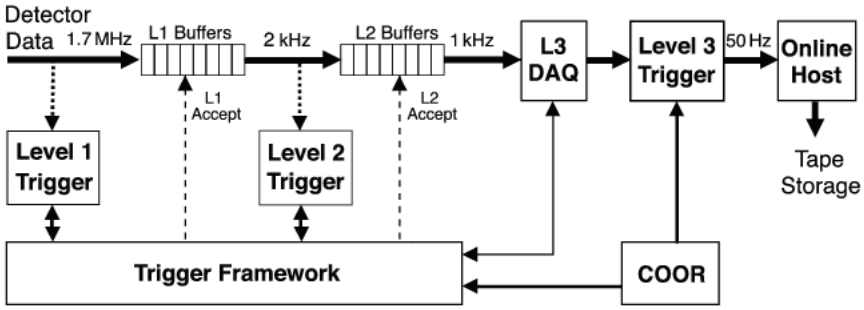

Figure 3.17. Schematic of the DØ trigger and data acquisition systems. Adapted from [16].

Typical geographic sectors area detector front-ends, but other systems like TFW readout are also geographic sectors. Each geographic sector receives an L1Accept from the TFW over the SCL, followed by L2Accept or L2Reject from the L2Global, Figure 3.18.

The overall coordination and control of the DØ triggering is handled by the COOR software package, Figure 3.17. COOR interacts directly with the trigger framework (L1 and L2 triggers) and with the DAQ supervising systems (L3 triggers).

The L3DAQ system has a designed bandwidth of 250 MB/s, corresponding to and average event size of about 200 kB and a L2 accept rate of 1 kHz. It is built around a single Cisco 6509 [21] ethernet switch. All nodes in the system correspond to digital readout VME crates (up to 63) with a single readout commodity computer (SBC), each. SBC reads out VME modules and sends the data to one or more farm nodes. An event builder process on each farm node builds a complete event from event fragments and makes it available to L3 trigger filter processes.

The fully programmable software trigger L3 performs a limited reconstruction of events. Its decisions are based on complete physics objects as well as relationships between such objects. Candidate physics objects are generated by filter tools. All

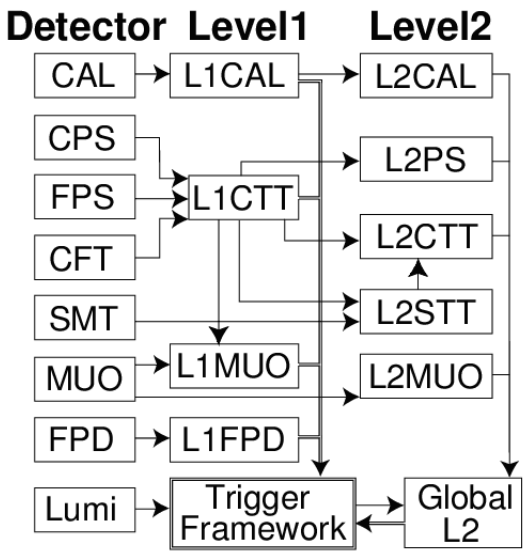

Figure 3.18. Block diagram of DØ L1 and L2 trigger systems. Adapted from [16].

tools cache their results to expedite possible multiple calls. Individual calls to the tools are made by filters that define specific selection criteria. Filter results are keyed for access by other filters, so that a single L3 condition can include blocks of filters defined in a script. When all the filters in a script are satisfied, the L3Accept is made and the event is sent to the host cluster to be recorded.

CHAPTER 4

ANALYSIS

One of the primary goals of this analysis is to obtain an accurate simulation of the response of the DØ detector to the propagation of the particles, produced as a result of a hypothetical Higgs boson decay. Along with the other products of the $p\bar{p}$ collisions in a theoretical model interaction, it should be compared to the response of the detector in the events recorded by the data acquisition system.

4.1 Reconstruction of Physics Objects at DØ

Although a meaningful analysis can be in principle performed on the detector information, raw data are usually reconstructed centrally at DØ to form physics candidate objects which have properties corresponding to the standard model particles. Sophisticated DØ reconstruction software combines electronics response into primary objects such as calorimeter clusters, charged particle tracks, and missing transverse energy, and uses these components along with the other detector information to build higher level objects, representing photons, electrons, muons, tau leptons, and hadronic jets.

Reconstruction solves part of the problem of separating physics particles coming from an inelastic $p\bar{p}$ collision from outside backgrounds such as cosmic rays, and detector noise. It has to make assumptions about the detector response to the propagation of physical particles, including their interference, and the instrumental

background, representing the detector noise. Those particles that can not be distinguished from the background are lost to inefficiency. Reconstruction also provides, along with the object tag, sufficient flexibility, by supplying parameters that can be varied in order to obtain a higher purity of the object (probability of being a real physical particle), or higher efficiency of object reconstruction after passing the cuts. Typically, an analysis tightens the cuts to obtain higher purity, and loosens them to obtain higher efficiency.

4.1.1 Luminosity

First of all, we need a handle on how many, if any, inelastic collisions occurred during a particular beam crossing. Luminosity scintillators serve the purpose of detecting coincident particles originating from the interaction region. Timing resolution of the scintillators ($\lesssim 0.3$ ns) allows the collision point along the beam axis to be localized with the accuracy of about 10 cm. Beam halo particles are rejected by requiring the collision point to be within a specified interaction region.

The instantaneous luminosity is measured by counting the fraction of crossings with no $p\bar{p}$ coincidences detected. The probability of this to happen is equal to:

$$P(n < 1) = e^{-\mu}, \tag{4.1}$$

where μ is the average number of inelastic collisions per beam crossing:

$$\mu = \mathcal{L}\sigma_{eff}/r, \tag{4.2}$$

where $\mathcal{L}$ is the instantaneous luminosity, σ_{eff} is the effective inelastic $p\bar{p}$ cross section, corrected for acceptance and efficiency, and r is the bunch crossing rate. Thus, the instantaneous luminosity is measured to be:

$$\mathcal{L} = -(r/\sigma_{eff}) \ln(P(n < 1)) \tag{4.3}$$

The crossing rate, r, is measured very well and is equal to 2.5 MHz. The effective cross section dominates the uncertainty of the luminosity measurement and is approximately 43 mb. This value is also corrected for the luminosity detector inefficiency (about 91%) and acceptance (about 97%).

Approximately each minute a *luminosity block* is written to the database to indicate the average measured luminosity for this time period and quality of the performance of the data acquisition system and detector components.

The integrated luminosity information is used to properly normalize the event yields in the Monte Carlo theoretical signal and background models.

4.1.2 Tracking and Primary Vertexing

Charged particle track reconstruction involves identification of clustered hits in the SMT and CFT detectors and building patterns of particle trajectories through them.

SMT hits are clustered by combining charge information from groups of adjacent silicon strips that have signal information above the threshold. Different ways of clustering exist. Depending on how efficient the tracking algorithm is, one-sided or two-sided ("stereo") strip information is used. Stereo clustering provides a lower fake rate, while one-sided information gives a better efficiency; however, the tracking algorithm has to deal with huge combinatorics of tracking hypotheses. CFT hits can be clustered in the doublet layers into 2D-hits or in superlayers, with 1 axial doublet and 1 stereo (u or v, see Section 3.2.2) doublet into 3D-hits.

Track reconstruction chooses among track candidates created by two competing algorithms, Histogram Track Finding (HTF) [22] and Alternative Algorithm (AA)

[23].

The histogramming technique uses the fact, that trajectories of particles in a perfect solenoidal magnetic field are 3-dimensional helices. Therefore, if the candidate hits are projected onto the transverse plane, when transformed into the track curvature and incident angle coordinates, they give rise to a bunch structure, intersecting nearly at one point, which signifies that a charged particle track is found. Roughly speaking, the closeness of the intersection points for this bunch is a measure of the quality of the track fitting. This HTF technique is illustrated in Figure 4.1. It is also called the Hough transform technique [24].

AA tracking starts with three 2D-hits from the SMT barrels or disks by forming an initial track hypothesis. Hits are selected starting from the innermost layer and going outward. Track hypothesis is extrapolated to the next SMT or CFT layer, and a new track hypothesis is formed if there is more than one hit on the next layer compatible with a low χ^2 fit. If the next layer does not contain a hit within a specific expectation window, such hit is missed. There are certain limitations imposed on how many overlapping track hypotheses should be considered, how many missed hits are acceptable, to keep a particular track hypothesis in the pool. The SMT seeded tracks have the advantage of describing well the original parameters of the interaction. For example, they can show whether the particle originates from a hard scattering, decay or interaction with the detector material. The disadvantage is that some tracks that do not have three hits in the SMT are missed, and those represent a significant part of all track candidates. On the other hand, CFT seeded tracks are plagued by very large combinatorics between the axial and stereo hit association. This is why knowledge of a primary interaction vertex is crucial in reducing the fake rate in the CFT seeded tracks and the whole track pool.

Tracking information is used to find primary vertices. These are locations, where

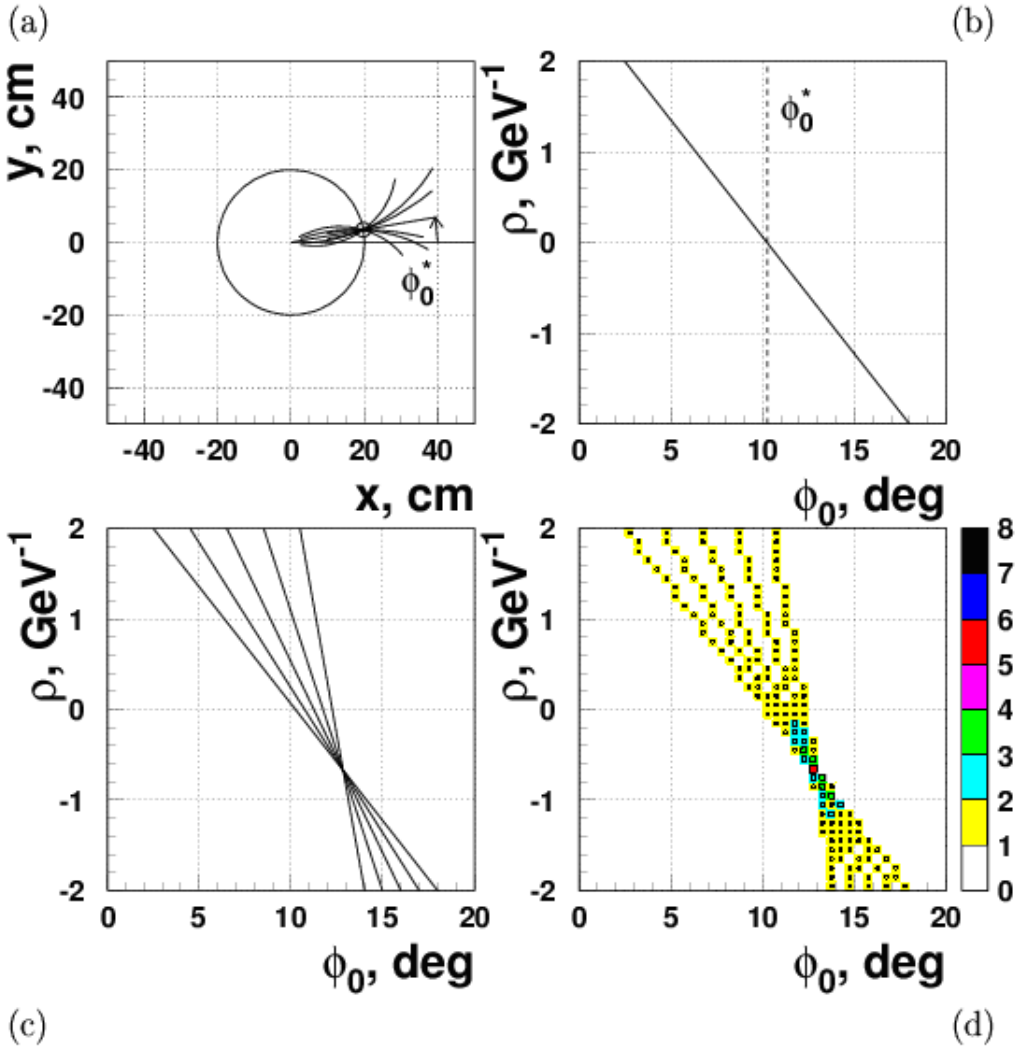

Figure 4.1. The Hough transform, used by the HTF track reconstruction algorithm, applied to a toy simulation of a single 1.5 GeV track coming from the center of the detector. a) shows the family of trajectories (circular arcs) through a given hit. b) shows the line in Hough transformed space corresponding to the locus of points which corresponds to each trajectory through the given hit. c) shows the family of lines corresponding to each of the five hits on the single 1.5 GeV simulated track. d) shows the histogram of the 5 Hough transformed hits. The peak in the histogram corresponds to the parameters (curvature and angle) of the original 1.5 GeV simulated track. Adapted from [9].

$p\bar{p}$ hard scattering collisions occur within the interaction region, as opposed to the minimal bias interactions or decay vertices. Minimal bias vertices can be understood as points where a non-central collision takes place and no significant scattering of the $p\bar{p}$ components is observed. Products of such collisions mostly fly in the forward direction.

Primary vertices can be fitted for any set of tracks. Using an iterative procedure, primary vertex position is found initially with the SMT seeded tracks. Then, CFT seeded tracks (starting with 3 2D-hits in the CFT) are found with an additional requirement to pass close to the primary vertex. The track pool is replenished with these additional tracks, and the procedure is repeated.

Vertices are fitted by first clustering the tracks within 2 cm along the z-direction. Tracks are required to have $p_T > 0.5$ GeV. A tear-down Kalman [25] vertex fitter fits tracks to a common vertex and removes tracks that contribute the highest χ^2 to the fit. The final value for the fit χ^2/n.d.o.f. is kept under 10. After that, tracks in each z-cluster are sorted with respect to their distance of closest approach (DCA) to the beam spot obtained during the tear-down fitting. A common vertex for these tracks is sought for in an adaptive Kalman procedure [26], where each track χ^2 contribution is weighted by a Fermi function:

$$w_i = \frac{1}{1 + e^{(\chi_i^2 - \chi_c^2)/2T}}, \tag{4.4}$$

where χ_i^2 is the ith track χ^2, χ_c^2 is the cutoff value, and T is a sharpness parameter. In the last step a probability for a vertex to be a minimum bias vertex is calculated and the vertex having the smallest probability is chosen as the primary.

Tracks that have a small impact parameter with respect to the primary vertex are considered first in the updated pool. CFT seeded tracks are extrapolated to the SMT. The tracks are passed through a fitter algorithm [27] using the Kalman

filtering procedure [25]. The fitter algorithm makes use of the DØ track propagator [28], which refines track parameters taking into account the solenoid magnetic field and interactions of the charged particles with the detector material. An illustration of a DØ event with reconstructed tracks is shown in Figure 4.2.

4.1.3 Calorimeter Energy Clusters

Reconstruction of electrons, photons, taus, and jets begins with identifying calorimeter energy clusters. Depending on the type of cluster needed, two algorithms are used: simple cone algorithm (SC) and nearest neighbor cell (CellNN).

Before creating energy clusters, calorimeter cells are grouped into towers taking cells from successive calorimeter layers which have the same stereo angular coordinates, and their energy 4-vectors are recalculated relative to the primary vertex. The magnitude of the projection of the energy 4-vector onto the transverse plane (perpendicular to the beampipe) becomes the tower transverse energy E_T.

In the SC algorithm, towers are grouped together into clusters, starting from the highest E_T tower, if successive towers in the list happen to be in a specific stereo angular cone (coordinates are azimuthal angle ϕ and pseudorapidity η, see Section 3.2), typically $\Delta R = \sqrt{(\Delta\phi)^2 + (\Delta\eta)^2} < 0.5, 0.7$ around the seed tower. Tower E_T's have to be above some specific threshold.

Nearest neighbor algorithm utilizes cell energy information, also calculated with respect to the primary vertex, to group cells together into clusters, instead of using towers. A description of the method is given in [29]. The algorithm is used exclusively to reconstruct electromagnetic-related objects like photons, electrons, and electromagnetic subclusters of τ decays. The calorimeter electromagnetic layer EM3 has higher resolution than other calorimeter layers, see Section 3.2.4, and is best used when grouping of calorimeter cells is first performed separately for each layer,

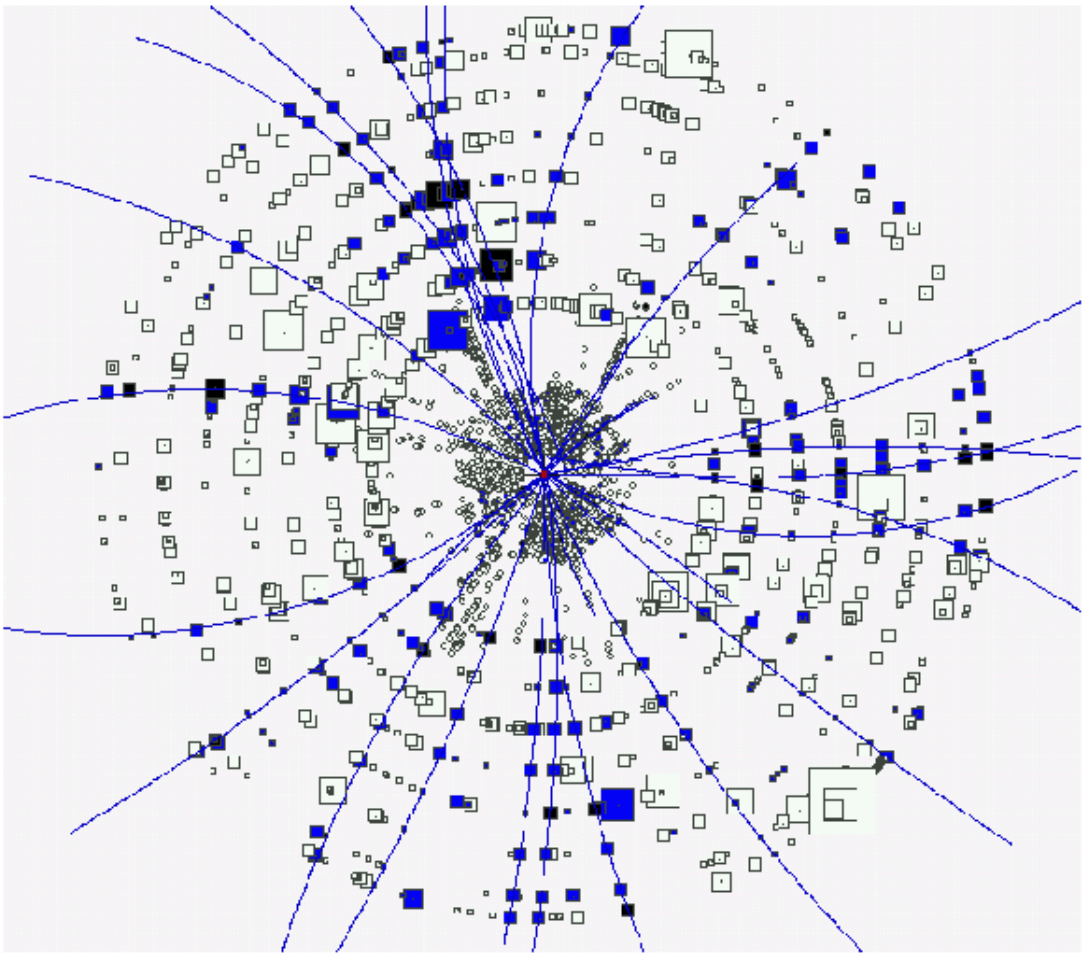

Figure 4.2. An axial view (looking down the beam-pipe) of an event recorded with the DØ inner trackers, showing the reconstructed hits and tracks. The CFT hits are square and form the 8 layers on the outside. Silicon hits are drawn as small circles, and are innermost. Hits are colored solid if they are associated with a reconstructed track. The tracks are shown as solid lines, and are curved by the solenoidal magnetic field pointing out of the page. Adapted from [9].

and then global clusters are formed by stitching together clusters from individual layers.

Both algorithms calculate the transverse energy of the cluster as the vector sum of the transverse energy of its components, and the cluster axis as E_T weighted sum of the centers of its components.

4.1.4 Reconstruction of Electromagnetic Objects

Electromagnetic object (electron and photon) reconstruction considers information from tracking and calorimeter energy clusters, built via either SC algorithm or CellNN algorithm, with a typical cone size of 0.4. In case of electrons, a track should be identified, pointing to the electromagnetic cells in the calorimeter cluster. Electromagnetic objects require that a significant fraction of their energy be deposited in the electromagnetic layers of the calorimeter, typically greater than 0.9, and their shower shapes be consistent with those of electrons and photons.

Shower shapes are tested using 7 shower variables as in the formula:

$$\chi^2_{cal} = \sum_{i,j=1}^{7} (x_i - \bar{x}_i) M^{-1}_{ij} (x_j - \bar{x}_j), \tag{4.5}$$

where the χ^2_{cal} is required to be less than some specific value, typically 50, and M_{ij} is the covariance matrix, calculated using model electrons:

$$M_{ij} = \frac{1}{N} \sum_{n=1}^{N} (x^n_i - \bar{x}_i)(x^n_j - \bar{x}_j), \tag{4.6}$$

where the sum is taken over the simulated or test beam electron sample. Also an electromagnetic isolation condition is imposed on the shower shape, as a cut on the electromagnetic fraction of the cluster energy in the hollow cone $0.2 < \Delta R < 0.4$, typically < 0.15 for electrons:

$$f_{iso} = \frac{E_{EM}(\Delta R < 0.4) - E_{EM}(\Delta R < 0.2)}{\Delta E_{EM}(R < 0.2)} \tag{4.7}$$

Electrons are also charactecterized by a likelihood, defined as a ratio of probabilities:

$$\mathcal{L} = \frac{P_{sig}(\mathbf{x})}{P_{sig}(\mathbf{x}) + P_{bkg}(\ \mathbf{x})}, \tag{4.8}$$

where $\mathbf{x}$ is a vector of likelihood parameters, which includes some of the shower shape parameters and some track parameters. A product of individual probabilities is taken as the overall probability, disregarding the correlations between the parameters:

$$P_{sig/bkg}(\mathbf{x}) = \prod_{i=1}^{K} P^{i}_{sig/bkg}(x_i), \tag{4.9}$$

where K is the number of parameters. In this analysis, electron definition with the likelihood $\mathcal{L} > 0.85$ is used for exclusion purposes.

4.1.5 Muon Reconstruction

Identification of muons runs over hit information in the muon system, see Section 3.2.5, and tracking information obtained from the charged particle reconstruction, see Section 4.1.2. Combinations of wire chamber and scintillator hits, consistent with the muons originating from the interaction region, are matched to the tracks in the tracking detector. In a particular case, when a muon candidate is matched to a track, its transverse momentum p_T is taken from the track parameters. A muon can also be characterized as isolated or non-isolated using two parameters:

$$I_{cal} = E(\Delta R < 0.4) - E(\Delta R < 0.1), I_{trk} = \sum p^{trk}_{T,(\Delta R<0.5)}, \tag{4.10}$$

where I_{cal} is *calorimeter isolation*, energy in a hollow cone $0.1 < \Delta R < 0.4$, and I_{trk} is *track isolation*, the sum of the p_T's of tracks, not associated with the muon, in a cone $\Delta R < 0.5$.

This analysis uses a $LOOSE$ definition of a muon canditate, where a muon is required to have:

- Scintillator and wire hits both inside and outside the muon toroid
- Scintillator hit times must be within a 10 ns window around the bunch crossing time
- Muon has to be matched to a central track, which has a distance of closest approach DCA$<$ 0.2 cm, see Section 4.1.2, in case it does not have hits in the SMT, or DCA$<$ 0.02 cm otherwise.

Monte Carlo simulated events, used to model some of the backgrounds for this search, generally have muon reconstruction efficiency higher than the one observed in the data with a tag-and-probe method. This method considers a pair of muons most likely coming from a Z boson decay, where one high quality muon is taken as a tag, and the other one as a probe. Muon trigger efficiencies are also studied like this. Therefore, Monte Carlo acceptances are corrected by scale factors, corresponding to the difference, typically 0.99 for the muon reconstructed in the muon system, and 0.96 for the track associated with the muon from the central tracking detector. These correction factors are typically parameterized with respect to the angular coordinates η, ϕ in the muon system, see Figure 4.3, or with respect to pseudorapidity, calculated in the CFT, and ϕ, for different bins in the z direction, see Figure 4.4.

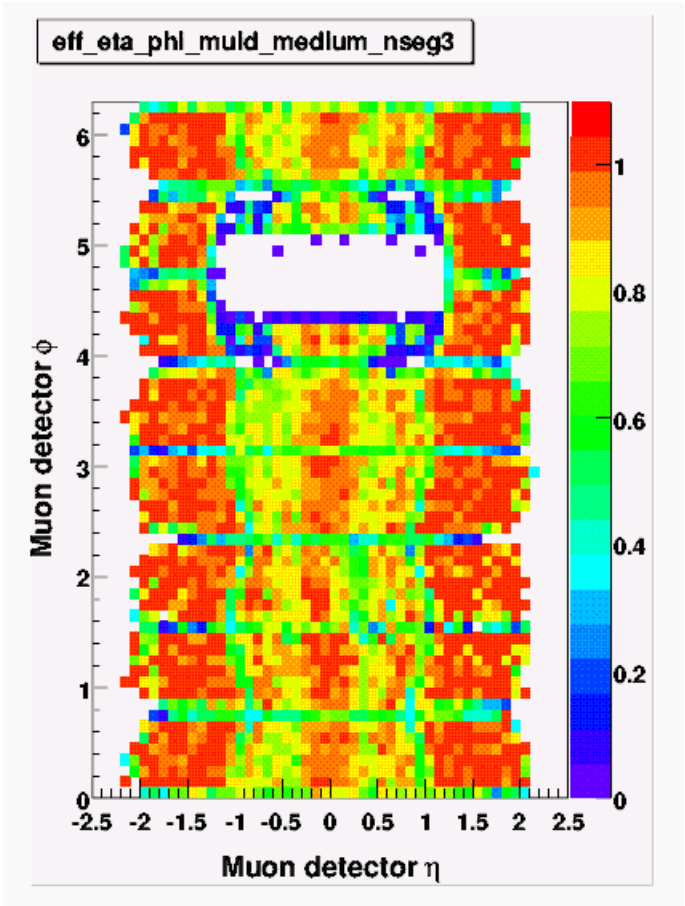

Figure 4.3. Muon reconstruction correction factor as a function of muon detector η and ϕ. Adapted from [30].

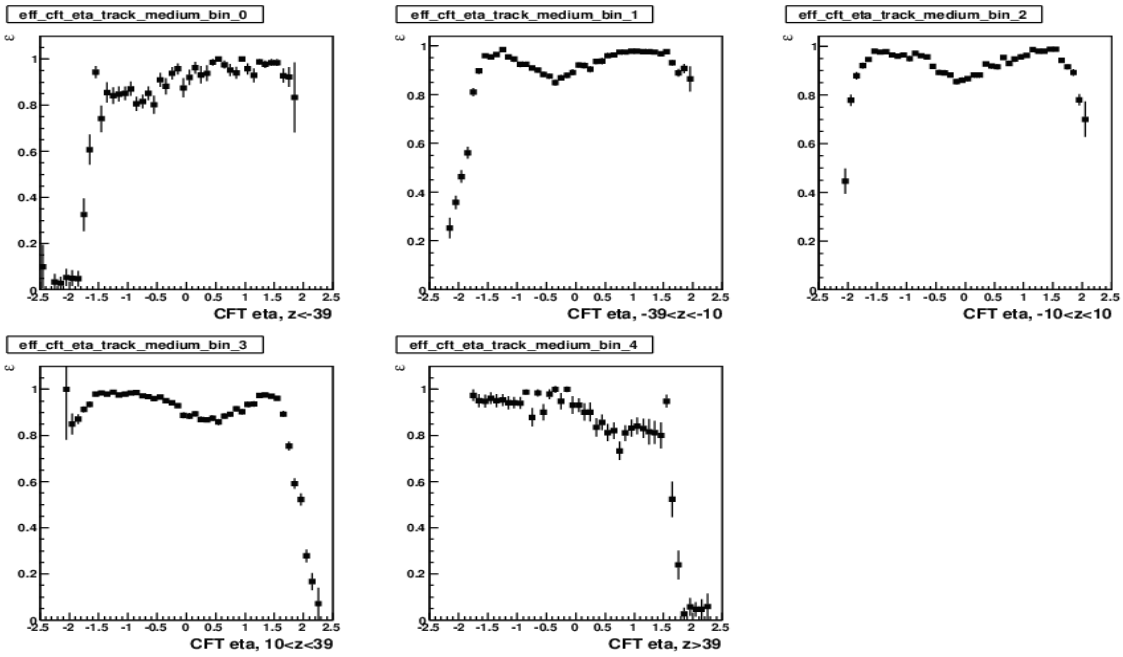

Figure 4.4. Muon track reconstruction correction factor as a range of the track z-position. Adapted from [30].

4.1.6 Jet Reconstruction

Strongly interacting elementary particles never exist in nature in an unbound state. The only exception is the top quark, which has a lifetime less than the typical hadronization timescale. Schematically, the evolution of strongly interacting particles can be described as a production of a single *parton*, gluon or quark, in a hard scattering collision (parton-jet), and hadronization stage (particle jet), where gluon splitting takes place. Quarks form hadronic bound states, heavier flavor quarks undergo weak decays, giving birth to long-lived particles, mostly pions and kaons, as a result. All these transformations happen in a relatively narrow bundle, called a jet. Jets are studied as a physical object by their energy deposition in the calorimeter, paths of the contributing charged particles in the tracking detector, and registering a passage of a muon through the muon system, if a heavier flavor quark decay takes place, see Figure 4.5.

This analysis uses jets reconstructed in a cone $\Delta R < 0.5$ with the help of the DØ "improved legacy cone" algorithm [31]. Algorithm constructs "seed" preclusters from all calorimeter towers with the transverse energy $E_T > 0.5$ GeV that fit into a smaller cone of $\Delta R < 0.3$ and have total $E_T > 1$ GeV. An iterative procedure is used to find $proto - jets$ in a larger cone around the seeds, where at each step the tower E_T weighted position of the proto-jet axis is recalculated together with the new value for the proto-jet E_T, until a stable position for the axis is reached [32]. The overlapping proto-jets are merged if the E_T contained within the overlapping region is more than a half of the E_T of each proto-jet, and are split otherwise. The E_T of the obtained jets is recalculated anew.

The jet E_T is a quantity that participates in many calculations involving jets, therefore its value is corrected for the calorimeter response and energy reconstruction inefficiency (because of the algorithmic cut on the size of the cone, etc.) in order to

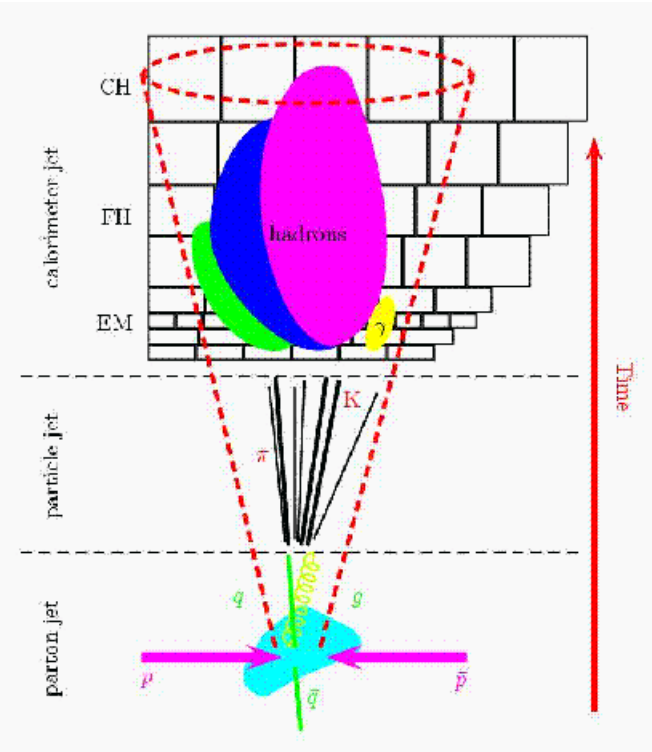

Figure 4.5. Evolution of a parton coming from a hard scattering process into a jet in the calorimeter. Adapted from [30].

obtain a number that would be close to the underlying particle jet E_T [33].

Jet transverse energy is corrected according to the formula:

$$E_{jet}^{ptcl} = \frac{E_{jet}^{raw} - E_O}{R_{jet} \cdot S_{jet}} + (E_\mu), \tag{4.11}$$

where E_{jet}^{ptcl} is the corrected jet energy, E_{jet}^{raw} is the jet energy measured in the calorimeter, E_O is the offset energy, R_{jet} is the response correction, S_{jet} is the showering correction, and E_μ is the muon energy correction.

The offset energy corresponds to the detector noise, which comes from both electronics and radioactive decay of the uranium absorber. It also contains the pile-up effect of the residual charge of previous crossings and minimum bias interactions, and has to be subtracted. Energy of the spectator particles coming from the underlying physics event is considered a part of the hard scattering event and is not subtracted. The correction is measured in minimum bias events. It grows with the number of primary vertices because of the multiple interactions within a bunch crossing, and also with the detector pseudorapidity as in Figure 4.6.

A calorimeter response correction R_{jet} is introduced due to fact that energy is lost in the material before the calorimeter as well as in the uninstrumented regions between modules, and also module-to-module inhomogeneities. It can be divided into a non-uniformity correction, depending on the detector pseudorapidity, as in Figure 4.7, and absolute response correction, depending on the jet energy, Figure 4.8. In the latter, the correction is shown as a function of the jet energy already corrected to the offset energy and response non-uniformity.

Both non-uniformity correction and absolute response correction are extracted from data using the Missing Transverse Energy Projection Fraction (MPF) method described in [33]. This method calculates the projection of the transverse momentum imbalance for the dijet and γ+jet events, in a so called "tag-and-probe" configura-

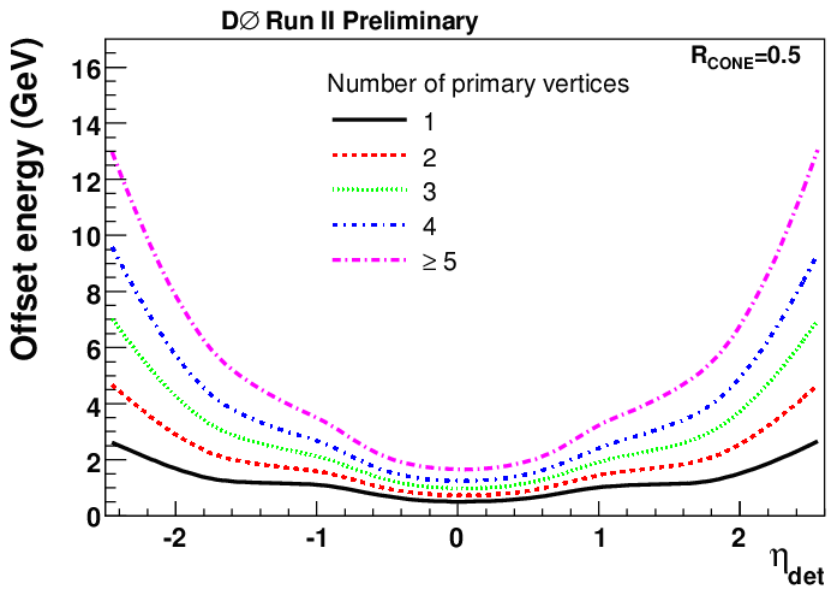

Figure 4.6. Offset energy correction for different primary vertex multiplicities as a function of the jet detector pseudorapidity. Adapted from [30].

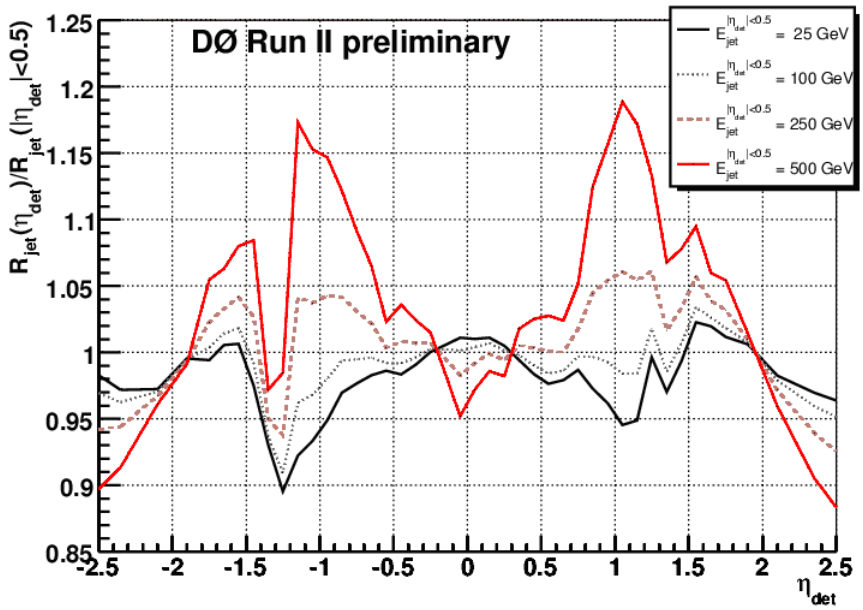

Figure 4.7. Non-uniformity correction in data as a function of jet detector pseudorapidity. Adapted from [30].

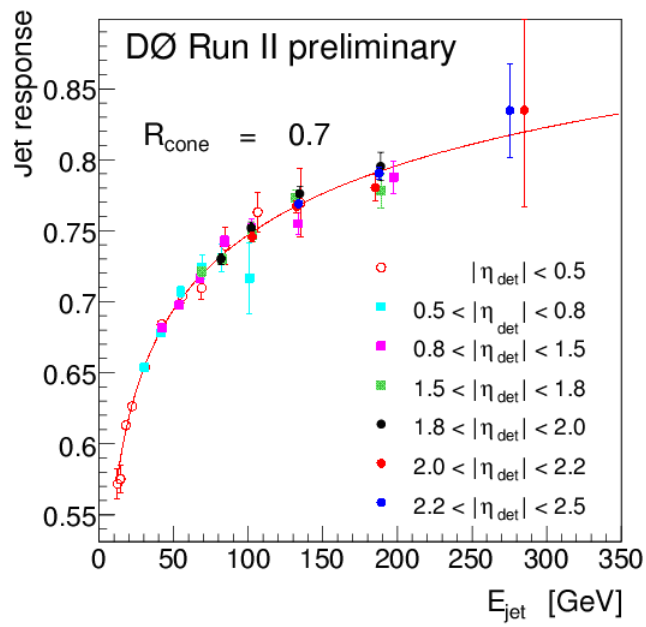

Figure 4.8. Absolute response correction in data after offset and relative response corrections as a function of partially-corrected jet energy. Adapted from [30].

tion, where the tag is a well reconstructed object in the central calorimeter, and a probe is a reconstructed jet.

Requiring the tag and the probe to be back-to-back in azimuthal angle ϕ and to be the only two objects reconstructed in the event, helps to reduce the effect of additional jets present in the event. Some of these jets may not even be reconstructed, which biases the response estimation. A schematic of the method is shown in the Figure 4.9.

Showering correction represents a reciprocal of the fraction of energy deposited inside the reconstruction cone as a result of the development of showers and finite size of the calorimeter cells, out of all energy of a particle jet. It also includes a correction for the energy deposited into the jet cone by the particles not belonging to the particle jet. In the MC, a showering correction is estimated using the full detailed information about the amount of energy deposited in each calorimeter cell

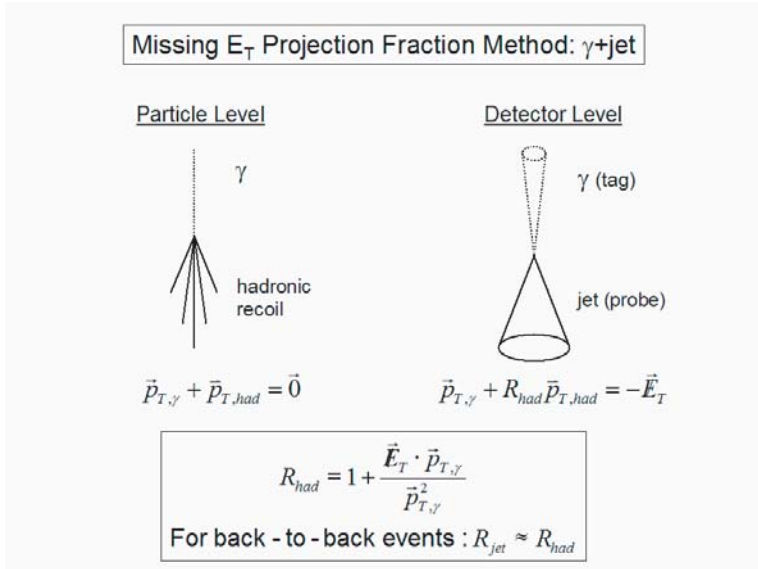

Figure 4.9. Schematic illustration of the MPF method. Adapted from [30].

by each particle in the absense of zero-bias overlay events (events, added to the MC to simulate the effect of minimum bias interactions in data), i.e no offset energy.

In data the showering correction is measured by examining the calorimeter energy distribution in annuli of increasing stereo angle $\Delta R(\eta, \phi)$, or jet energy profile. Differences between the total jet energy profile in data and energy profiles of the particle jet, underlying event and offset energy deposition into the jet cone in the MC are corrected for by fitting the data profile to the linear combination of the MC profiles. Optimal parameters for the linear combination are found in the process. Thus, the resulting showering correction in data accounts for both physics and detector effects, and is shown in Figure 4.10.

If a muon is registered within a jet cone, the jet energy is also corrected for the muon energy loss, which is necessary to accurately represent jet parameters for b-quark identification. Muon deposits only about 3 GeV in the calorimeter, therefore a large part of its energy escapes identification. Also, energy of the neutrino,

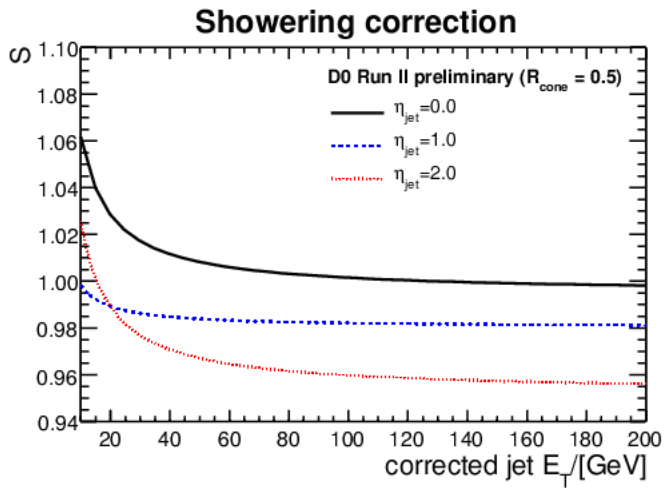

Figure 4.10. Showering correction in data as a function of corrected jet transverse energy. Adapted from [30].

associated with the production of the muon, as measured in the MC, is added to this correction. A typical fraction of the muon energy necessary to add back to the jet is shown in Figure 4.11.

Uncertainties, associated with the jet energy scale corrections, described above, are typically large and add significantly to the overall uncertainty of the analyses involving jets. Among these, absolute calorimeter response uncertainty typically dominates, as shown in the Figure 4.12.

4.1.7 B-quark identification

This analysis uses b-quark identification in combination with identification of τ-leptons as a powerful tool to suppress large QCD backgrounds. B-quark decays tend to develop a displaced decay vertex, which the tracking system is able to identify.

There are several signatures for displaced verteces that allow a measurement of either the displaced vertex position or the probability of a heavy flavor decay.

One of them is the high signed impact parameter significance with respect to

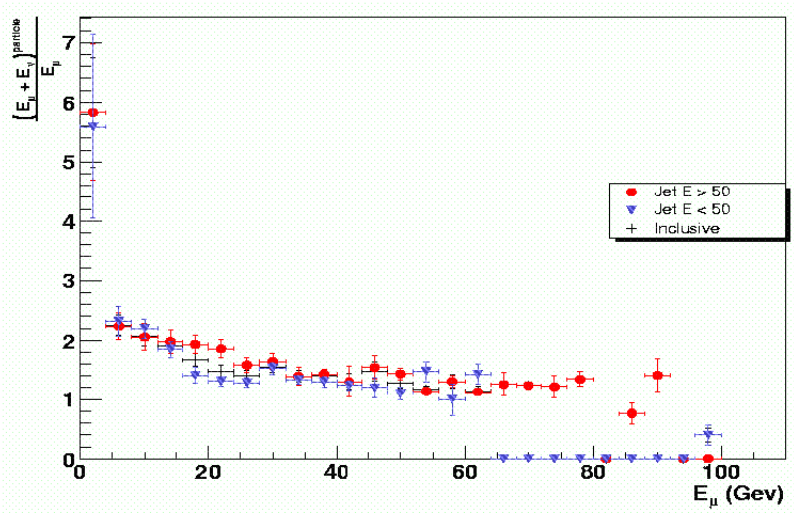

Figure 4.11. The jet correction factor for the measured muon energy associated with a jet. The fraction of the muon energy to add back to the jet is derived from simulated bjets containing muons. The correction factor is shown for low (< 50 GeV) and high (> 50 GeV) energy jets and the inclusive jet sample. Adapted from [9].

the primary interaction vertex, which is calculated by dividing the track impact parameter by its resolution, see Figure 4.13. The sign of the projection of the track impact parameter (DCA) onto the jet axis can be positive or negative. Tracks coming from a heavy flavor decay vertex tend to have a significant positive impact parameter on average.

On the other hand, a displaced vertex can be fitted using the track parameters, and its distance from the primary vertex can be estimated together with its error to form a secondary vertex decay length significance.

Several such characteritics of a possible heavy flavor decay obtained by different b-tagging algorithms are used as input variables into a Neural Network (NN) algorithm which associates a b-tagging probability with a jet [34, 35, 36]. These are summarized in Table 4.1.

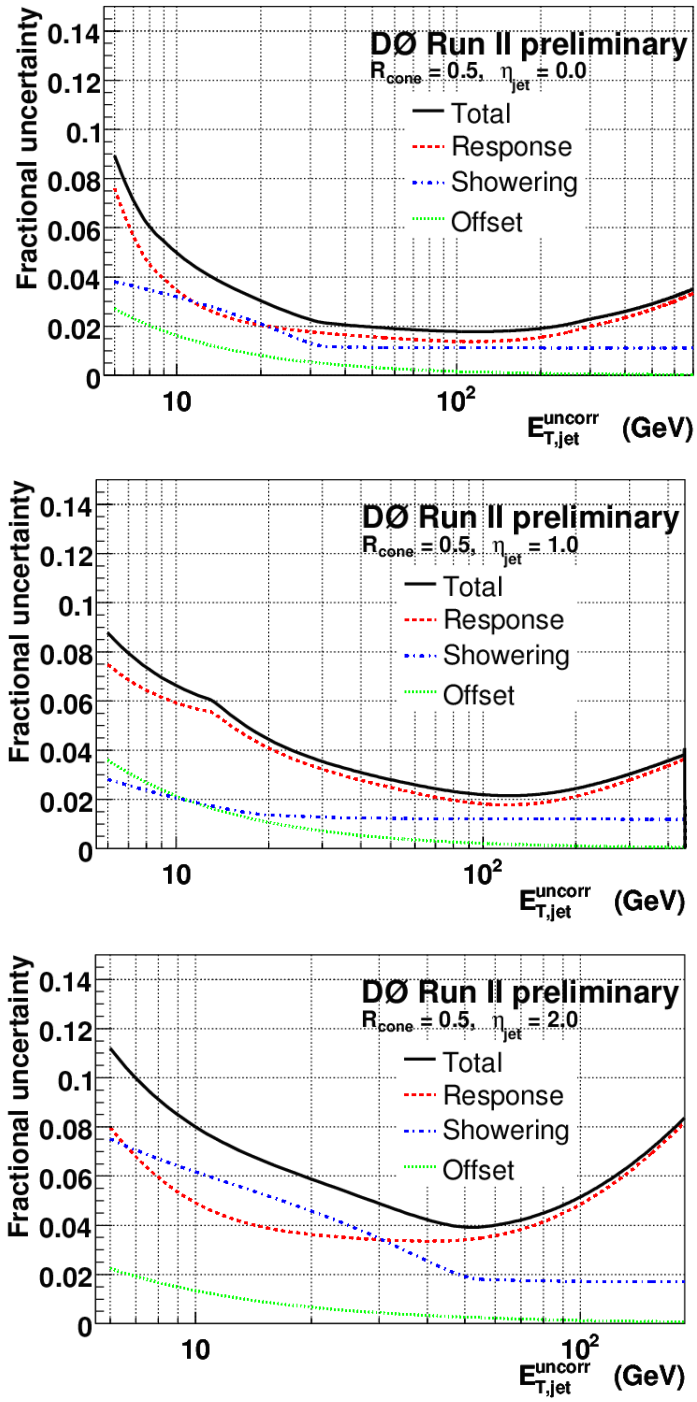

Figure 4.12. Fractional jet energy scale uncertainties as a function of uncorrected jet transverse energy, plotted for three different pseudorapidity values.Adapted from [30].

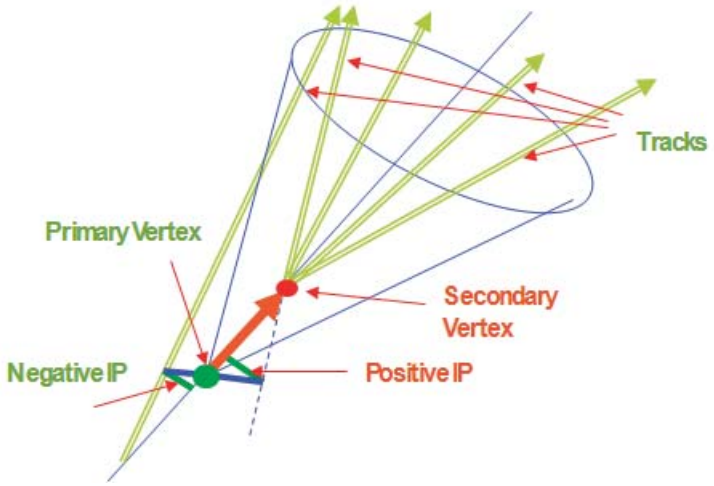

Figure 4.13. A schematic illustration of b-jet parameters.

TABLE 4.1

INPUT VARIABLES FOR THE NEURAL-NETWORK B-TAGGING ALGORITHM.

Variable	Description
SVT DLS	Decay length significance of a secondary vertex
CSIP Comb	Weighted combination of the track impact parameter significance
JLIP Prob	Probability of a jet to originate from a primary vertex
SVT $\chi^2_{d.o.f.}$	χ^2 per degree of freedom of the secondary vertex
SVT N_{tracks}	Number of tracks used to reconstruct the secondary vertex
SVT Mass	Reconstructed mass of the secondary vertex
SVT Num	Number of the secondary vertexes found in the jet

Only jets that satisfy specific conditions on the track multiplicity within the jet cone and tracks transverse momenta, can be probed for the presence of a heavy flavor decay. For instance, the number of tracks must be greater than two, there must be at least 1 track with $p_T > 1$ GeV, and all tracks must have $p_T > 0.5$ GeV, etc. Such jets are called "taggable", and the probability of a jet to satisfy these conditions is estimated in lepton+jets data, and is applied to each jet in MC [36].

Because the algorithm is not applied to the MC directly, there are several so called "working points" created with a specific cut on the NN output, a number between 0 and 1, see [35], to facilitate application of tag rate functions (TRF's), which are probabilities for a jet to have a specific working point NN cut, parameterized as functions of the jet η and p_T.

MC events are weighted by the probability to have at least one taggable jet and at least one b-tag, both according to the formula:

$$P_{tag/taggable} = 1 - \prod_{i=1}^{N}(1 - P_{i,tag/taggable}), \tag{4.12}$$

where N is the number of jets.

To the data events both taggability and b-tagging algorithms are applied directly.

4.1.8 τ Recontstruction

The tau lepton is the most massive, 1.78 GeV, third generation, charged lepton. It has a short lifetime, 2.9×10^{-13} s, corresponding to $c\tau = 87\mu$m, which is 4 times shorter than that of a b-quark. Because of this fact, and also the low track multiplicity of all τ decay modes, displaced vertex identification methods have had little success in τ-identification until now, and so the τ lepton is looked for, using specific features of its decay products.

TABLE 4.2

τ DECAY BRANCHING RATIOS [20].

Decay mode	Branching ratio (%)
Leptonic decays	
$\tau^- \to \mu^- \bar{\nu}_\mu \nu_\tau$	17.36 ± 0.05
$\tau^- \to e^- \bar{\nu}_e \nu_\tau$	17.84 ± 0.05
Type 1 Hadronic single-prong without π^0	
$\tau^- \to \pi^- \nu_\tau$	10.90 ± 0.07
Type 2 Hadronic single-prong with π^0	
$\tau^- \to \pi^- \pi^0 \nu_\tau$	25.50 ± 0.10
$\tau^- \to \pi^- 2\pi^0 \nu_\tau$	9.25 ± 0.12
$\tau^- \to \pi^- 3\pi^0 \nu_\tau$	1.04 ± 0.08
Type 3 Hadronic three-prong	
$\tau^- \to \pi^- \pi^+ \pi^- \nu_\tau$	9.33 ± 0.08
$\tau^- \to \pi^- \pi^+ \pi^- \pi^0 \nu_\tau$	4.59 ± 0.07

Tau lepton can decay into both electrons and muons, as well as hadronically. Tau leptonic decays are largely indistinguishable from the hadronic decay modes, and are included in this analysis with some restrictions. It should be mentioned that only τ pair production, as a decay mode of a Z boson, has been thoroughly studied at DØ [37, 39], although a successful τ+jets top quark cross-section measurement has also been made [40]. Studies of hadronic τ decays are assisted by having an extra recoil muon, or an electron, for that matter, see [30], which represents a leptonic decay of the other τ in the event.

Branching ratios of different τ decay modes are given in Table 4.2. Hadronic decay modes are studied separately in three types (only the leading modes are shown).

Hadronically decaying τ reconstruction begins similarly to jet reconstruction by identifying a calorimeter energy cluster by means of a simple cone algorithm, or

a modified algorithm, which starts combining calorimeter towers into a cluster, if it finds a charged particle track with $p_T > 5$ GeV, and the track position at a preshower detector is taken as the direction of the cluster axis starting from the primary vertex.

After identifying a calorimeter cluster, the number of tracks is determined within a $\Delta R < 0.5$ cone around the cluster axis with $p_T > 1.5$ GeV. According to the Table 4.2, taus with 1 track are considered separately from taus with more than 1 track. Tracks are added to the tau object if the second track has an invariant mass with the first one < 1.1 GeV, and a third one, if the tracks total invariant mass is < 1.7 GeV. The absolute value of the total charge of the tracks must not be greater than 2. Tau candidates with the absolute charge equal to 2 are retained in contrast to candidates that have absolute charge 0. Both correspond to tau candidates with a misreconstructed third track. Single track vertex positions are required to be within 2 cm in the z-direction.

At the second step, cell energies within the cones $\Delta R < 0.3, 0.5$ around the cluster axis are summed up and a set of tau identification variables is calculated.

At the third step, electromagnetic subclusters are identified using CellNN method, see Section 4.1.3, starting with calorimeter layer EM3. If no EM subclusters with the transverse energy $E_T > 0.8$ GeV in the EM3 layer are found, such τ candidate is classified as type 1; otherwise, if it has 1 track, it belongs to type 2.

Irrespective of the number of EM subclusters found, τ candidates with 2 or more tracks form a separate type, type 3.

One can see that according to this classification, type 1 tau candidate will have a smaller fraction of energy deposited into the electromagnetic layers of the calorimeter, as in Figure 4.14.

After the reconstruction stage, hadronic tau candidates still contain a lot of fakes,

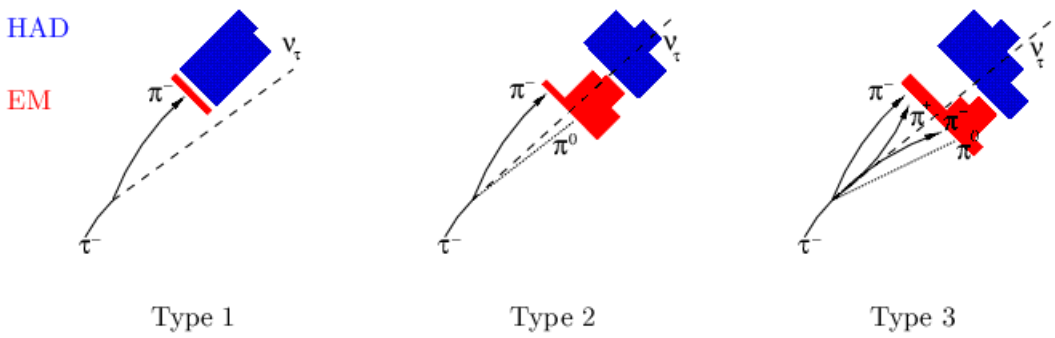

Figure 4.14. A schematic of the three types of taus. Adapted from [30].

mostly jets, but also muons and electrons. A further selection, which makes use of the tau identification variables calculated during the process of reconstruction, is necessary to suppress an enormous jet background plaguing any τ-lepton analysis.

A neural network algorithm was constructed to maximally employ the correlations between τ shower shape and tracking variables for the jet background rejection. A set of variables for each τ-type has been chosen to maximize a suitable signal significance ratio, $S/\sqrt{S+B}$, where S is $Z \rightarrow \tau^+\tau^-$ Monte Carlo sample with reconstucted τ candidates matched to the generated ones, and B is a data sample containing τ candidates, which are back-to-back in ϕ with a muon that has isolation cuts, see Section 4.4.1, reversed. The reversal of the isolation cuts gives a set of τ candidates that are mostly jets. The Monte Carlo sample was generated with a Z boson mass between 130 and 250 GeV, which is shifted from a normal range between 60 and 130 GeV, to accomodate a p_T^τ spectrum more resembling that of the data, see details in [52].

Each set of variables belongs to a subset of the following:

1. *EM12isof*, fraction of energy of the τ cluster in a cone $\Delta R < 0.5$, deposited into the layers 1 and 2 of the calorimeter,

$$EM12isof = \frac{E^{EM1} + E^{EM2}}{E^\tau}.$$

2. *trkiso*, sum of the p_T of the tracks not associated with the τ divided by the sum of the p_T of the tracks associated with a tau, both within a 0.5 cone,

$$trkiso = \frac{\sum p_T^{extratrk}}{\sum p_T^{\tau trk}}.$$

3. *fhf*, fraction of the energy of the τ cluster, deposited into the fine hadronic layers of the calorimeter.

4. *ET_o_sum*, ratio of τ cluster energy and the sum of the τ cluster energy and the p_T of the tracks, associated with the τ,

$$ET_o_sum = \frac{E_T^{\tau}}{E_T^{\tau} + \sum p_T^{\tau trk}}.$$

5. *dalpha*, a stereo angle between the vector sum of the momenta of the τ tracks and the direction of the τ electromagnetic subclusters, as seen from the primary vertex,

$$dalpha = \frac{\sqrt{(\frac{\Delta\phi}{\sin\theta})^2 + (\Delta\eta)^2}}{\pi},$$

calculated in the azimuthal angle and pseudorapidity coordinate basis. θ is the cluster polar angle with respect to the primary vertex.

6. *prf3*, energy of the leading electromagnetic subcluster, deposited into the calorimeter layer EM3, divided by the energy contained within the whole layer EM3 inside the τ 0.5 cone.

7. *profile*, transverse energy of the two most energetic calorimeter towers divided by the energy of the calorimeter cluster,

$$profile = \frac{E_{T_1} + E_{T_2}}{E_T^{\tau}}.$$

8. *emET_o_ET*, which is energy of the electromagnetic subclusters divided by the energy of the τ cluster,

$$emET_o_ET = \frac{E_T^{em}}{E_T^{\tau}}.$$

9. *ett1_o_ETiso*, the p_T of the leading τ track, divided by the energy of the tau cluster in a 0.5 cone,

$$ett1_o_ETiso = \frac{p_T^{leading\tau trk}}{E_T^{\tau iso}}.$$

10. *caliso*, a ratio of the energy in a hollow cone $0.3 < \Delta R < 0.5$ to the energy of the 0.5 cone tau cluster,

$$caliso = \frac{E_T^\tau - E_{Tcore}^\tau}{E_T^\tau}.$$

11. *rms*, transverse energy weighted stereo angle distance between individual cells in the calorimeter cluster and the cluster centroid,

$$rms = \sqrt{\frac{\sum_i^n ((\Delta\phi_i)^2 + (\Delta\eta_i)^2) E_{T_i}}{E_T^\tau}}.$$

12. *etad*/3, the absolute value of the position of the τ cluster in the calorimeter, divided by 3, to constrain the variable between 0 and 1,

$$etad/3 = \frac{|\eta^\tau|}{3}.$$

Table 4.3 lists the subsets of these variables found optimal during training of the τ neural network (NN_τ) for each τ type, and Figures 4.15, 4.16, 4.17, 4.18, show the variable distributions for the signal and background samples, used for training the NN_τ.

Some of the variables do not show significant discrimination power by themselves, like, for example *etad*/3. It was added to the set of NN_τinput variables to disentangle correlations among other variables for the tau candidates from different calorimeter regions.

4.1.9 Missing Transverse Energy

Taking a vector sum of the transverse energy of the reconstructed objects like jets, taus, electrons, photon, muons, unclustered energy from the calorimeter, we most likely will get a non-zero quantity. This may indicate several different things. First of all, real physical neutrinos do not interact with the detector parts at any substantial level, and thus contribute to the missing energy; and secondly, reconstructed objects may be poorly calibrated.

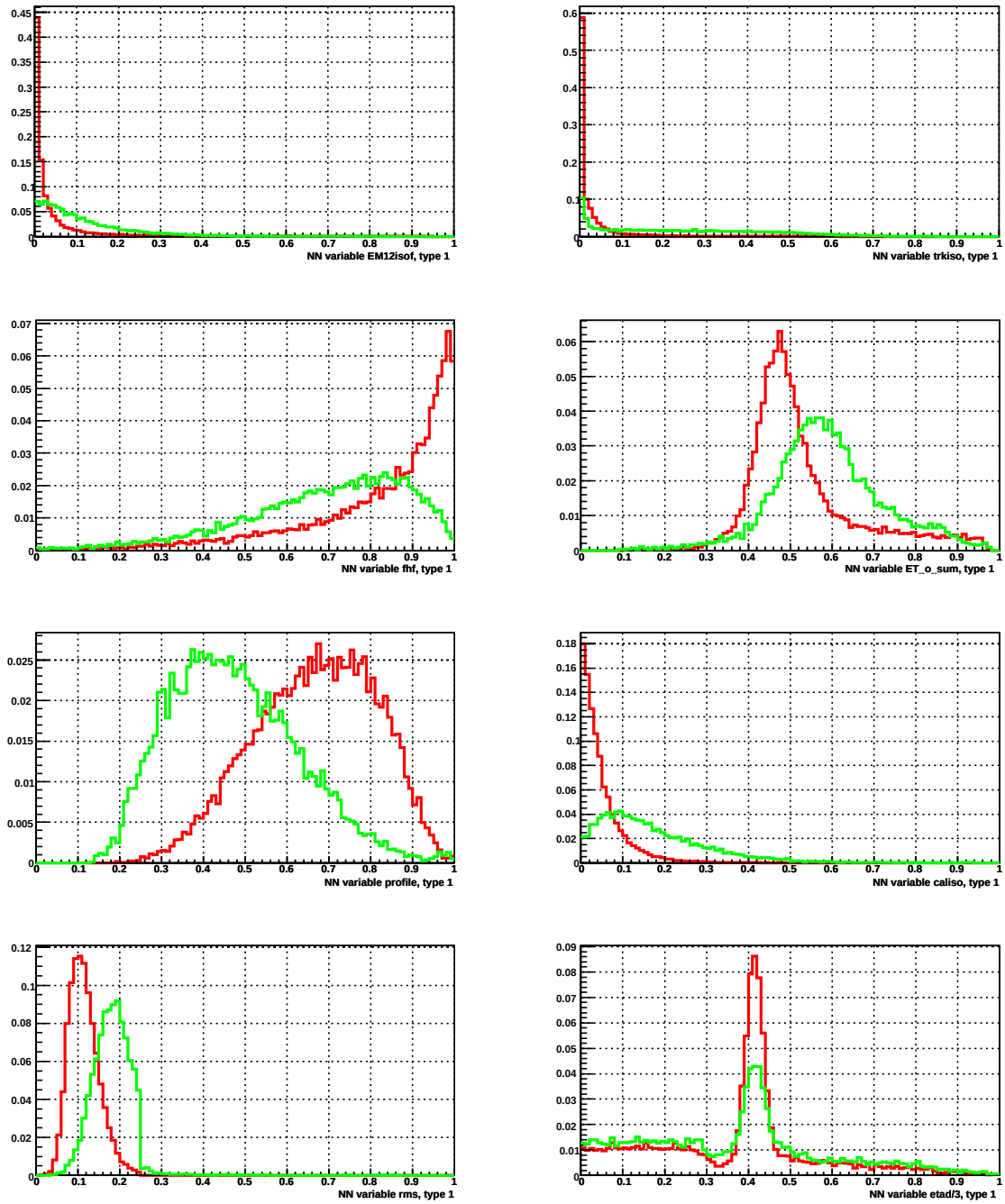

Figure 4.15. NN_τvariables for type 1. Red histograms are the $Z \rightarrow \tau^+\tau^-$ Monte Carlo, green are the anti-isolated muon data.

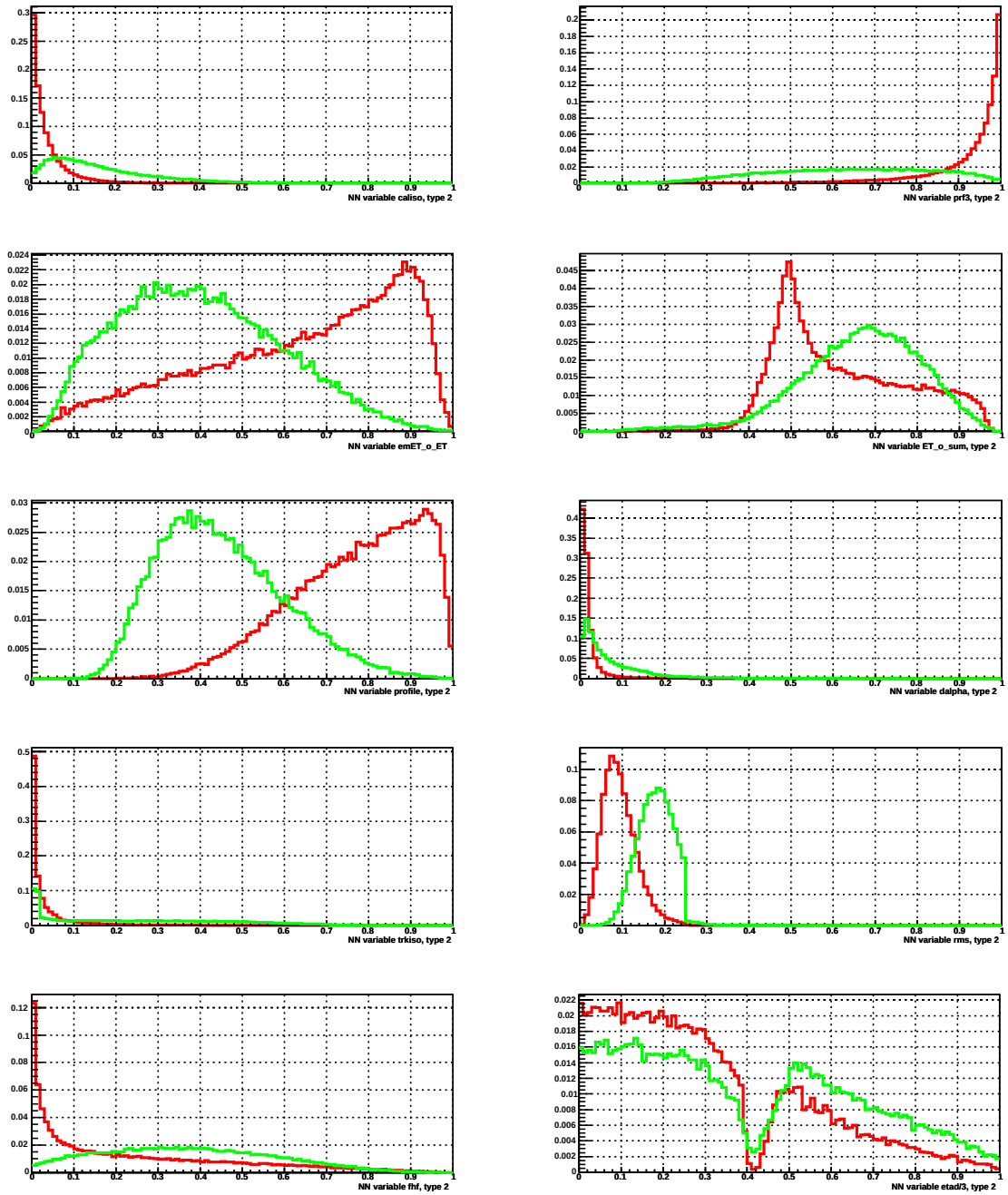

Figure 4.16. NN_τvariables for type 2. Red histograms are the $Z \rightarrow \tau^+\tau^-$ Monte Carlo, green are the anti-isolated muon data.

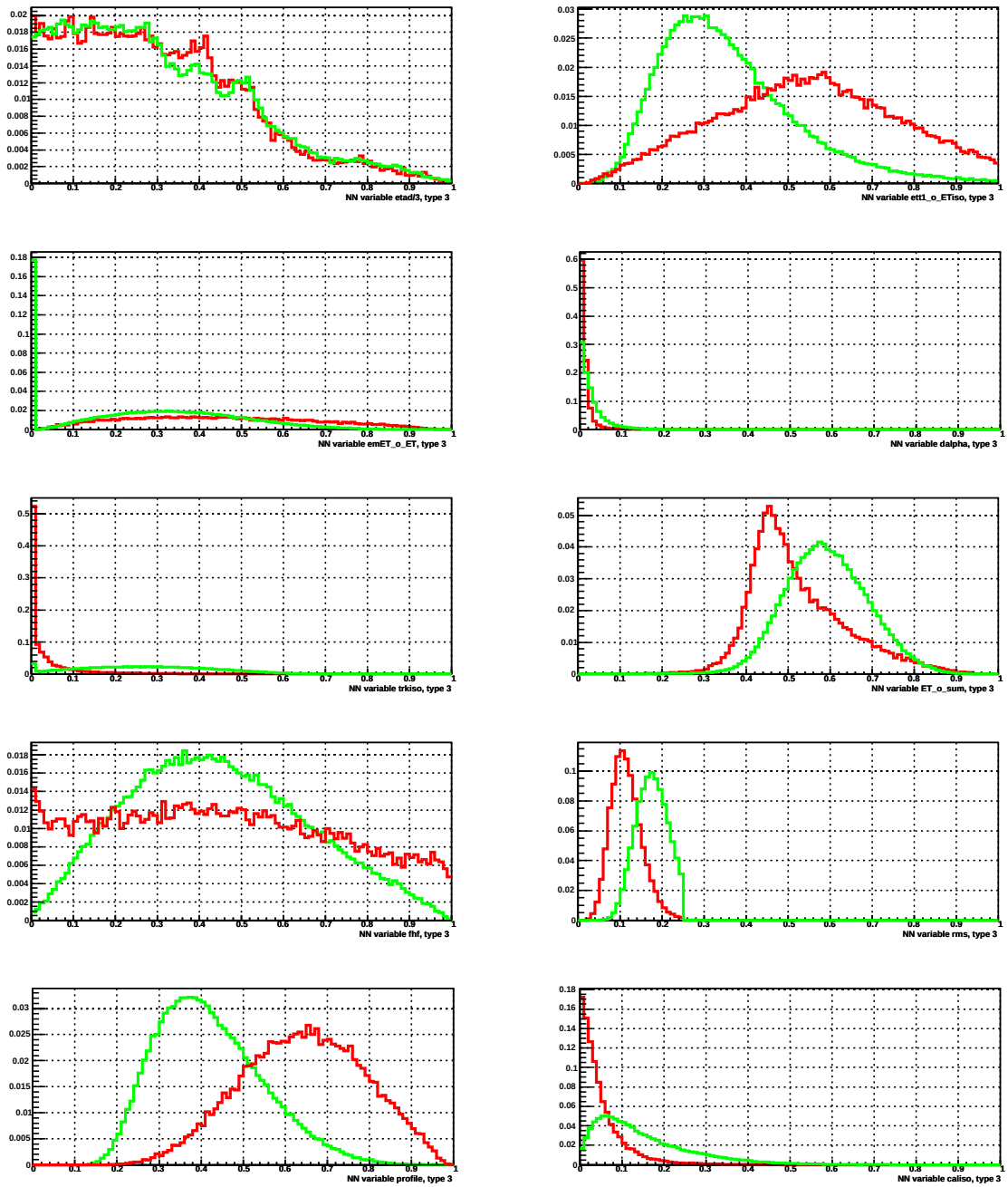

Figure 4.17. NN_τvariables for type 3. Red histograms are the $Z \rightarrow \tau^+\tau^-$ Monte Carlo, green are the anti-isolated muon data.

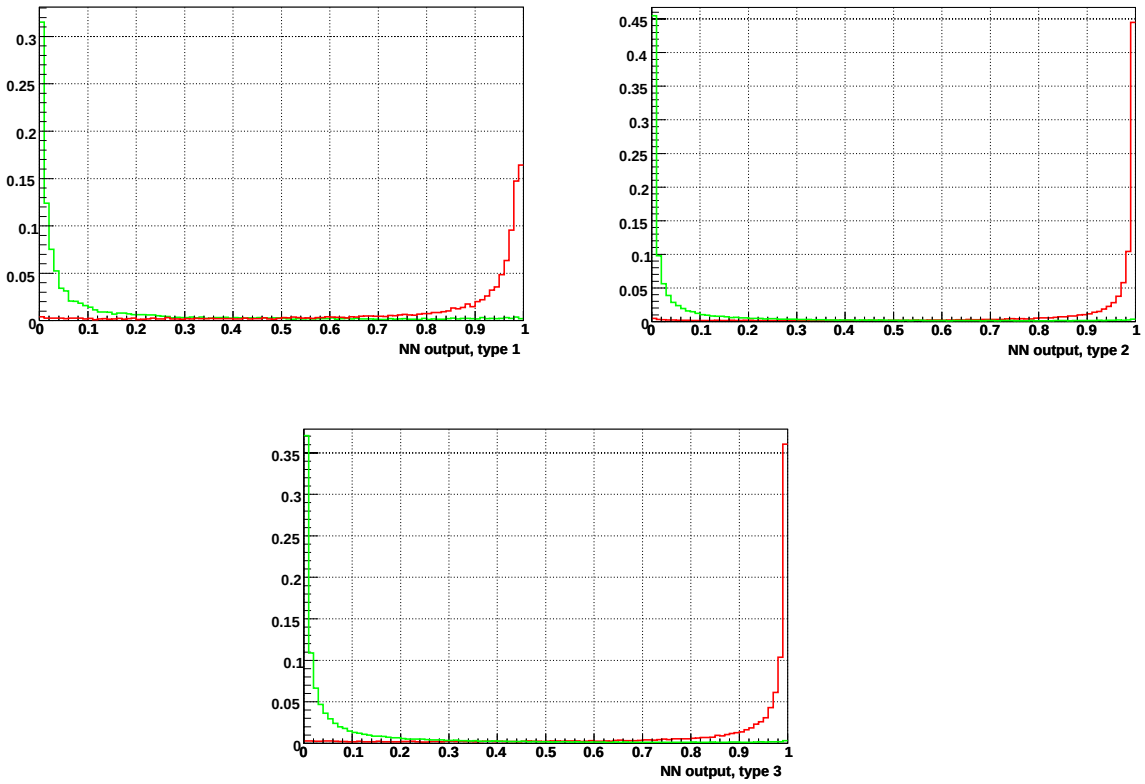

Figure 4.18. NN_τoutput for the three τ types. Red histograms are the $Z \rightarrow \tau^+\tau^-$ Monte Carlo, green are the anti-isolated muon data.

TABLE 4.3

NN_τINPUT VARIABLES USED FOR EACH τ TYPE.

Variable name	Type 1	Type 2	Type 3
$EM12isof$	✓		
$trkiso$	✓	✓	✓
fhf	✓	✓	✓
ET_o_sum	✓	✓	✓
$dalpha$		✓	✓
$prf3$		✓	
$profile$	✓	✓	✓
$emET_o_ET$		✓	✓
$ett1_o_ETiso$			✓
$caliso$	✓	✓	✓
rms	✓	✓	✓
$etad/3$	✓	✓	✓

Efforts are made by the DØ collaboration to keep the effects of the miscalibration of the energies of the calorimeter cells and reconstructed objects to a minimal level. Therefore, the energy of the missing neutrinos can be estimated by vectorially summing the energies of the calorimeter cells and correcting the sum by the energies of all the reconstructed objects.

In this analysis the invariant mass of the τ candidate, muon, and missing transverse energy ($\not\!\!E_T$) is used as a final limit setting variable.

4.2 Event Samples

Data and Monte Carlo event samples for this analysis were reconstructed using the software corresponding to the period of time after 2004, when a transition to a Common Analysis Format has been made at DØ. The reconstruction software also incorporated new calorimeter hadronic calibration algorithms, neural net b-tagging,

new luminosity constants, an improved jet energy scale algorithm, improved EM, muon, and τ identification algorithms.

4.2.1 Data Sample

This analysis was performed on the Run IIa data set collected at the DØ detector between April 2002 and February 2006 corresponding approximately to 1.1 fb^{-1} recorded luminosity. It used a $\sim$ 320 million event subset of these data, which required at least one muon in the event [42]. Data quality definitions from October 10, 2006 were applied rejecting around 15% of events. They include rejecting detector runs flagged as bad for SMT, CFT, calorimeter, and the muon detector. The total reconstructed luminosity for the selected triggers (described in Section 4.3) was 1064 ± 61 pb^{-1}. Events corresponding to calorimeter noise flags were also rejected.

4.2.2 Monte Carlo Samples

Signal Monte Carlo samples corresponding to the process $p\bar{p} \rightarrow bH \rightarrow b\tau^+\tau^-$ were generated using PYTHIA [43] generator with $p_T > 15$ GeV and $|\eta| < 2.5$ cuts on the contributing partons. The τ-leptons were decayed using the TAUOLA package [44]. The event samples were generated for different Higgs masses from 90-160 GeV separately, and their numbers of events after removing duplicates and bad data quality flags are given in Table 4.4.

To estimate $t\bar{t}$, WW, and WZ backgrounds PYTHIA generated inclusive samples were used, Table 4.4. W+jets, $Z \rightarrow ll + jets$ backgrounds were estimated both from data and Monte Carlo using samples generated with ALPGEN[45]. PYTHIA was used to model initial and final state radiation (FSR). Excessive heavy flavor production from PYTHIA FSR was removed by post processing the generated samples and leaving only heavy flavor particle jets corresponding to true generated heavy

TABLE 4.4

PYTHIA MC SIGNAL AND BACKGROUND SAMPLES.

Mass	Number of events	SM Cross section
$M_H = 90$ GeV	93733	10.31 fb
$M_H = 100$ GeV	110149	6.93 fb
$M_H = 110$ GeV	93454	4.75 fb
$M_H = 120$ GeV	96095	3.32 fb
$M_H = 130$ GeV	94813	2.35 fb
$M_H = 140$ GeV	94521	1.70 fb
$M_H = 150$ GeV	94195	1.24 fb
$M_H = 160$ GeV	93704	0.92 fb
$M_t = 175$ GeV	187048	7 pb
WW	182294	13.8 pb [48]
WZ	91854	4 pb

flavor quarks. These samples are described elsewhere [47]. The simulated events were processed through the DØ detector simulation and minimum bias events were added to all generated events at the digitization stage before being reconstructed with the same software as the collider data.

All samples were reweighted according to the difference between data and Monte Carlo instantaneous luminosity shapes and $Z \to ll + jets$ were reweighted according to the observed difference between p_T^Z in data and Monte Carlo [49].

4.3 Trigger

The analysis only considers events recorded with the list of single muon triggers in Table 4.5, from versions 8.10 to 14.93. A requirement that at least one selected muon, see Section 4.4.1, match trigger terms of at least one trigger from the list, was also imposed, and events that did not satisfy it, were removed.

Table 4.5 shows integrated luminosity recorded for the particular trigger periods and corresponding trigger names.

For example, trigger MUH1_ILM15 requires a L1Muon matched to a L1CTT track and a loose isolated muon object at L3, see Section 3.2.6.

The Monte Carlo events were weighted by the trigger probability weights, using the OR of the above triggers according to their relative luminosity. Existing prescale rates were included into the parametrization [50].

4.4 Object Identification and Selection

There are three types of physics objects used in this analysis: muons, hadronic taus, and jets. All selected objects are required to be associated with the same primary vertex within $\Delta Z_{vtx} < 1$ cm.

4.4.1 Muons

Following [46] and [51] the optimal muon selection was initially chosen to consist of the following requirements:

- LOOSE quality muon with $p_T > 12$ GeV matched to a central track
- Calorimeter isolation, energy within $0 < \Delta R < 0.5$, $I_{cal} < 2.5$ GeV, where $\Delta R = \sqrt{(\Delta\phi)^2 + (\Delta\eta)^2}$ is the distance in asimuth and pseudorapidity
- Track isolation: $I_{trk} = \sum_{\Delta R<0.5} p_T^{trks} < 2.5$ GeV, see Section 3.2.5
- If two or more isolated muons in the event, the muon with the highest p_T is selected
- Muon p_T was corrected relative to the beam spot, and muons having a central track $DCA > 0.02$ with at least 1 SMT hit, and $DCA > 0.2$ with no SMT hits were removed.

4.4.2 Hadronic Taus

We distinguish three τ final states, which we refer to as τ-types [51], see also Section 4.1.8:

TABLE 4.5

INTEGRATED LUMINOSITY RECORDED WITH DIFFERENT TRIGGER VERSIONS.

Triggers	Version	$\int \mathcal{L}dt$, (pb^{-1})	Reference
MU_W_L2M0_TRK3 MU_W_L2M0_TRK10 MU_W_L2M5_TRK10 MUW_W_L2M5_TRK10	8-10.3	53.2	MU_W_L2M5_TRK10
MUW_A_L2M3_TRK10	10.3-12	75.3	MUW_W_L2M3_TRK10
MU_W_L2M3_TRK10 MUW_W_L2M3_TRK10	12-13	231.9	MUW_W_L2M3_TRK10
MUH1_TK10 MUH1_TK12 MUH1_LM15 MUH1_TK12_TLM12 MUH2_LM15 MUH2_LM10_TK12 MUH2_LM3_TK12 MUH2_LM6_TK12 MUH3_LM15 MUH3_LM3_TK10 MUH3_LM6_TK12 MUH3_LM10_TK12 MUH4_LM15 MUH4_TK10 MUH5_LM15 MUH6_TK10 MUH6_LM15 MUH6_TK12_TLM12 MUH7_TK10 MUH7_TK12 MUH7_LM15	13.03-14.93 13-14 13.03-14.93 13.03-14.90 13.20-14.93 13.20-14.93 13.03-14.90	379.1	MUH1_TK12_TLM12
MUH1_ILM15	14-14.6	143.2	MUH1_TK12_TLM12
MUH1_ITLM10 MUH8_ILM15 MUH8_ITLM10 MUH8_TK12_TLM12	14.00-14.93 14.6-14.93	191.3	MUH1_TK12_TLM12

1. $\tau^{\pm} \rightarrow \pi^{\pm}\nu_{\tau}$: one track with the calorimeter cluster and no associated EM sub-cluster;
2. $\tau^{\pm} \rightarrow \rho^{\pm}\nu_{\tau} \rightarrow \pi^{\pm}\pi^{0}\nu_{\tau}$: one track with the calorimeter cluster and at least one associated EM sub-cluster (there can be more than one π^0 in the final state);
3. $\tau^{\pm} \rightarrow h^{\pm}h^{+}h^{-}(\pi^{0})\nu_{\tau}$: more than one track, with the calorimeter cluster, and with or without associated EM sub-clusters (h refers generically to a hadron)

An object reconstructed as a τ according to the above definitions is considered a τ-candidate if it satisfies the following requirements:

- $E_T^{\tau} > 12$ GeV for all τ-types, where E_T^{τ} is the E_T of the calorimeter cluster associated with the τ-candidate (τ-cluster);
- $p_T^{\tau_{trk}} > 7$ GeV for type 1 and $p_T^{\tau_{trk}} > 5$ for the highest p_T track for type 3 τ-candidates; $p_T^{\tau_{trk}} > 5$ GeV for type 2 and $\sum p_T^{\tau_{trk}} > 7$ GeV for type 3 τ-candidates, where $\sum p_T^{\tau_{trk}}$ is the sum of the p_T's of all the tracks associated with the τ-candidate
- $\tau_{rms} < 0.25$, with τ_{rms} defined as $\sqrt{\eta_{rms}^2 + \phi_{rms}^2}$, where $\eta_{rms} = \sum E_T^{tower} \cdot (\eta^{\tau} - \eta^{tower})/E_T^{\tau}$, and similarly for ϕ_{rms} [51].
- $\Delta\phi(\mu, \tau) > 2$
- if there is a second $LOOSE$, track matched muon, matched to a τ candidate, the τ candidate is rejected.

After the above selection, the τ-candidates are passed through a τ-identification Neural Network (NN_{τ}) [52]. The NN_{τ} has been trained separately for each τ-type, and for type 1 separately for ICD region and outside of it.

The cuts on NN_{τ} are optimized separately for each τ type in the data. The reference values for the following cross-check plots are:

- for type 1 τ's: $NN_{\tau} > 0.9$
- for type 2 τ's: $NN_{\tau} > 0.9$
- for type 3 τ's: $NN_{\tau} > 0.95$

In the following sections these are referred to as the minimum NN_{τ} requirement for each τ type, $minNN_{\tau}$.

4.4.3 Jets

A candidate event is required to have one or more jets satisfying the Run IIa *good jet* quality criteria [53], with $p_T > 15$ GeV, and det $|\eta| < 2.5$. Jets matching electrons objects, described in Section 4.1.4, with a likelihood > 0.85, the candidate muon and the candidate τ within $\Delta R < 0.5$ were removed. The resulting jets are called the "isolated jets" below.

4.4.4 B-tagging

For b-jet identification, the NN tagger [35] was used in this analysis. The Monte Carlo events were weighted by the probability to have at least one isolated taggable jet and at least one b-tag, derived from the jet taggability [54] and b-tagging efficiencies available after running the corresponding b-tagging algorithms. A reference b-tagging working point for the cross-check plots below is NN_TIGHT, see Section 4.1.7.

4.4.5 Preselection

All samples have been initially reduced to a smaller size by identifying a $\tau + \mu$ candidate pair, by applying the following cuts: $p_T^{\tau} > 10, 5, 10$ GeV, $p_T^{\tau trk} > 7, 5, 5$ GeV for τ types 1, 2, 3, respectively, and also $\sum p_T^{\tau trk} > 7$ for the type 3, $p_T^{\mu} > 8$ GeV, DCA cuts from the Section 4.4.1, and a cut of $NN_{\tau} > 0.2$. In addition, type 1, 2 τ tracks were required to have at least one SMT hit.

This set of cuts is referred to as the preselection cuts below.

The set of cuts, described in the Secs. 4.4.1, 4.4.2, 4.4.3, 4.4.4, is the reference set of cuts.

4.5 Backgrounds

There are three major backgrounds for the $bH \rightarrow b\mu\tau$ process. These are QCD multijet production, $Z + (b)jets \rightarrow \mu\tau + (b)jets$, and $t\bar{t} \rightarrow b\bar{b}\mu\tau$.

Backgrounds originating from $W + 2(bc)jets \rightarrow \mu + 2(bc)jets$ and WW production are heavily suppressed by the τ-ID and b-tagging, and their contributions are estimated from Monte Carlo.

Backgrounds containing a Z boson like $Z + jets$ or WZ and ZZ are estimated from data for the final selection and also cross checked from Monte Carlo. We propose two normalization schemes, one from data and one from Monte Carlo, and discuss their applicability, see Sec. 5.1.

4.5.1 W+jets estimation

$W + jets$ samples are normalized to the leading order (LO) ALPGEN cross section, not mentioning the fact, that after the luminosity reweighting and heavy flavor (HF) processing, see Section 4.2.2 the overall normalization needs to be restored. Also, on top of the theoretical next-to-leading-order (NLO) scale factors, called K-factors, that should be applied to the leading order $W + jets$ MC, so it can better match the data, heavy flavor to light flavor (LF) ratio needs to be corrected, and we apply a scale factor of 1.17 ± 0.18 to the $W + 2b(c) + ljets$ (HF) samples [55] relative to LF. By the following procedure LF K-factors are absorbed into the renormalization.

By applying the cuts $p_T^{\mu} > 25$ GeV, $\not{E}_T > 20$ GeV, $M(\mu, \tau_{trk}) < 70$ GeV (which is the invariant mass of the muon and the τ track, this cut is applied to reduce the $Z \rightarrow \mu^+\mu^-$ contribution), $0.2 < NN_\tau < 0.9$ we get a relatively pure sample of $W + jets$. We normalize the jet multiplicity distribution in MC, which is dominated by $W + jets$, to data in each jet multiplicity bin, assuming the discrepancy is

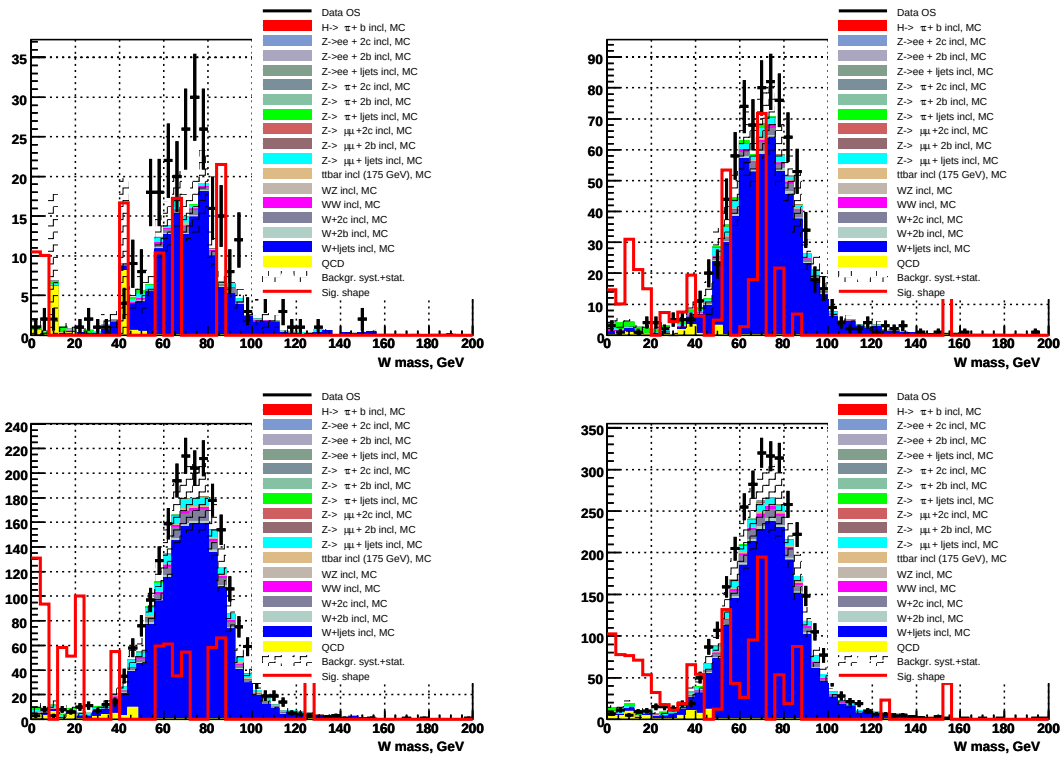

Figure 4.19. μ-$\not{E}_T$transverse mass (Wmass) for the three τ-types (top left - type 1, top right - type 2, bottom left - type 3, and bottom right - all types) before the normalization.

due entirely to the $W + jets$ contribution, to obtain both an overall and partial agreement in jet multiplicity which we believe the MC does not accurately reproduce. Figures 4.19 and 4.20 show the muon and $\not{E}_T$ transverse mass (Wmass) $Wmass = \sqrt{2 \cdot p_T^{\mu} \cdot \not{E}_T \cdot \cos(\Delta\phi(\mu, \not{E}_T))}$ before the normalization and Figures 4.21 and 4.22 after it. Jet multiplicity should be understood as the number of jets isolated from both μ and τ, satisfying the jet quality cuts, Section 4.4.3.

The coefficients applied to each jet multiplicity bin are summarized in table 4.6. Errors on the coefficients are statistical.

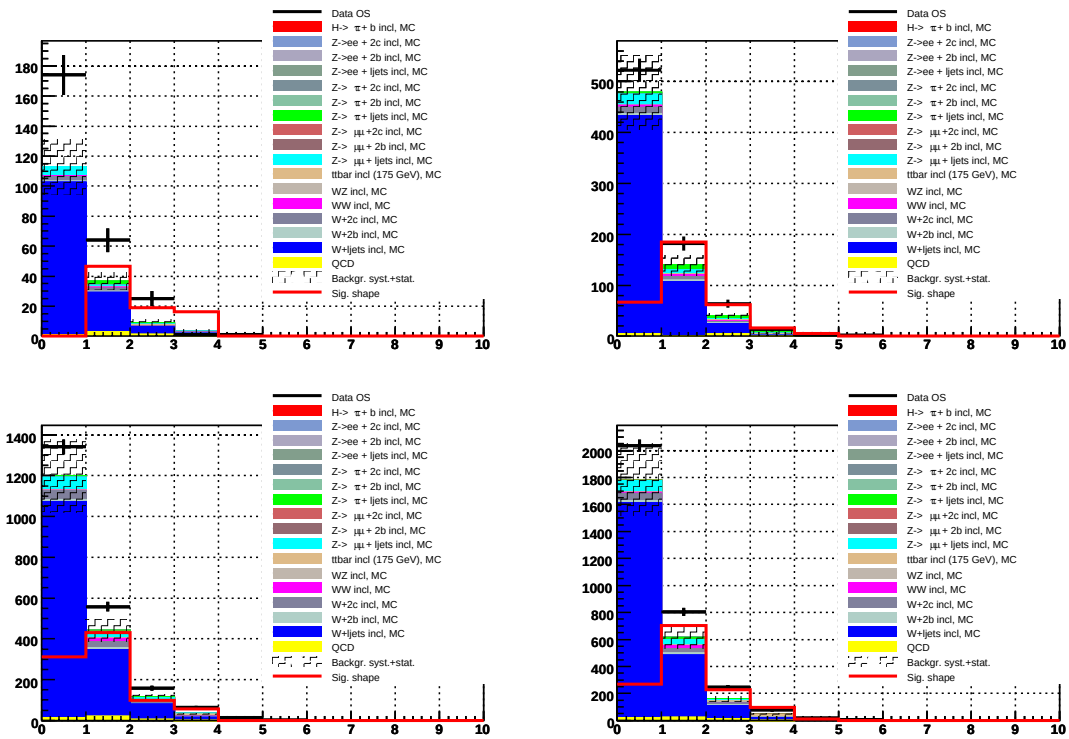

Figure 4.20. Jet multiplicity for the three τ-types (top left - type 1, top right - type 2, bottom left - type 3, and bottom right - all types) before the normalization.

TABLE 4.6

$W + jets$ JET MULTIPLICITY SCALE FACTORS. QUOTED UNCERTAINTIES ARE STATISTICAL.

	Type 1	Type 2	Type 3
0 jets	1.58 ± 0.19	1.09 ± 0.08	1.12 ± 0.05
1 jet	1.93 ± 0.38	1.36 ± 0.14	1.31 ± 0.09
2 jets	3.89 ± 1.10	2.05 ± 0.36	1.51 ± 0.19

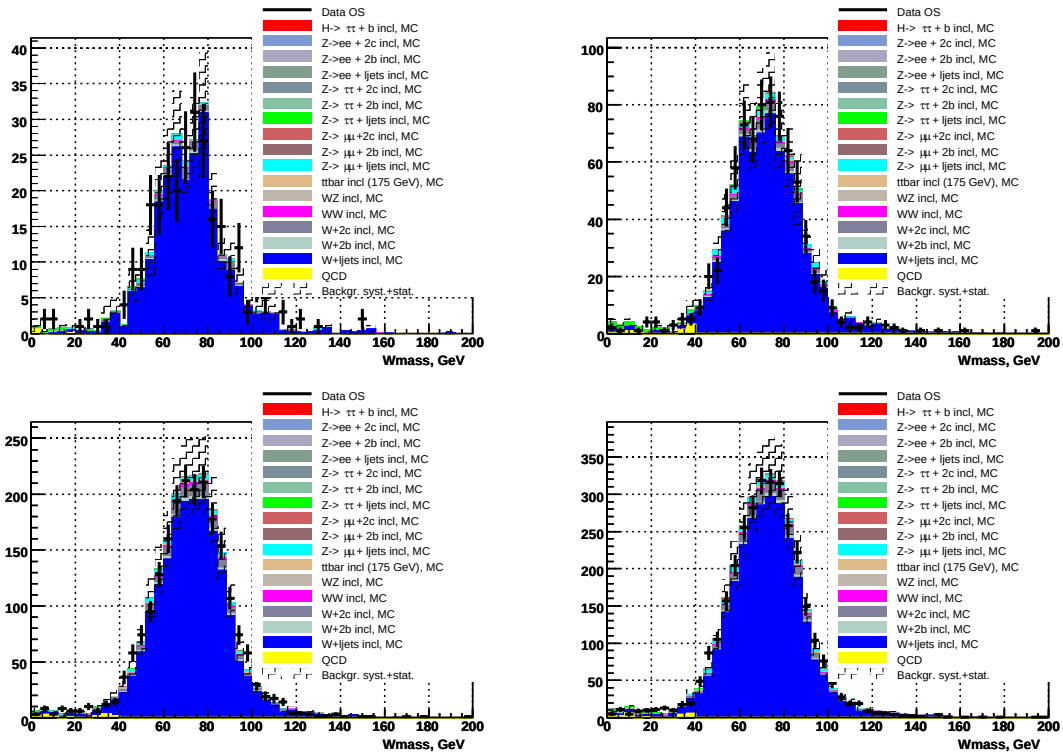

Figure 4.21. μ-$\not{E}_T$transverse mass (Wmass) for the three τ-types (top left - type 1, top right - type 2, bottom left - type 3, and bottom right - all types) after the normalization.

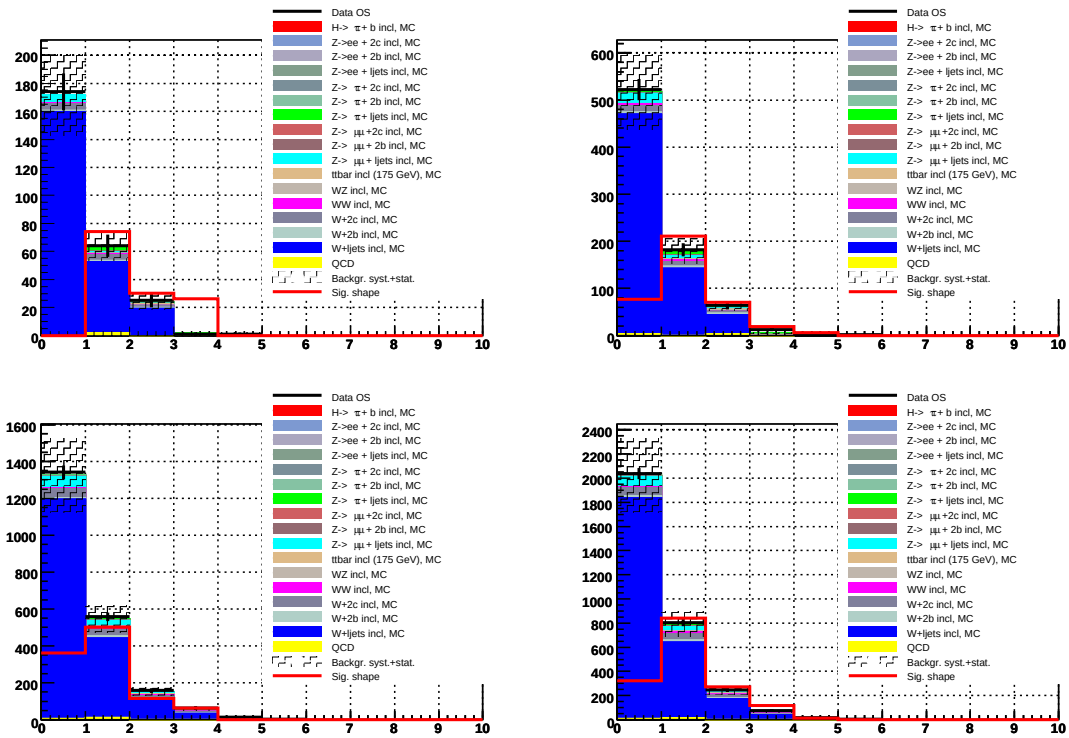

Figure 4.22. Jet multiplicity for the three τ-types (top left - type 1, top right - type 2, bottom left - type 3, and bottom right - all types) after the normalization.

4.5.2 $Z + jets \rightarrow \mu^+\mu^- + jets$ estimation from Monte Carlo

Another factor contributing to the distortion of the jet multiplicity in $Z + jets$ MC is reweighting of the Z boson transverse momentum p_T^Z, which affects the normalization of the individual $Z + jets$ samples because it depends on the jet multiplicity.

We use the same technique to find the normalization for the $Z+jets \rightarrow \mu\mu+jets$ background. The sample is prepared by requiring an isolated muon, Sec. 4.4.1 with $p_T^\mu > 25$, $\sum p_T^{\tau trk} > 25$ GeV, $E_T^\tau < 18$ GeV on top of the preselection. Figures 4.23 and 4.25 illustrate the change in the Z mass peak (invariant mass of the muon and the vector sum of the τ tracks) after the renormalization. Figure 4.24 shows the jet multiplicity before and Figure 4.26 after the renormalization. The discrepancy between data and MC here is equally divided between all contributing $Z + jets$ samples, where a HF/LF scale factor of 1.33 is applied to the HF samples, see [56]. QCD background is negligible. $Z + jets \rightarrow ee + jets$ is small and is not rescaled separately.

Jet multiplicity scale factors are shown in Table 4.7 for each τ type individually. Statistical errors on these coefficients are larger than a possible difference between these scale factors and those measured for the $Z + jets \rightarrow \tau\tau + jets$ background, in the sample where it dominates, therefore we believe that applying them to the $Z + jets \rightarrow \tau\tau + jets$ background in this particular calculation is legitimate.

4.5.3 QCD estimation

A QCD event with three or more jets can have an isolated muon from a misreconstructed jet, (the muon can also pass the isolation cuts, if it has high enough momentum relative to the jet axis), a fake τ, and a real or fake b-jet. Since the sign of such muon has a low degree of correlation with the sign of a fake τ_h, the QCD

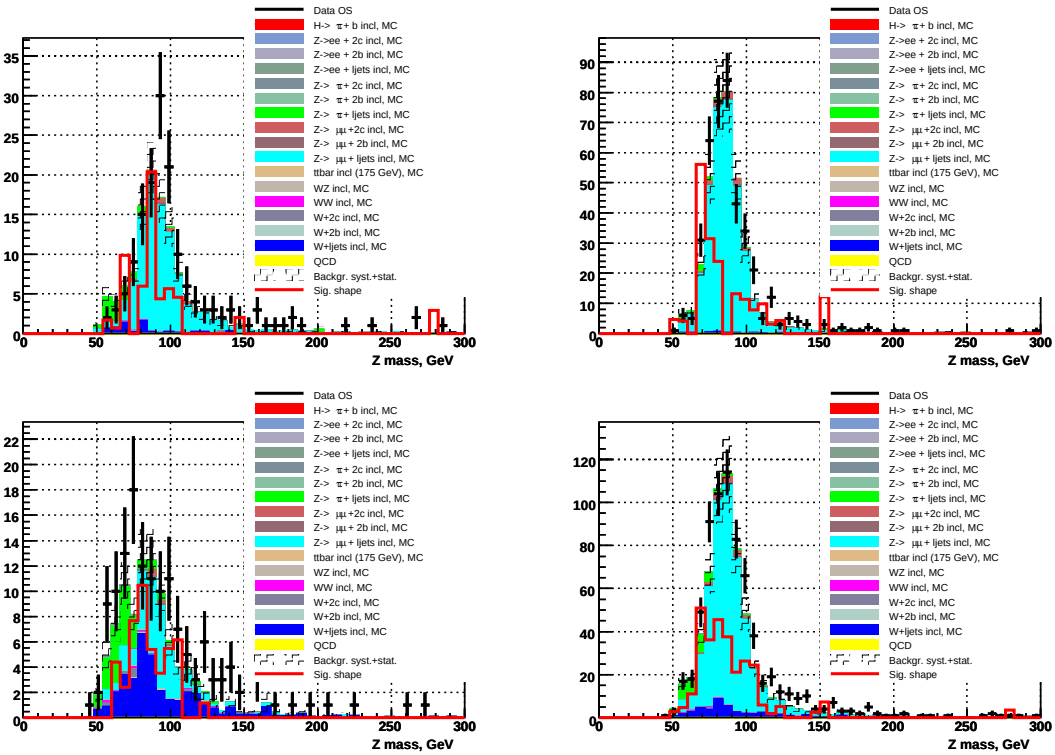

Figure 4.23. μ, $\sum \tau_{pT}^{trk}$ invariant mass (Zmass) for the three τ-types (top left - type 1, top right - type 2, bottom left - type 3, and bottom right - all types) before the normalization.

TABLE 4.7

$Z + jets \rightarrow \mu\mu + jets$ JET MULTIPLICITY SCALE FACTORS. QUOTED UNCERTAINTIES ARE STATISTICAL.

	Type 1	Type 2	Type 3
0 jets	1.32 ± 0.15	1.15 ± 0.09	1.91 ± 0.19
1 jet	1.61 ± 0.45	1.06 ± 0.20	1.54 ± 0.45
2 jets	0.86 ± 0.56	0.98 ± 0.42	2.33 ± 1.35

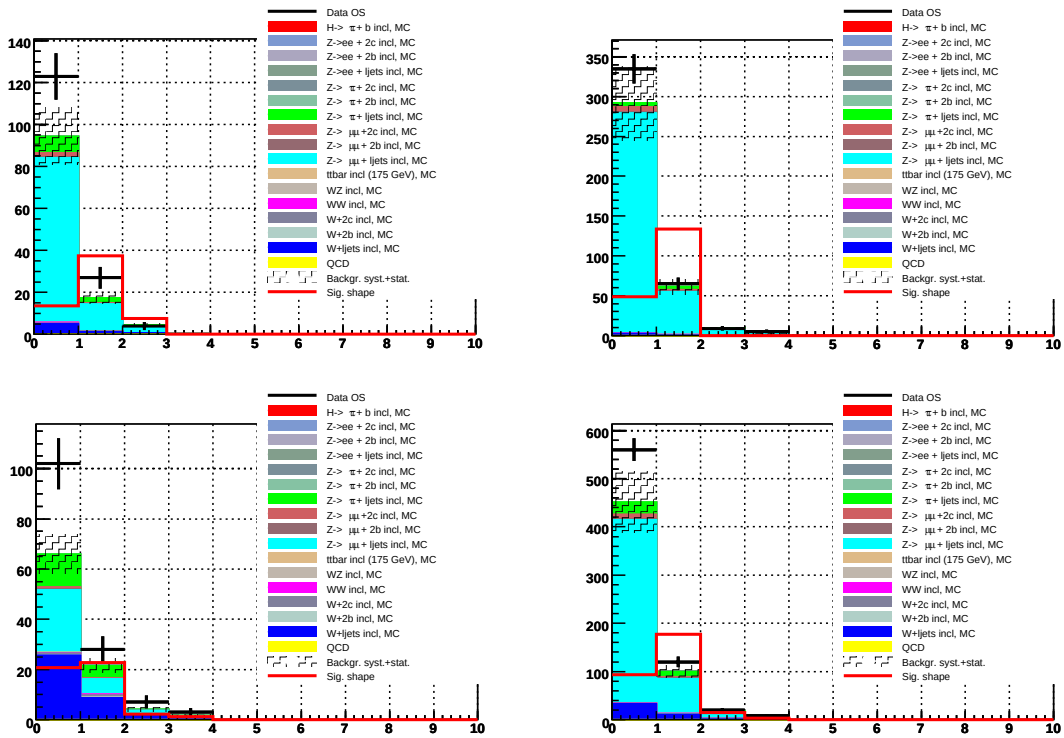

Figure 4.24. Jet multiplicity for the three τ-types (top left - type 1, top right - type 2, bottom left - type 3, and bottom right - all types) before the normalization.

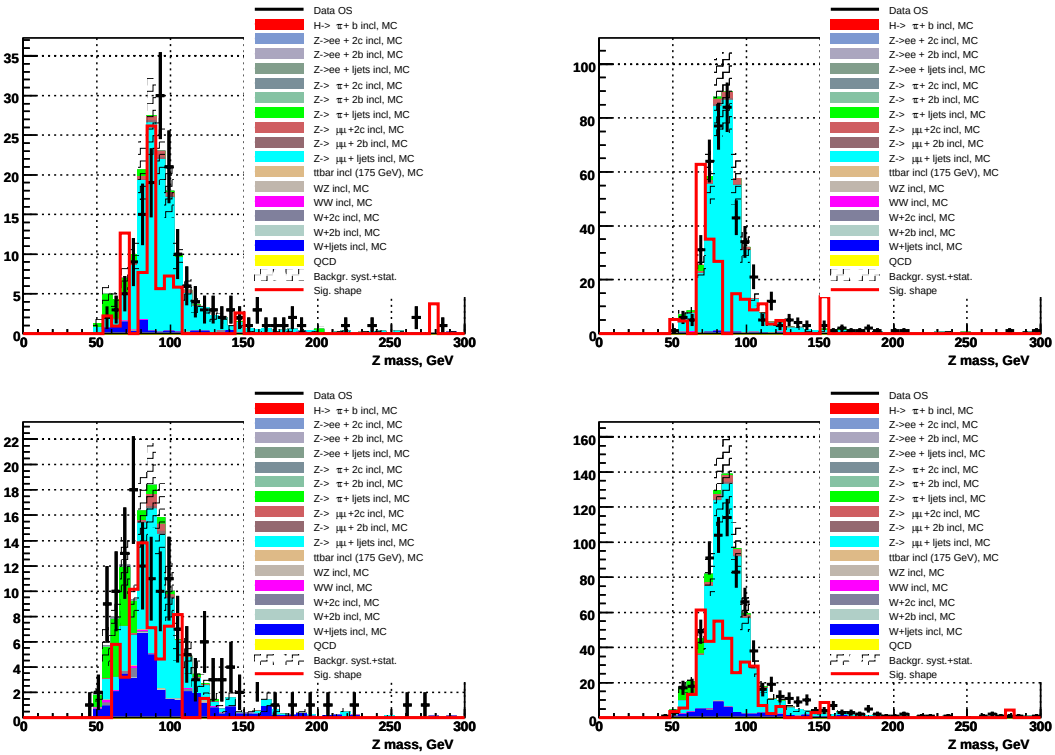

Figure 4.25. μ, $\sum \tau_{pT}^{trk}$ invariant mass (Zmass) for the three τ-types (top left - type 1, top right - type 2, bottom left - type 3, and bottom right - all types) after the normalization.

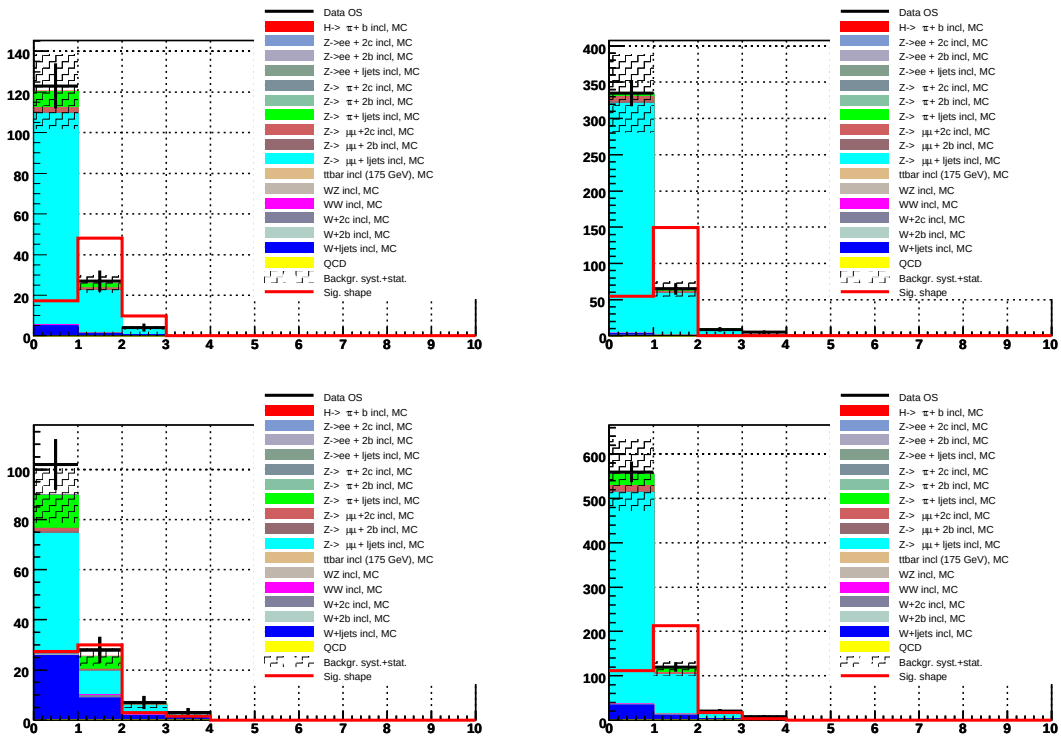

Figure 4.26. Jet multiplicity for the three τ-types (top left - type 1, top right - type 2, bottom left - type 3, and bottom right - all types) after the normalization.

background tends to have equal amounts of opposite sign (OS) and same sign (SS) $\mu - \tau$ candidate events. In contrast, the signal should contain only opposite sign $\tau^+\tau^-$ events coming from the Higgs Decay.

To estimate the number of QCD events out of the total number of SS events, we first measure the *QCD fake rate* in a sample, in which the selected muon fails the isolation criteria (the parameter space is schematically illustrated in the Figure 4.27):

$$QCD\ fake\ rate = \left(\frac{N_{SS,NN_\tau > minNN_\tau}}{N_{SS,NN_\tau > 0.4}}\right)_{non\text{-}isolated\ \mu}. \tag{4.13}$$

We can then estimate the amount of the QCD background in the data sample, by multiplying the number of SS events, with an isolated muon, before the NN_τ cut, corrected for the non-QCD backgrounds (taken from MC), by the QCD fake rate:

$$N_{QCD,SS} = (N_{data} - N_{MC})_{SS,NN_\tau > 0.4, isolated\ \mu} \cdot (QCD\ fake\ rate). \tag{4.14}$$

In the above, we have assumed that the QCD background contains precisely equal amounts of OS and SS events. In order to test this assumption, we create a sample with a non-isolated muon and a fake τ-candidate. Fake tau is defined as a τ-candidate with $0.4 < NN_\tau < minNN_\tau$. The NN_τdistribution with the muon isolation cuts applied is illustrated in Figure 4.28, and one of the isolation parameters, track isolation, see Section 4.4.1, is shown in Figure 4.29 with $minNN_\tau$ cuts applied and no muon isolation cuts. Both are shown for a set of cuts with a requirement of at least one extra jet isolated from both μ and τ-candidate.

QCD in Figure 4.28 is just the same sign events, and in the Figure 4.29 it is SS events multiplied by the QCD fake rate as described above. The OS and SS distributions have indeed similar shapes, but the total amount of OS events

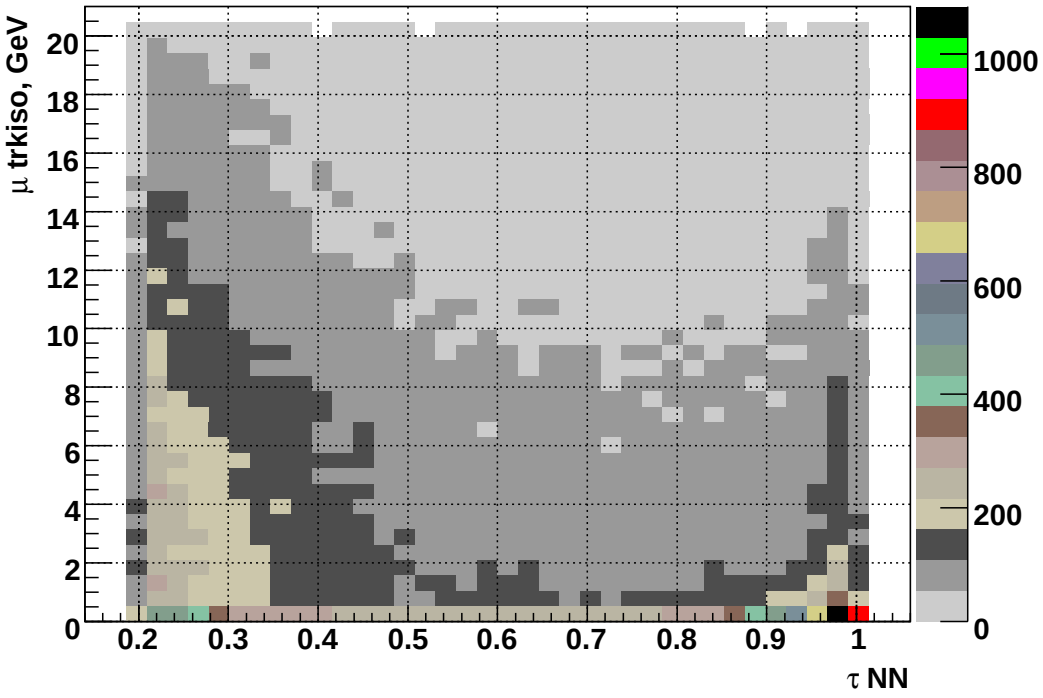

Figure 4.27. μ track isolation vs. $NN_\tau$for the SS events in data.

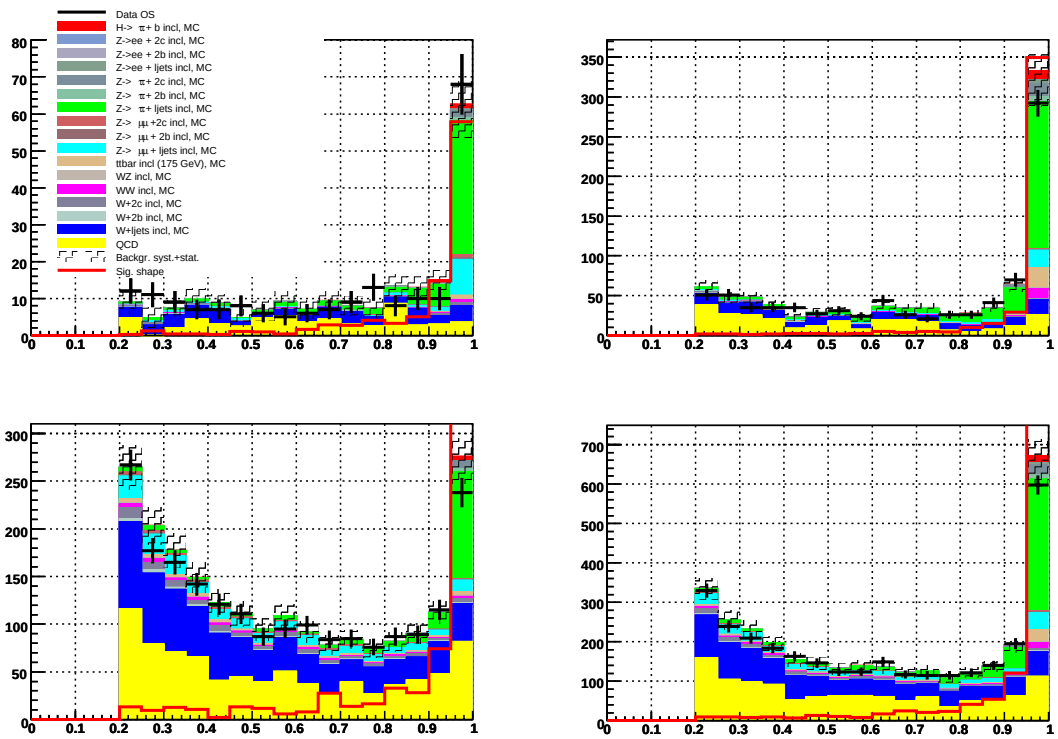

Figure 4.28. NN_τdistributions with muon isolation applied and an isolated jet required, for the three τ-types (top left - type 1, top right - type 2, bottom left - type 3, and bottom right - all types). QCD is represented by SS events.

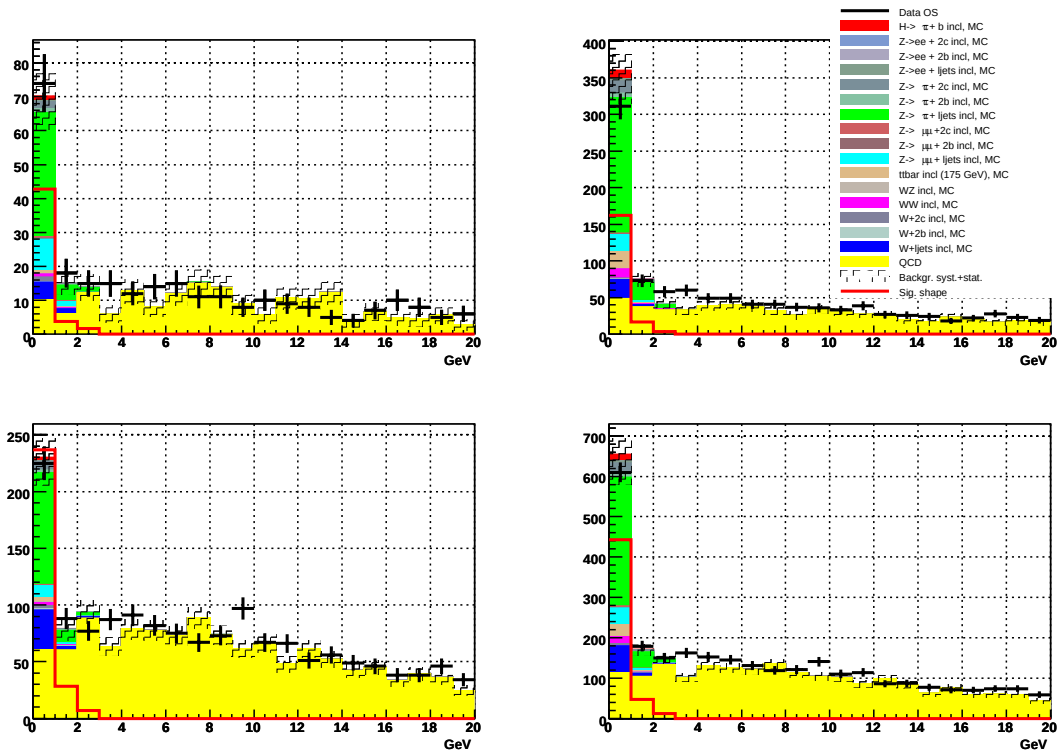

Figure 4.29. Muon track isolation distributions with $minNN_\tau$ cuts applied and an isolated jet required, for the three τ-types (top left - type 1, top right - type 2, bottom left - type 3, and bottom right - all types). QCD is represented by SS events corrected for the τ fake rate.

exceeds the amount of SS events, after subtraction of the backgrounds calculated from Monte Carlo, by 4-9%, depending on the τ_h type (see Table 4.8). Therefore, when estimating the QCD background in the data using Eq. 4.14, we correct the number of SS events by the above factor:

$$N_{QCD,OS} = N_{QCD,SS} \cdot \left(\frac{OS}{SS}\right)_{non\text{-}isolated\ \mu, fake\ \tau} . \tag{4.15}$$

Finally, the estimated number of QCD multijet OS events is multiplied by the b-tagging rate measured in the QCD sample. The b-tagging rate is defined as the fraction of events with at least one taggable jet that have at least one b-tagged jet, see Section 4.1.7. The measured b-tagging rates in the QCD sample for the three τ types for NN_TIGHT b-tagger are given in Table 4.8. Figure 4.30 shows muon track isolation where QCD means SS events from the isolated muon region with all three corrections applied.

TABLE 4.8

OS VS SS ASYMMETRY AND B-TAGGING RATE IN THE QCD DATA SAMPLE. QUOTED UNCERTAINTIES ARE STATISTICAL AS PER BIN IN FIGURE 4.29.

	Type 1	Type 2	Type 3
QCD OS/SS ratio	1.07±0.14	1.09±0.07	1.04±0.03
QCD b-tag rate (%)	8.1±0.2	7.9±0.1	8.0±0.1

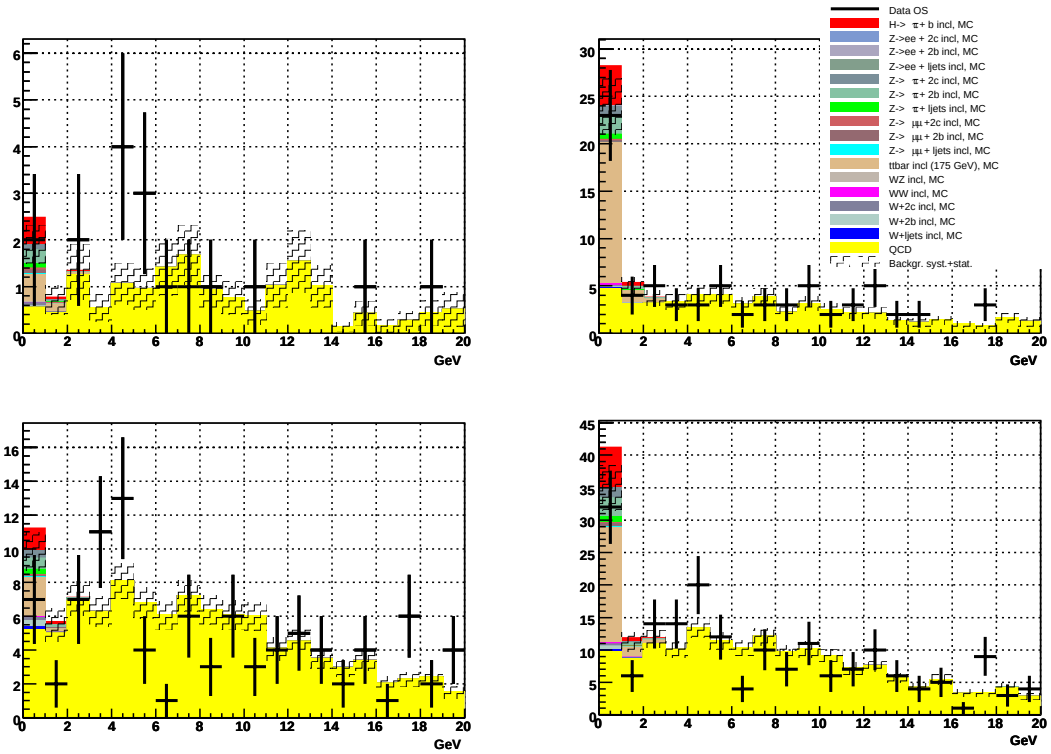

Figure 4.30. Muon track isolation distributions with $minNN_\tau$ cuts applied and a NN_TIGHT b-tag required, for the three τ-types (top left - type 1, top right - type 2, bottom left - type 3, and bottom right - all types). QCD is represented by SS events corrected by all three rates. Signal with Higgs mass 150 GeV is shown in red.

4.5.4 $Z + jets \rightarrow \tau^+\tau^- + jets$ estimation from Monte Carlo

After normalizing $W + jets$, $Z + jets \rightarrow \mu^+\mu^- + jets$ one can think of removing the existing discrepancy between data and Monte Carlo through renormalization of the remaining significant background, $Z + jets \rightarrow \tau^+\tau^- + jets$, as in Figs. 4.31, 4.32. We use the same procedure as for the $Z + jets \rightarrow \mu^+\mu^- + jets$.

The coefficients applied to each jet multiplicity bin are summarized in Table 4.9. Errors on the coefficients are statistical. Figures 4.33, 4.34 show the normalized distributions.

TABLE 4.9

$Z + jets \rightarrow \tau^+\tau^- + jets$ JET MULTIPLICITY SCALE FACTORS. QUOTED UNCERTAINTIES ARE STATISTICAL.

	Type 1	Type 2	Type 3
0 jets	1.97 ± 0.12	1.57 ± 0.05	2.57 ± 0.10
1 jet	1.37 ± 0.19	1.14 ± 0.09	1.49 ± 0.12
2 jets	1.03 ± 0.32	1.60 ± 0.21	1.64 ± 0.30

A different cross check is necessary to validate the application of the trigger probabilities to the Higgs signal Monte Carlo above the $p_T^\mu > 12$ GeV muon p_T cut. This is done by simulating the $Z + jets \rightarrow \tau^+\tau^- + jets$ background with PYTHIA, which is the generator used for modelling the signal. Muon p_T distribution is shown in the Figure 4.35 with a normalization only to an overall cross section of 247 pb, as in [38].

We can see that the normalization to the trigger probabilities from Section 4.3 and $Z \rightarrow \tau^+\tau^-$ cross section leads to a sufficient agreement between the data and sum of the backgrounds within the systematic errors, see Section 4.7.

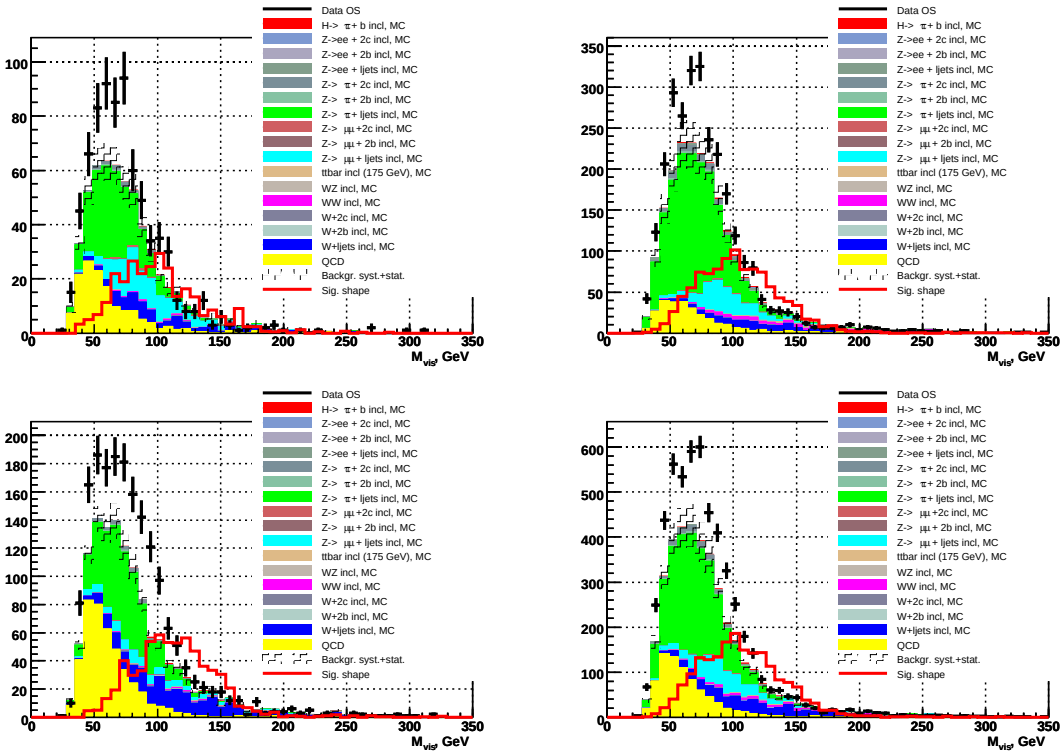

Figure 4.31. Muon, τ and $\not{E}_T$ invariant mass (visible mass) with reference final selection cuts, Sec. 4.4, without requiring an extra isolated jet for the three τ-types (top left - type 1, top right - type 2, bottom left - type 3, and bottom right - all types) before the normalization.

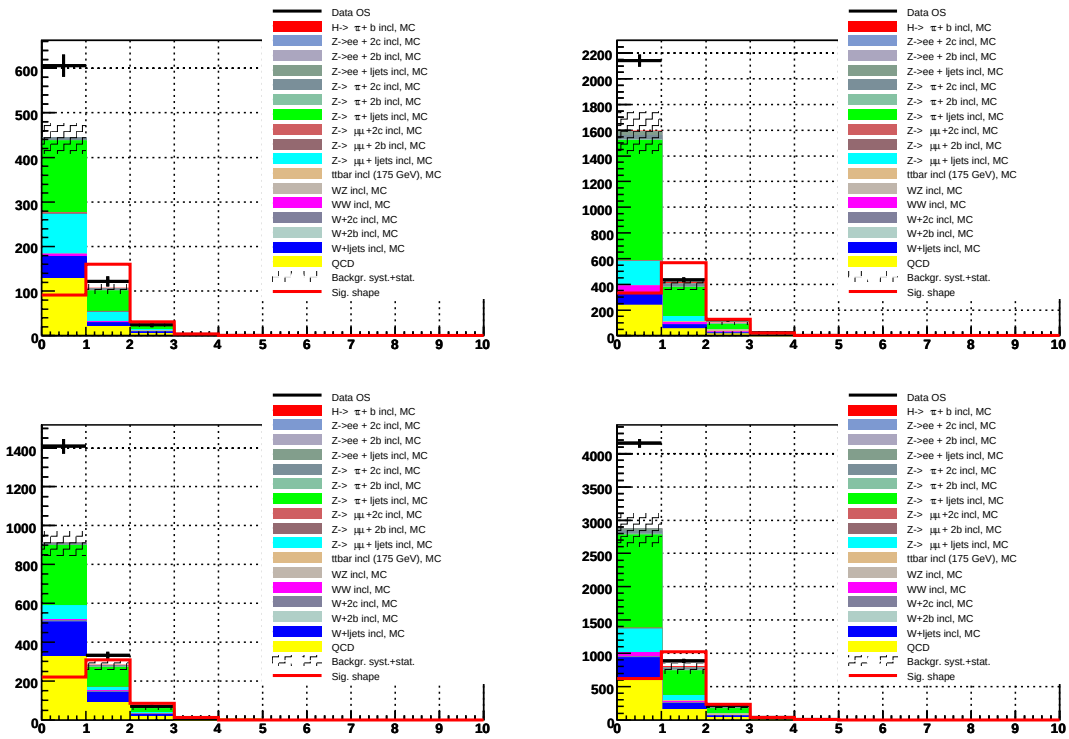

Figure 4.32. Isolated jet multiplicity with reference final selection cuts, Sec. 4.4, for the three τ-types (top left - type 1, top right - type 2, bottom left - type 3, and bottom right - all types) before the normalization.

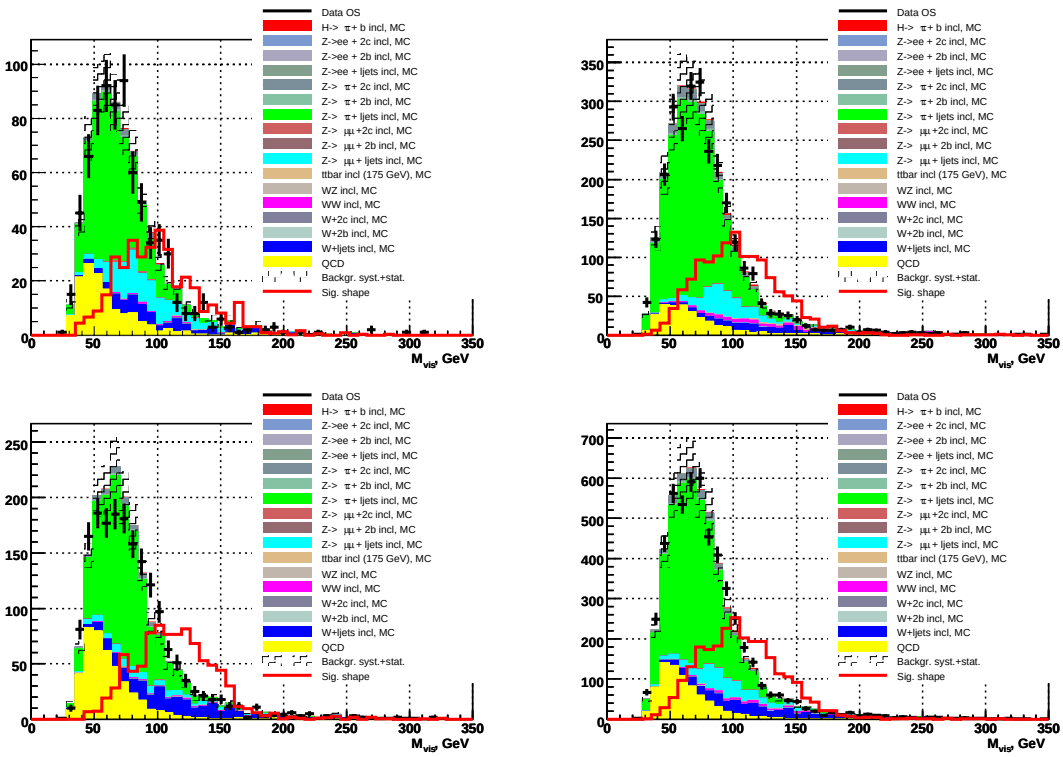

Figure 4.33. Muon, τ and $\not{E}_T$ invariant mass (visible mass) with reference final selection cuts, Sec. 4.4, without requiring an extra isolated jet for the three τ-types (top left - type 1, top right - type 2, bottom left - type 3, and bottom right - all types) after the normalization.

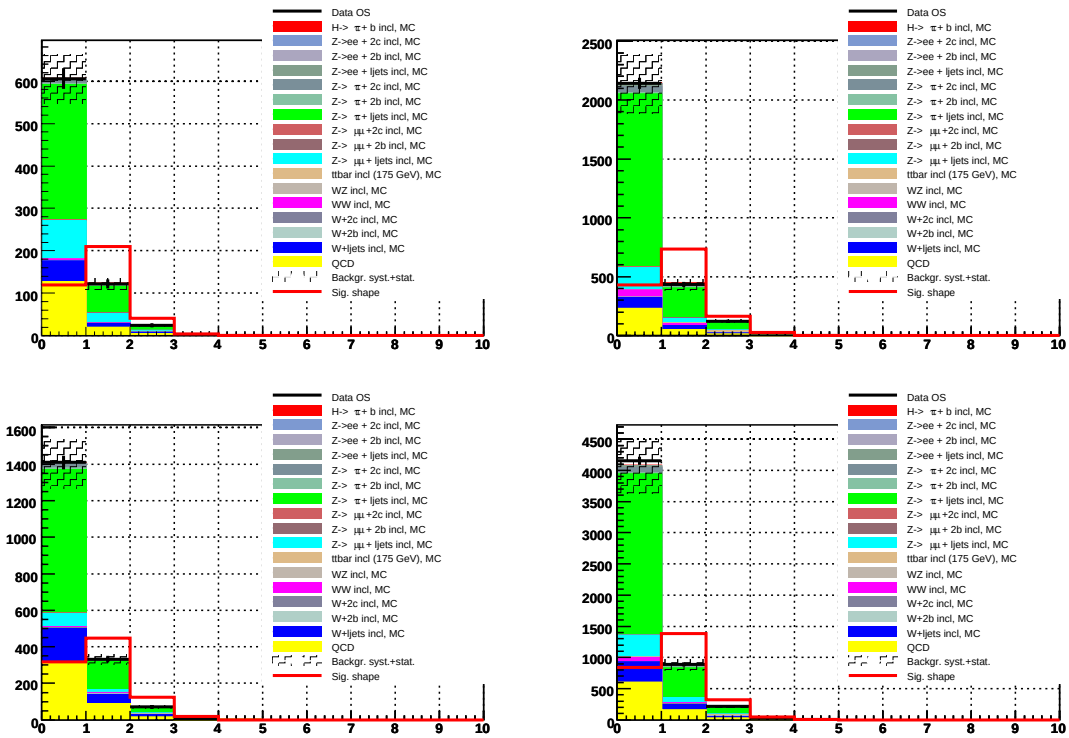

Figure 4.34. Isolated jet multiplicity with reference final selection cuts, Sec. 4.4, for the three τ-types (top left - type 1, top right - type 2, bottom left - type 3, and bottom right - all types) after the normalization.

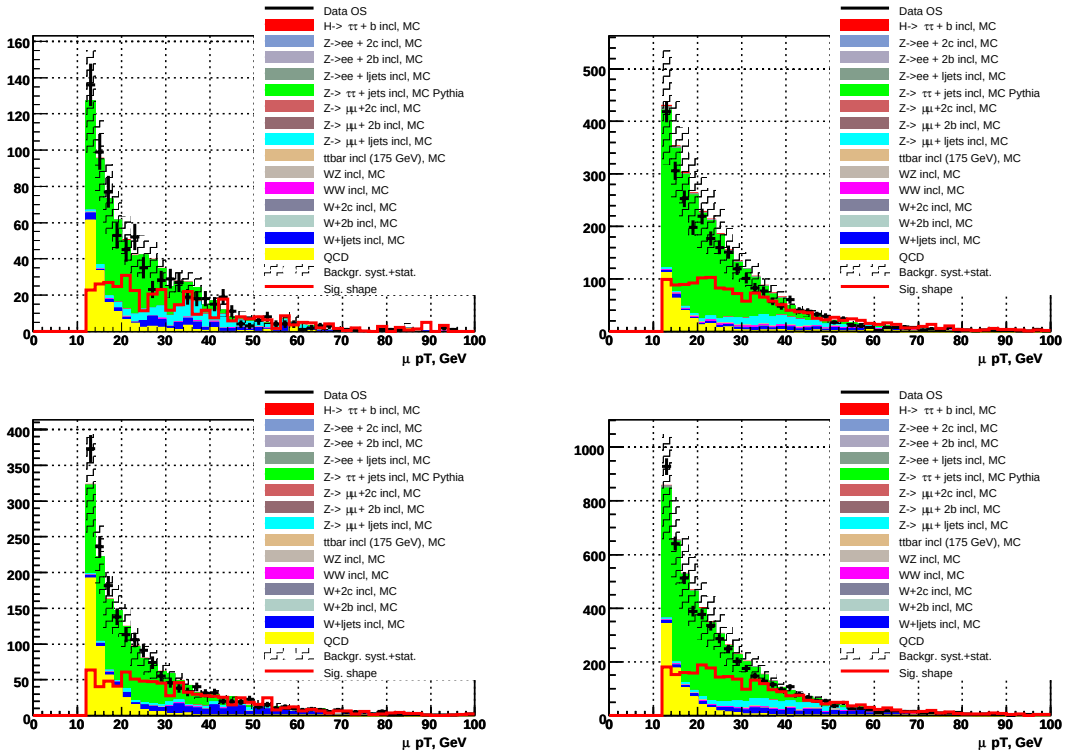

Figure 4.35. Muon p_T, with reference cuts, without requiring an extra isolated jet for the three τ-types (top left - type 1, top right - type 2, bottom left - type 3, and bottom right - all types). $Z \to \tau^+\tau^-$ background is simulated with PYTHIA.

4.5.5 $Z + jets \rightarrow ll + jets$ estimation from data

The $Z + jets \rightarrow ll + jets$ background can also be estimated differently using data. The number of events having at least one isolated b-tagged jet relative to the number of events having at least one taggable isolated jet (b-tagging rate) is assumed to be the same for $Z + jets \rightarrow \tau^+\tau^- + jets$, $Z + jets \rightarrow \mu^+\mu^- + jets$, and $Z + jets \rightarrow e^+e^- + jets$ components of this background. A clean sample of $Z + jets \rightarrow \mu^+\mu^- + jets$ with dimuon invariant mass between 70 and 110 GeV was extracted from the dataset[42] by requiring two non-cosmic isolated muons, see Section 4.4.1, with $p_T^\mu > 15$ GeV, and the b-tagging rate of $1.97 \pm 0.13\%$ measured for this sample for NN_TIGHT b-tagger.

This measured b-tagging rate is then applied to the estimated number of $Z + jets \rightarrow ll + jets$ events in the data. The latter is defined as:

$$N_{Zj,OS} = N_{OS} - N_{QCD,OS} - (N_{t\bar{t}} + N_{W+jets} + N_{WW})_{OS} - N_{signal,OS} \ , \qquad (4.16)$$

where N_{OS} is the number of OS events events in the data, $N_{QCD,OS}$ is taken from Eq. (4.15), and the rest of the backgrounds, as well as the signal, are estimated from MC. All variables in Eq. (4.16) refer to the number of events *before* b-tagging. Then:

$$N_{Zb,OS} = N_{Zj,OS} \cdot (b{-}tagging\, rate) \ . \qquad (4.17)$$

where $N_{Zb,OS}$ is the number of resulting total $Z + jets \rightarrow ll + jets$ background.

Figure 4.36 shows the distribution of the visible mass after application of reference cuts and NN_TIGHT b-tag.

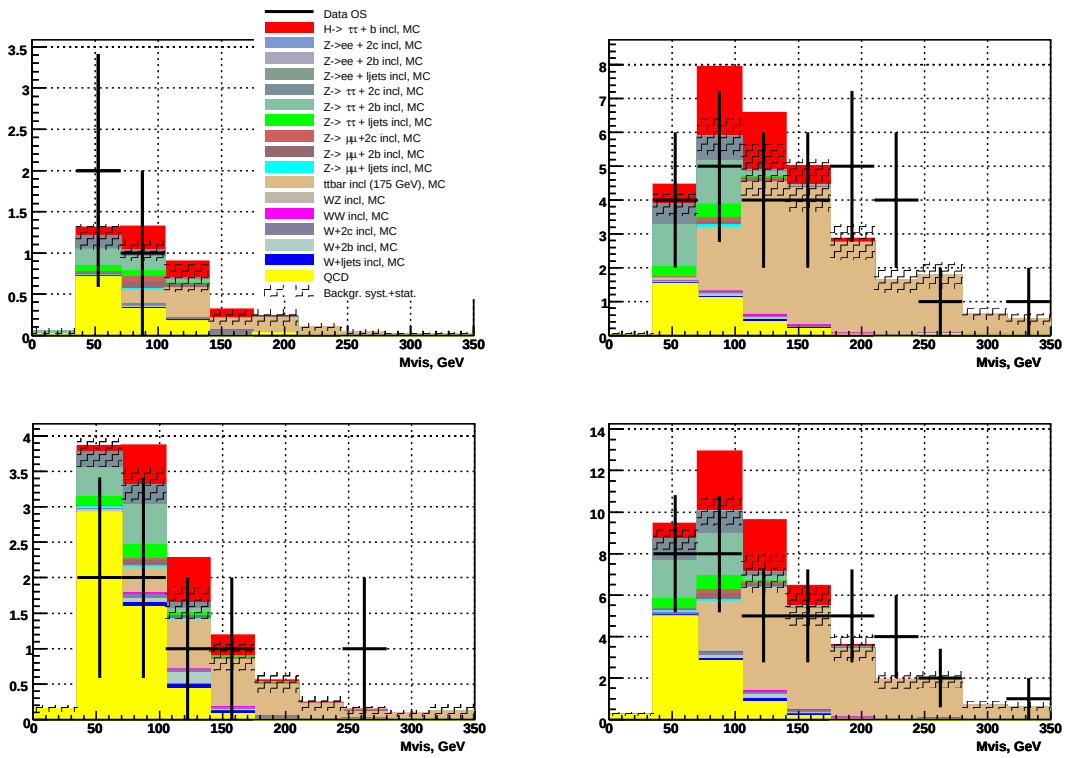

Figure 4.36. μ, τ, and $\not{E}_T$ invariant mass (visible mass) with reference final selection cuts and NN_TIGHT b-tag, for the three τ-types (top left - type 1, top right - type 2, bottom left - type 3, and bottom right - all types).

4.5.6 $t\bar{t}$ background

After b-tagging, the $t\bar{t} \rightarrow \mu\tau_h + b\bar{b}$ is the largest background. $t\bar{t}$ events have two high p_T b-jets, a high p_T muon and a high p_T hadronic tau. On the contrary, b-jets in the signal events have relatively low p_T. In order to remove the $t\bar{t}$ background, we use a kinematic neural network (KNN).

The KNN has four input variables and one hidden layer with nine neurons. The input variables are the following:

- HT: Sum of the E_T's of the jets in the event (excluding the τ-jet)
- MHT: Missing HT constructed from the jets and selected μ and τ_h
- Njet: Number of jets in the event
- mutau_dphi: $\Delta\phi$ between μ and τ_h

The background sample used for training the KNN was $t\bar{t} \rightarrow \mu\tau_h$ events from a $t\bar{t}$ PYTHIA inclusive sample, which passed all selection cuts except b-tagging. The signal sample used for training the KNN was a mixture of $bh \rightarrow b\tau\tau \rightarrow b\mu\tau_h$ events with different Higgs masses, which also passed all cuts except b-tagging. The KNN input variable distributions are shown in Figures 4.37, 4.38, 4.39, 4.40. Figure 4.41 shows the KNN output for Higgs mass of 150 GeV.

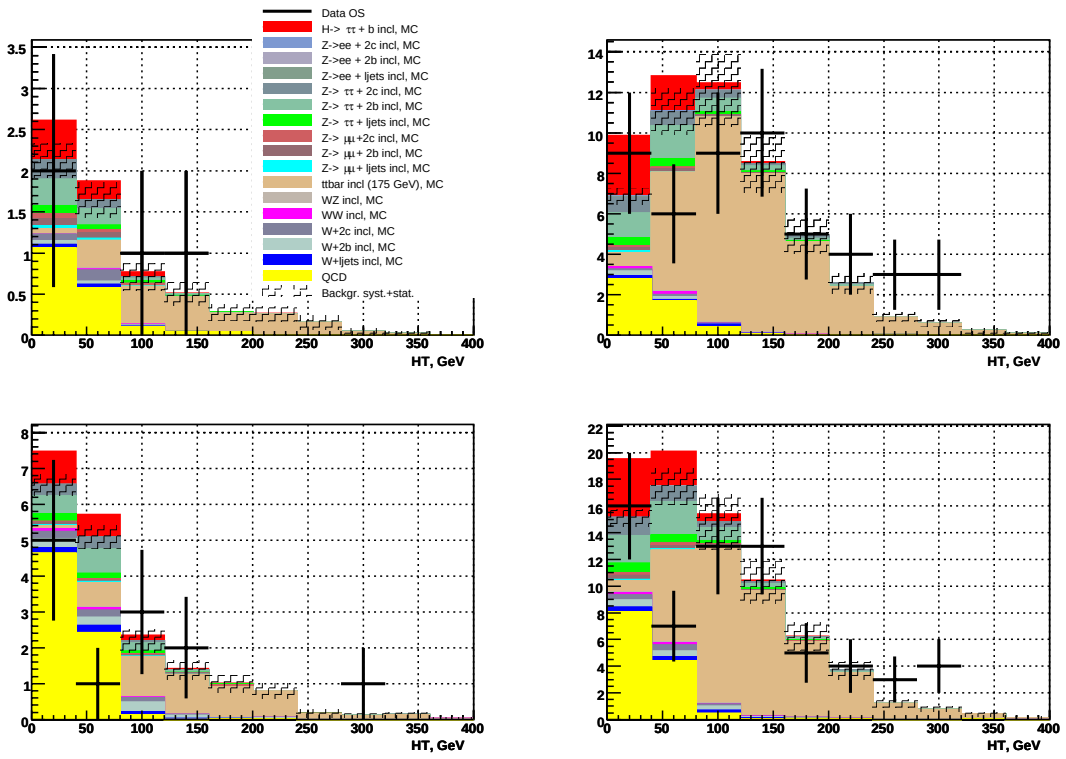

Figure 4.37. KNN variable HT with reference final selection cuts and $\Delta\phi(\mu,\tau) > 0.5$ cut, Sec. 4.4, with a NN_TIGHT b-tag for the three τ-types (top left - type 1, top right - type 2, bottom left - type 3, and bottom right - all types). Signal with Higgs mass 150 GeV is shown in red.

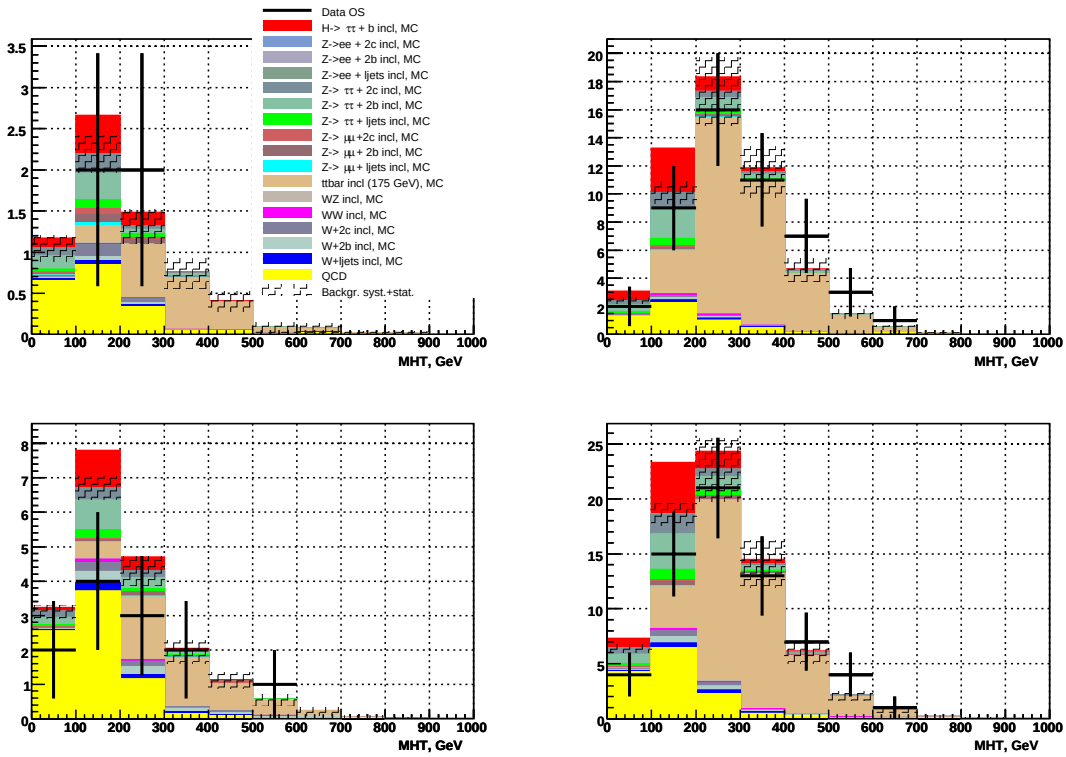

Figure 4.38. KNN variable MHT with reference final selection cuts and $\Delta\phi(\mu,\tau) > 0.5$ cut, Sec. 4.4, with a NN_TIGHT b-tag for the three τ-types (top left - type 1, top right - type 2, bottom left - type 3, and bottom right - all types). Signal with Higgs mass 150 GeV is shown in red.

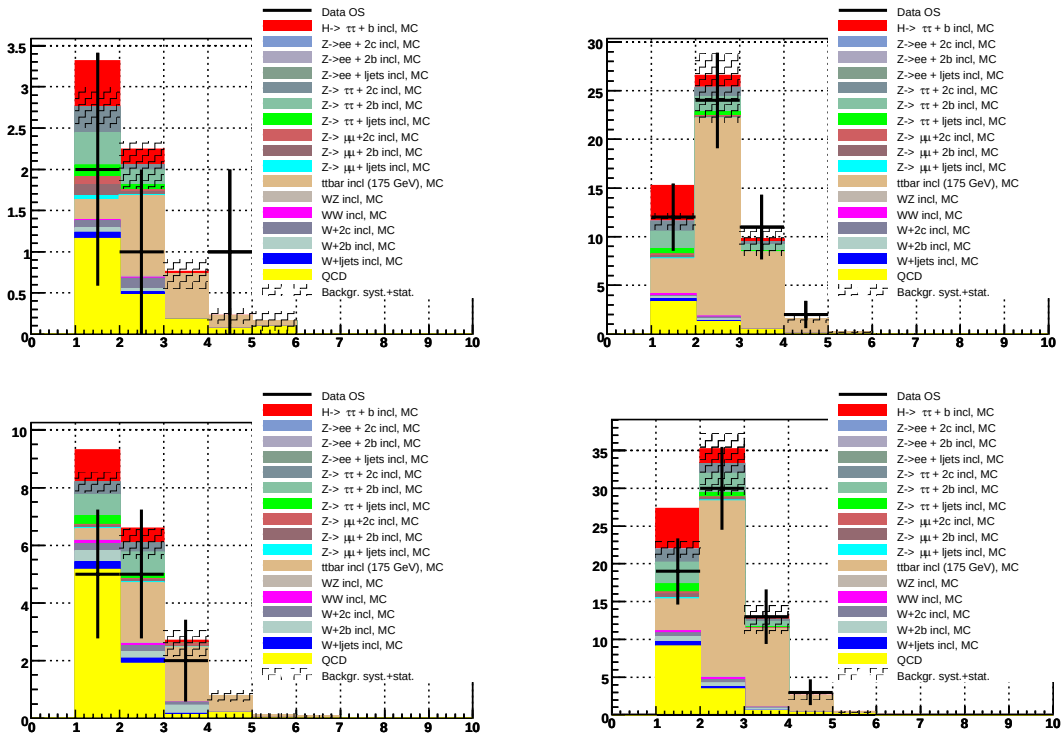

Figure 4.39. KNN variable Njet with reference final selection cuts and $\Delta\phi(\mu,\tau) > 0.5$ cut, Sec. 4.4, with a NN_TIGHT b-tag for the three τ-types (top left - type 1, top right - type 2, bottom left - type 3, and bottom right - all types). Signal with Higgs mass 150 GeV is shown in red.

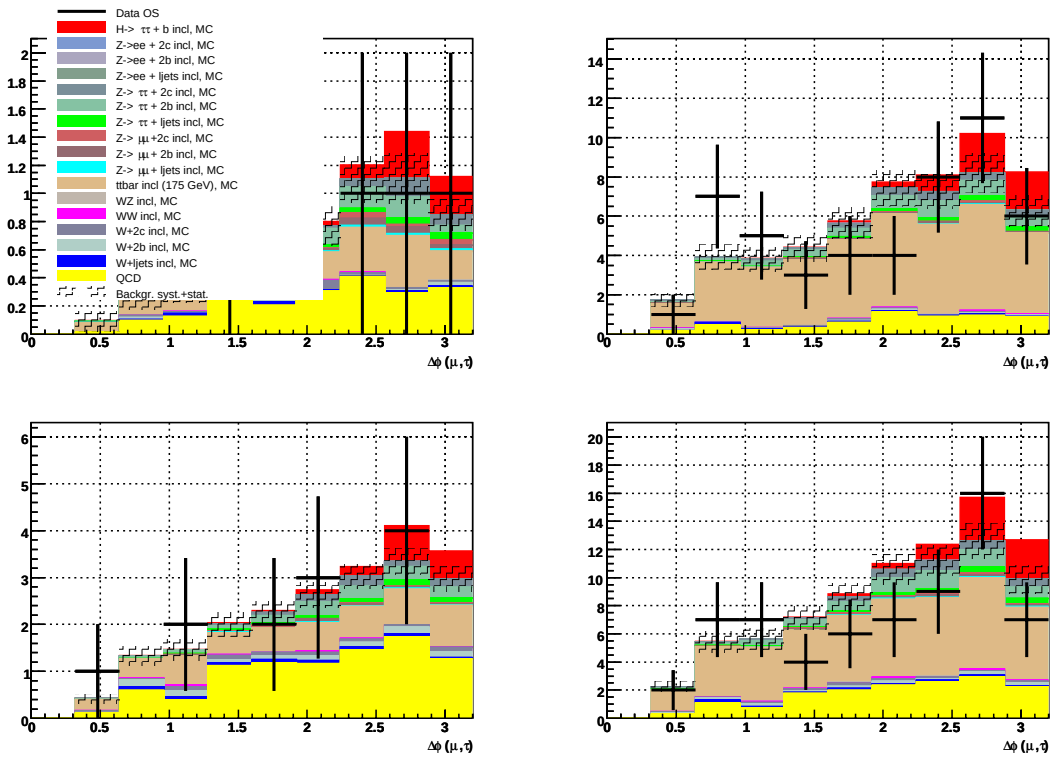

Figure 4.40. KNN variable mutau_dphi with reference final selection cuts and $\Delta\phi(\mu,\tau) > 0.5$ cut, Sec. 4.4, with a NN_TIGHT b-tag for the three τ-types (top left - type 1, top right - type 2, bottom left - type 3, and bottom right - all types). Signal with Higgs mass 150 GeV is shown in red.

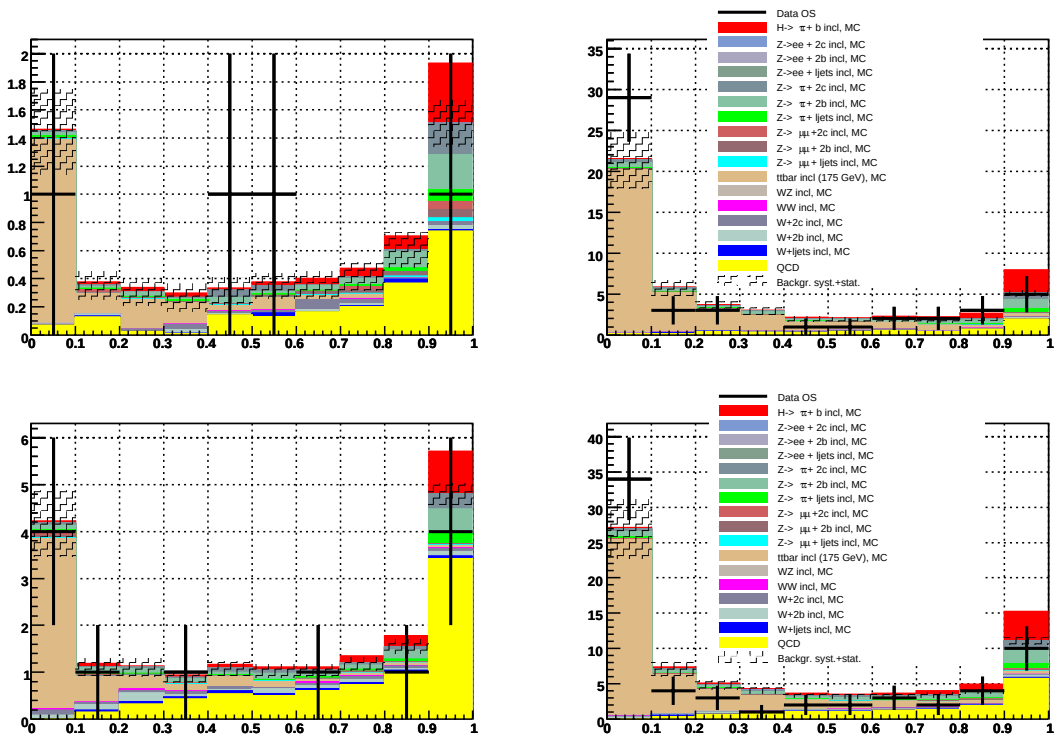

Figure 4.41. KNN output with reference final selection cuts and $\Delta\phi(\mu,\tau) > 0.5$ cut, Sec. 4.4, with a NN_TIGHT b-tag for the three τ-types (top left - type 1, top right - type 2, bottom left - type 3, and bottom right - all types). Signal with Higgs mass 150 GeV is shown in red.

4.6 Monte Carlo cross check. Event Kinematic Distributions.

As a cross check we plot different kinematic distributions after applying all the MC normalization corrections from Section 4.5. Figures 4.42, 4.43, 4.44, 4.45,4.46, 4.47, 4.48 show muon, τ p_T, det η, and ϕ distributions and $\not{E}_T$ before requiring an extra jet, and Figures 4.49, 4.50, 4.51 show p_T, det η and ϕ of the leading isolated jet.

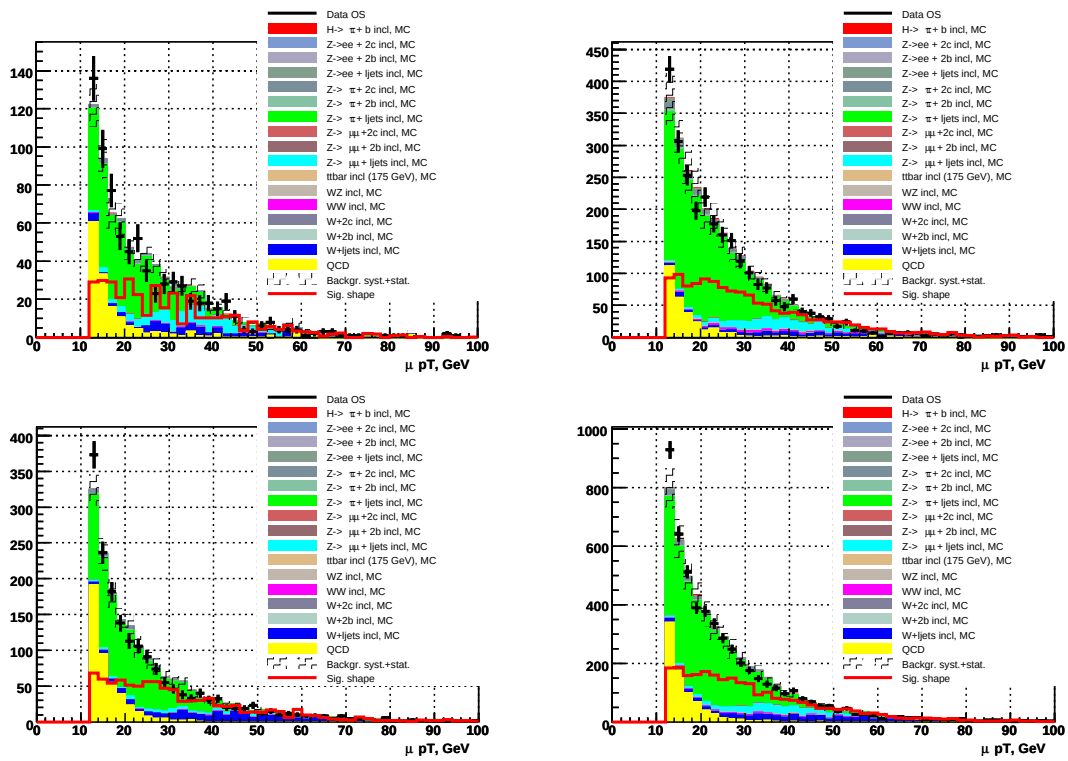

Figure 4.42. p_T^{μ} with reference final selection cuts, without requiring an extra isolated jet, for the three τ-types (top left - type 1, top right - type 2, bottom left - type 3, and bottom right - all types).

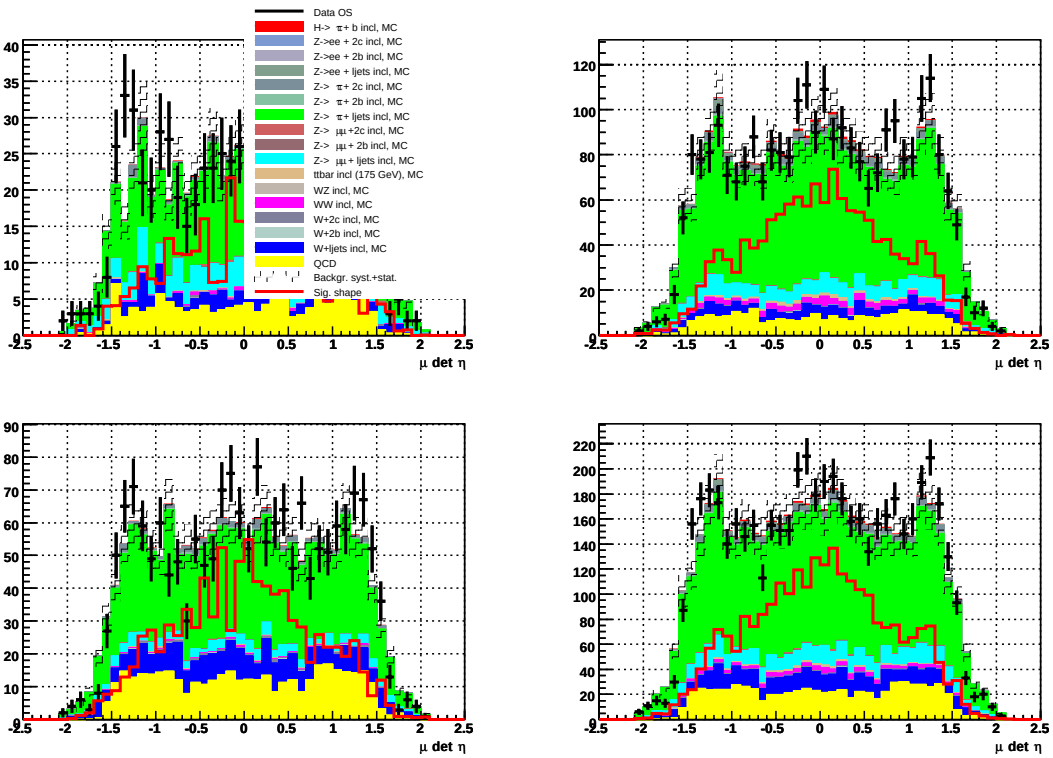

Figure 4.43. muon det η with reference final selection cuts, without requiring an extra isolated jet, for the three τ-types (top left - type 1, top right - type 2, bottom left - type 3, and bottom right - all types).

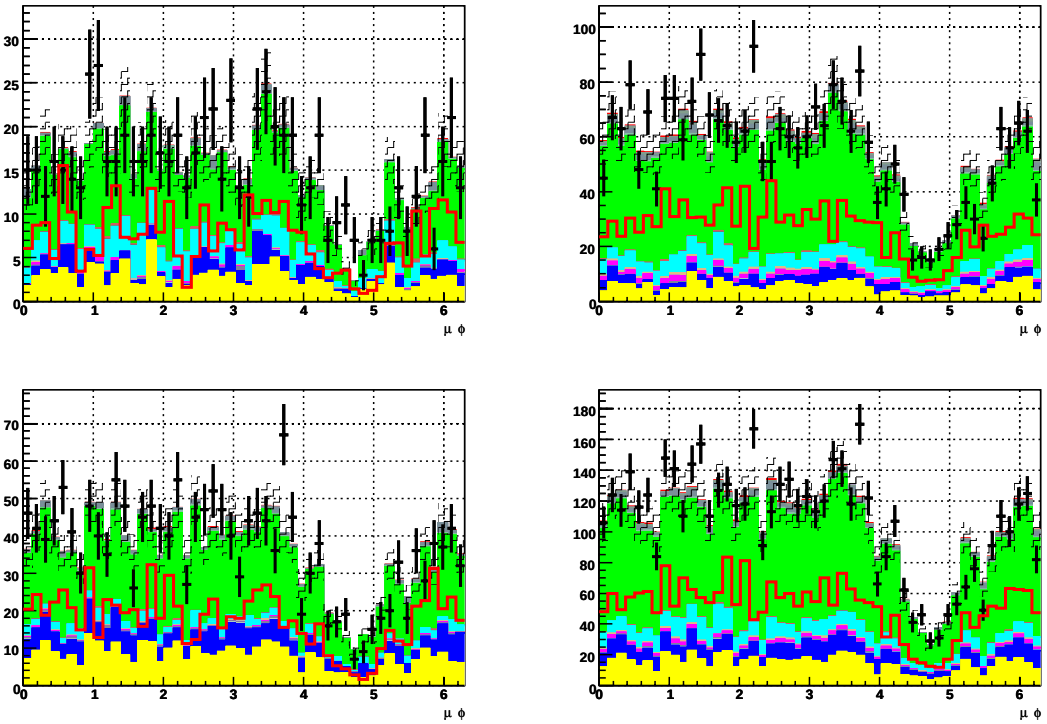

Figure 4.44. muon ϕ with reference final selection cuts, without requiring an extra isolated jet, for the three τ-types (top left - type 1, top right - type 2, bottom left - type 3, and bottom right - all types). Color code is the same as in Fig. 4.43

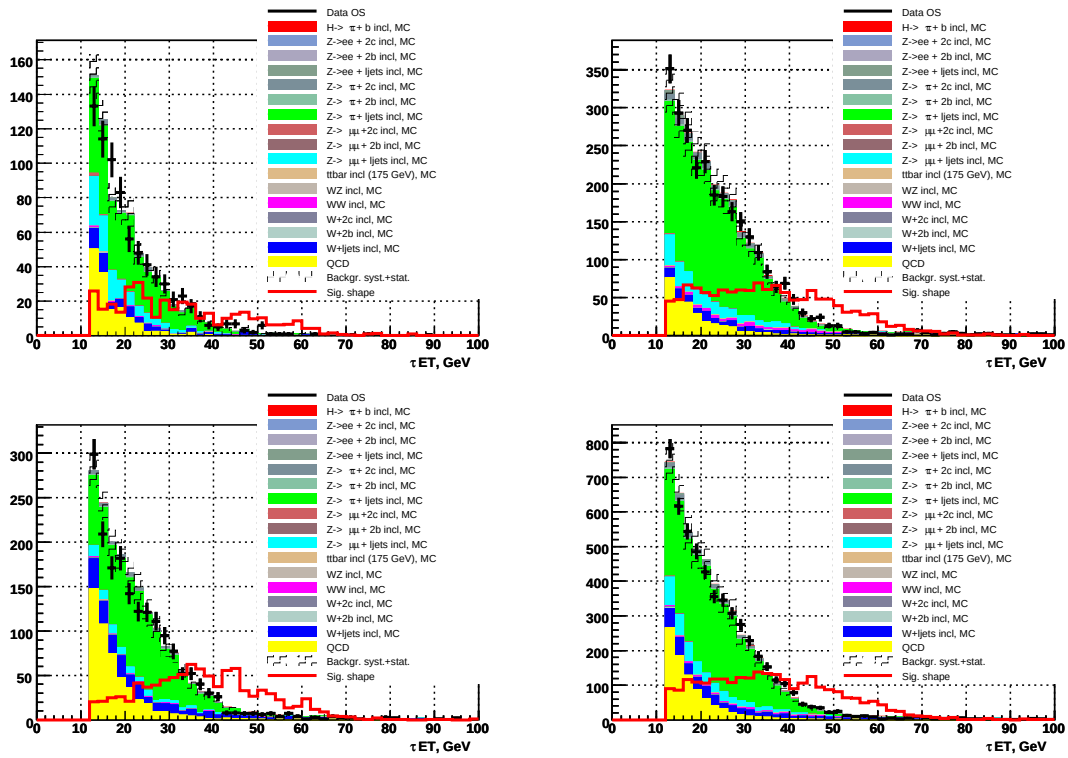

Figure 4.45. p_T^τ with reference final selection cuts, without requiring an extra isolated jet, for the three τ-types (top left - type 1, top right - type 2, bottom left - type 3, and bottom right - all types).

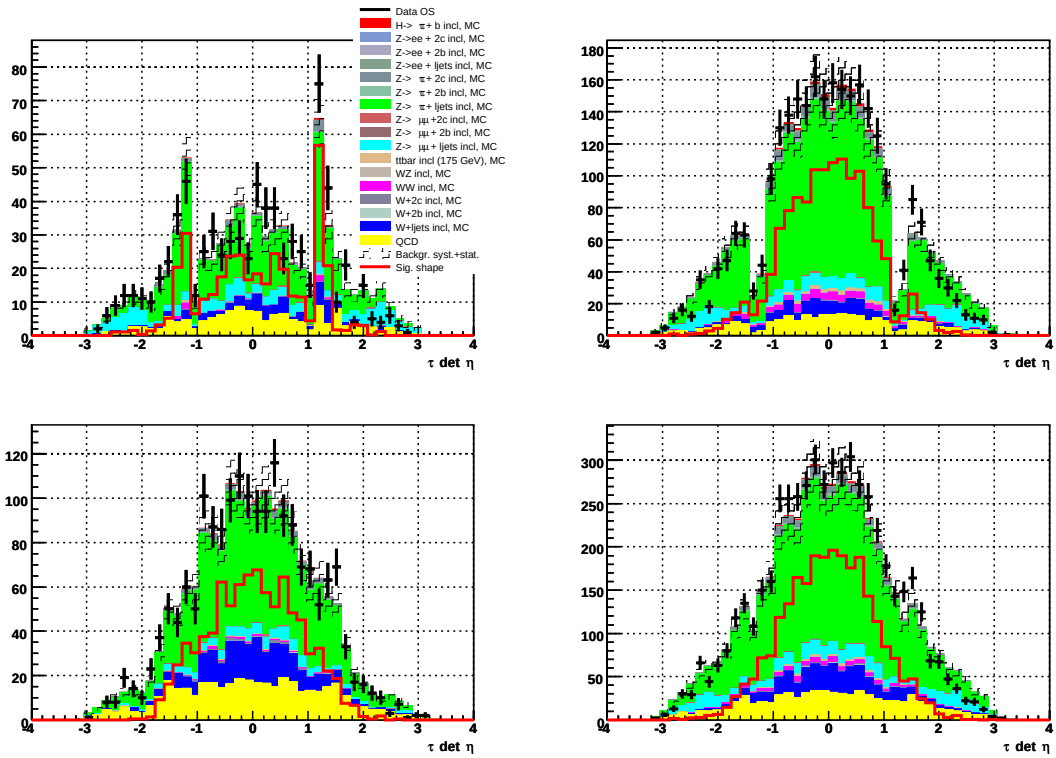

Figure 4.46. τ det η with reference final selection cuts, without requiring an extra isolated jet, for the three τ-types (top left - type 1, top right - type 2, bottom left - type 3, and bottom right - all types).

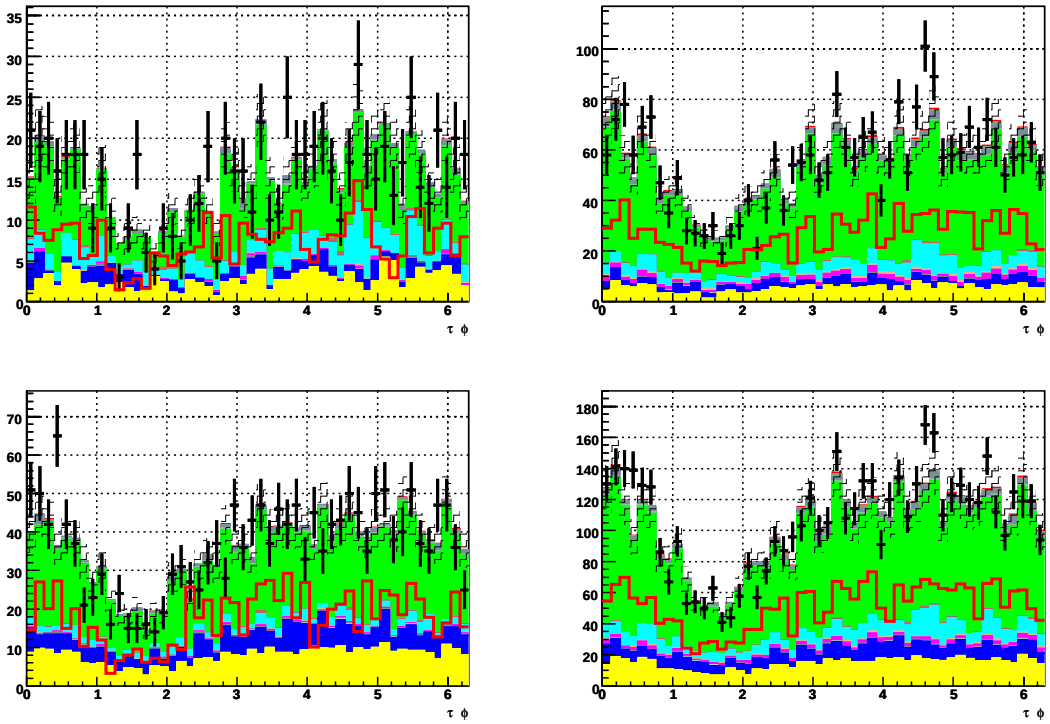

Figure 4.47. τ ϕ with reference final selection cuts, without requiring an extra isolated jet, for the three τ-types (top left - type 1, top right - type 2, bottom left - type 3, and bottom right - all types). Color code is the same as in Fig. 4.46

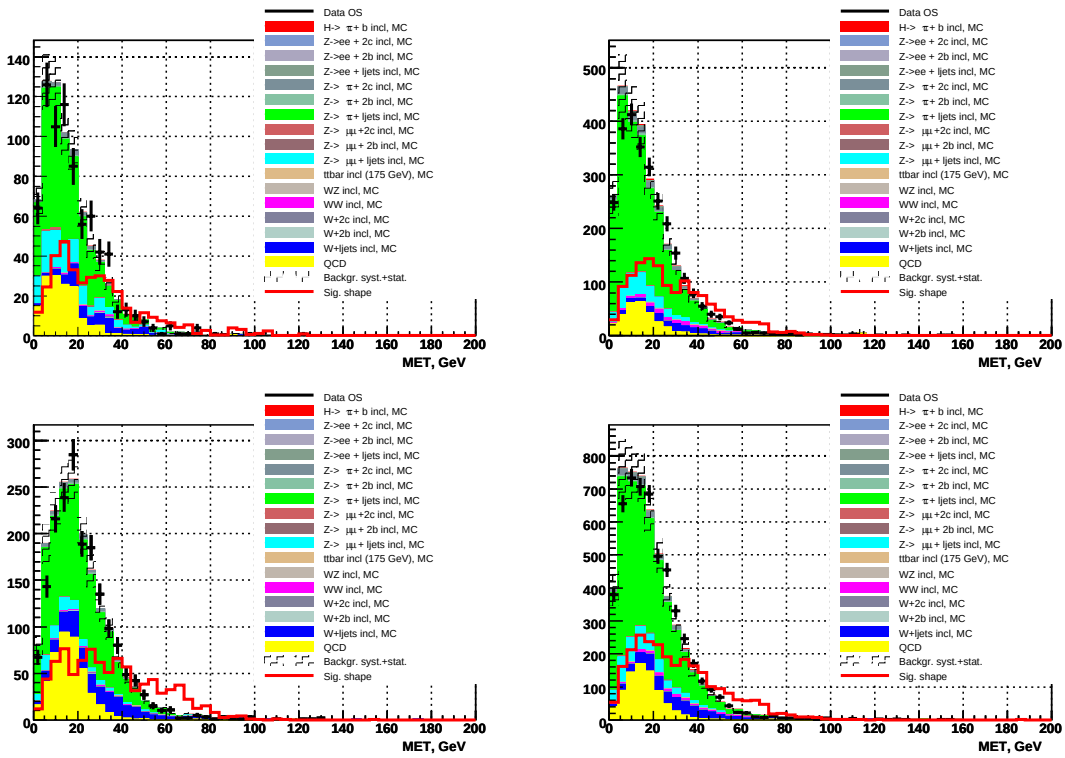

Figure 4.48. $\not\!\!E_T$ with reference final selection cuts, without requiring an extra isolated jet, for the three τ-types (top left - type 1, top right - type 2, bottom left - type 3, and bottom right - all types).

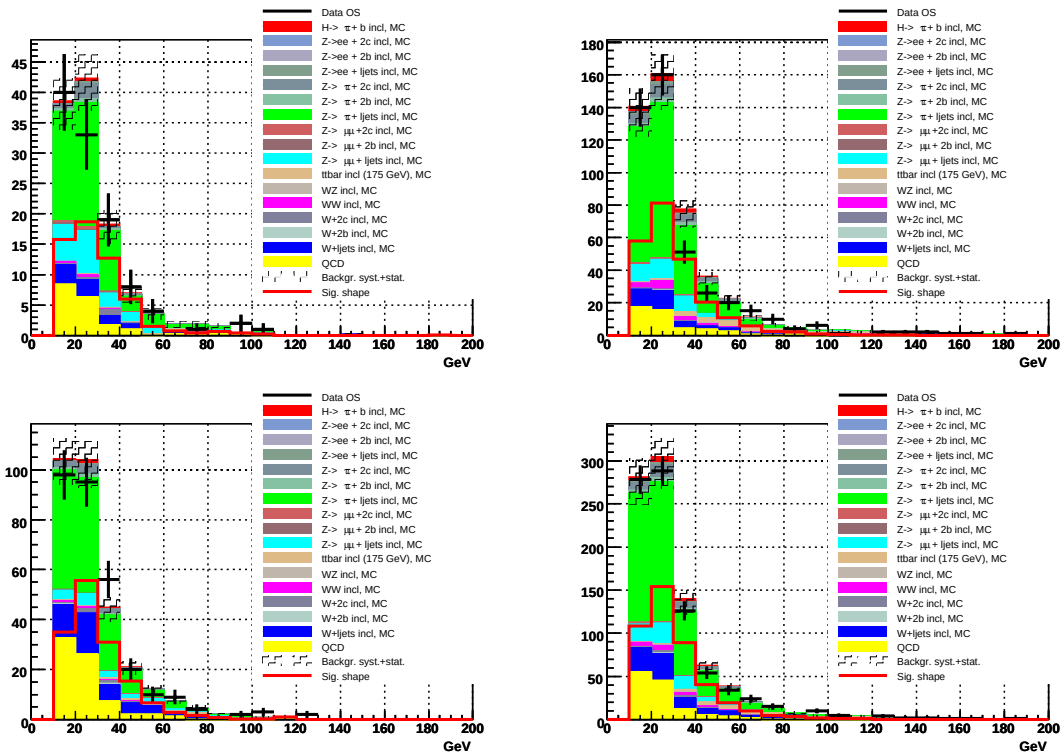

Figure 4.49. Leading isolated taggable jet p_T with reference final selection cuts, for the three τ-types (top left - type 1, top right - type 2, bottom left - type 3, and bottom right - all types).

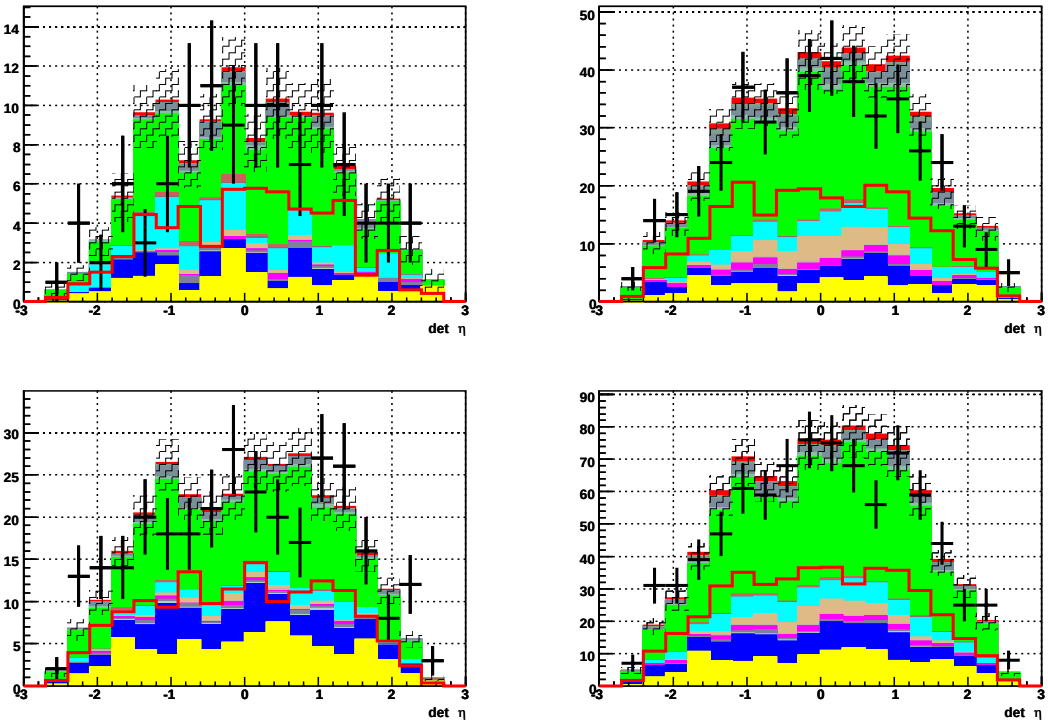

Figure 4.50. Leading isolated taggable jet $det\eta$ with reference final selection cuts, for the three τ-types (top left - type 1, top right - type 2, bottom left - type 3, and bottom right - all types).

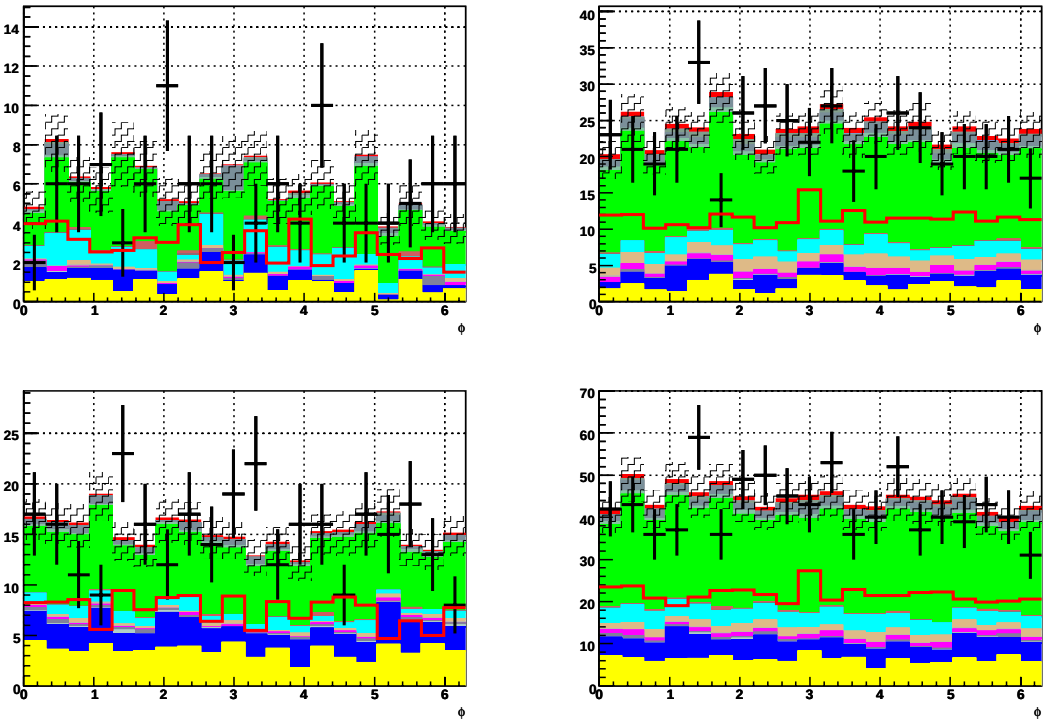

Figure 4.51. Leading isolated taggable jet ϕ with reference final selection cuts, for the three τ-types (top left - type 1, top right - type 2, bottom left - type 3, and bottom right - all types).

4.7 Systematic Uncertainties

For backgrounds derived from data, the systematic errors result from the statistical errors of the background estimates. Also a 30% systematic error is assigned to the QCD estimate due to the observed differences in total predicted QCD background for various kinematic distributions.

For backgrounds derived from Monte Carlo, the following systematic errors are included in the calculations:

- The Jet Energy Scale uncertainty is estimated by moving the energy scale of all jets in each MC sample (signal and background) by $\pm 1\sigma$, and calculating the new acceptances [57]. Similarly for the Jet Reconstruction Efficiency uncertainty.
- A 5% uncertainty is assigned to the signal and backrounds taken from MC acceptances due to the missing τ energy scale correction.
- The TRF uncertainty is estimated from the uncertainty on the TRF from respective b-tagger according to jet multiplicity, see Table 4.10. Taggability systematic is around 10% of the TRF systematic on average, and is absorbed into the TRF systematic.
- The NN_τ uncertainty is taken from [58].
- The muon trigger efficiency systematic uncertainty is obtained by varying the trigger weight for each MC event by $\pm 1\sigma$.
- The luminosity uncertainty is taken to be equal to 6.1%.
- A flat 10% uncertainty is assigned to all MC cross sections.

In Tab. 4.10 the systematic errors on the background are quoted for the reference cuts, Higgs signal with mass 150 GeV, NN_TIGHT b-tagger, and KNN cut 0.6 and $Z + jets \rightarrow ll + jets$ estimation from data. Almost all errors except the QCD systematic are applied to backgrounds estimated from Monte Carlo. QCD systematic is applied to the amount of QCD multijet backround, estimated from data, see Section 4.5.3. This is why systematic uncertainties on the sum of the backgrounds can be small, if the amounts of MC simulated backgrounds are small in the total background.

TABLE 4.10

RELATIVE SYSTEMATIC UNCERTAINTIES (IN %) ON THE NUMBER OF SIGNAL AND BACKGROUND EVENTS.

	Type 1		Type 2		Type 3	
	Signal	Bkgd	Signal	Bkgd	Signal	Bkgd
Luminosity	6.1	0.4	6.1	1.4	6.1	0.5
Trigger	10.0	0.6	10.0	2.2	10.0	0.8
NN_τ	3.8	0.2	1.2	0.3	3.7	0.3
Jet Reco Eff.	9.0	0.6	7.5	1.7	6.5	0.5
JES syst.	3.7	0.2	1.5	0.3	2.0	0.2
τ ES syst.	5.0	0.3	5.0	1.1	5.0	0.4
TRF syst.	5.5	0.3	5.0	1.1	5.0	0.4
Z+jet b-rate		3.4		3.3		2.0
QCD		13.0		8.3		18.4
MC x-section	10.0	0.6	10.0	2.2	10.0	0.8

CHAPTER 5

EXPERIMENTAL RESULTS

5.1 Final Selection and Results

In the first proposed $Z + jets \rightarrow ll + jets$ background estimation scheme, as in Section 4.5.4, where $Z + jets \rightarrow ll + jets$ backgrounds are estimated from Alpgen MC in the pre-tagged sample, the agreement between the data and the sum of the backgrounds is not unreasonable, as seen from the visible mass plot, Figure 5.1. The second scheme, where the $Z + jets \rightarrow ll + jets$ background is estimated from data, see Section 4.5.5, gives almost perfect agreement by definition, due to the negligible amount of simulated signal at this stage, Figure 5.2.

Also, comparing the estimated total background obtained from Alpgen MC, as in Figure 5.3, and from data, as in Figure 5.4 we see that although they agree within systematical uncertainties for the chosen HF/LF scale factor of 1.33, see Section 4.5.2 above, a perfect agreement would be reached by applying a factor of 1.8. There is large uncertainty associated with the measurement of this factor, ~ 0.5, which is around 40%, see [56]. It means that previous studies do not provide a satisfactory measurement of this scale factor. On the other hand the data normalization scheme gives a low systematic uncertainty associated with the normalization of the $Z + jets \rightarrow ll + jets$ background after b-tagging. The fact that we do not know our leading irreducible background $Z + b(c)jets \rightarrow ll + b(c)jets$ better than the systematic error on the b-tagging rate measured in $Z + b(c)jets \rightarrow \mu^+\mu^- + b(c)jets$ data,

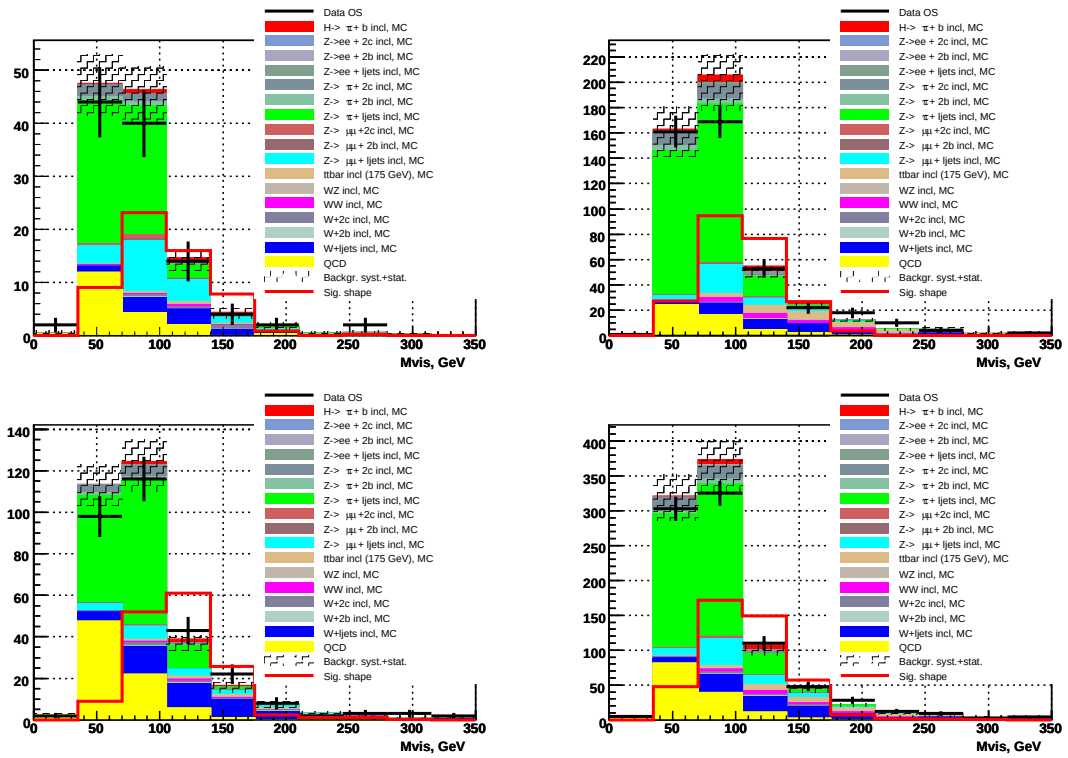

Figure 5.1. μ, τ, and $\not{E}_T$ invariant mass (visible mass) with reference final selection cuts, for the three τ-types (top left - type 1, top right - type 2, bottom left - type 3, and bottom right - all types).

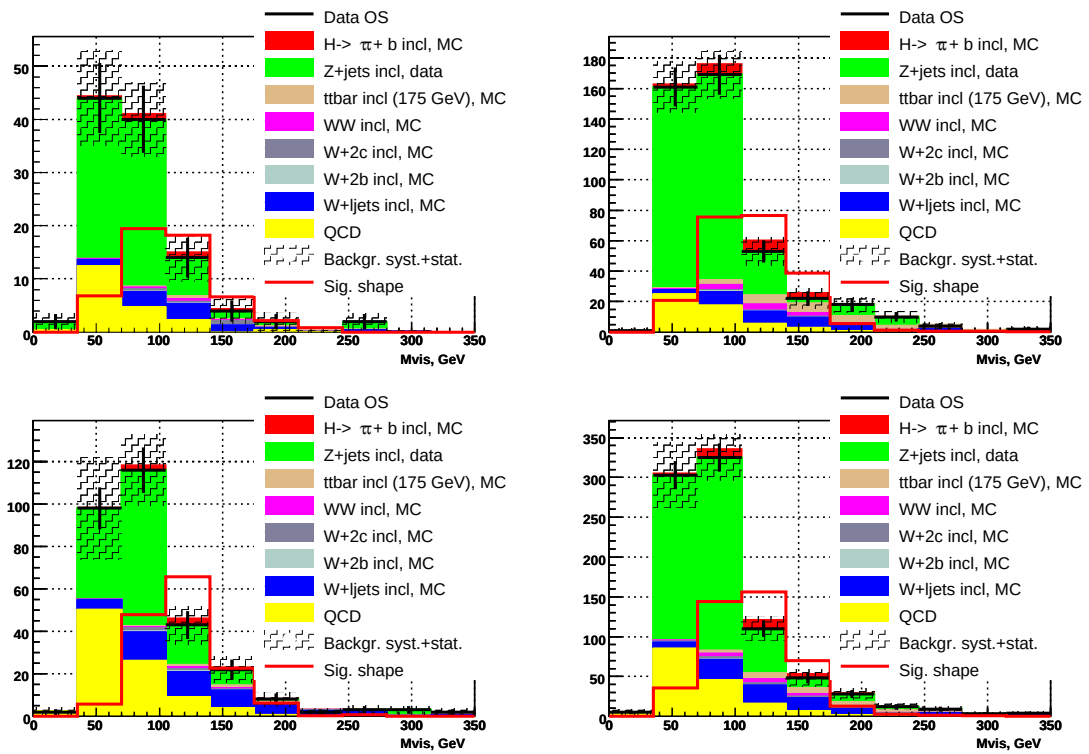

Figure 5.2. μ, τ, and $\not{E}_T$ invariant mass (visible mass) with reference final selection cuts, for the three τ-types (top left - type 1, top right - type 2, bottom left - type 3, and bottom right - all types). $Z + jets \rightarrow ll + jets$ background is estimated normalizing to data in the no signal hypothesis.

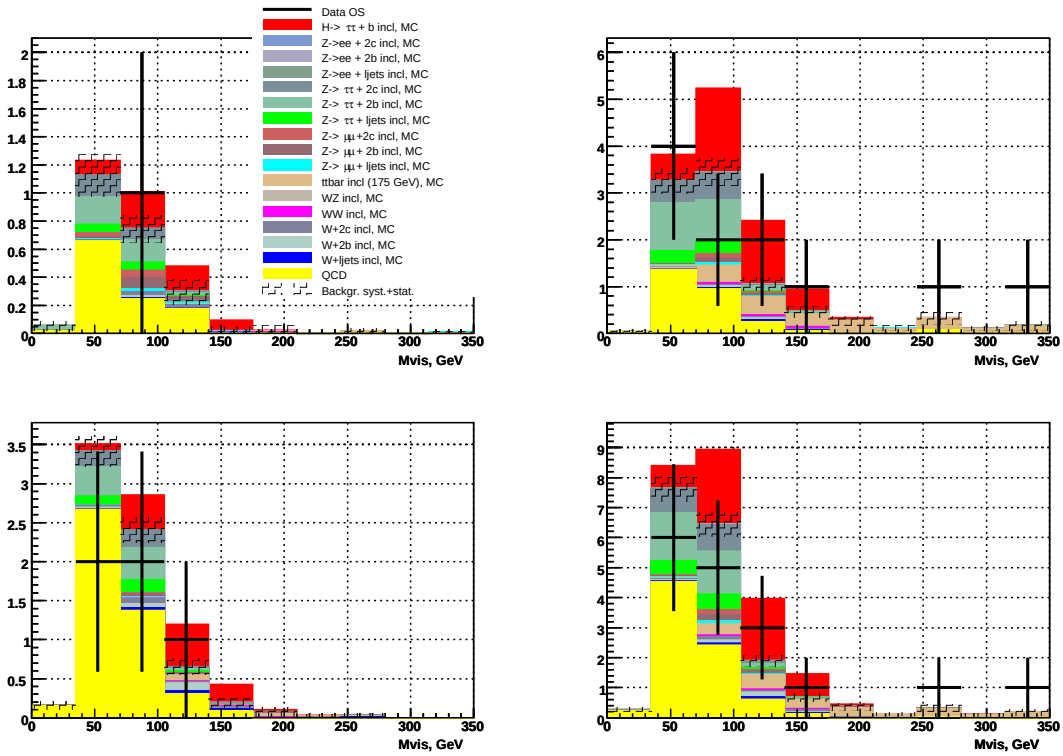

Figure 5.3. μ, τ, and $\not{E}_T$ invariant mass (visible mass) with reference final selection cuts, NN_TIGHT b-tag, and KNN cut 0.6, where all backgrounds are estimated from MC, for the three τ-types (top left - type 1, top right - type 2, bottom left - type 3, and bottom right - all types).

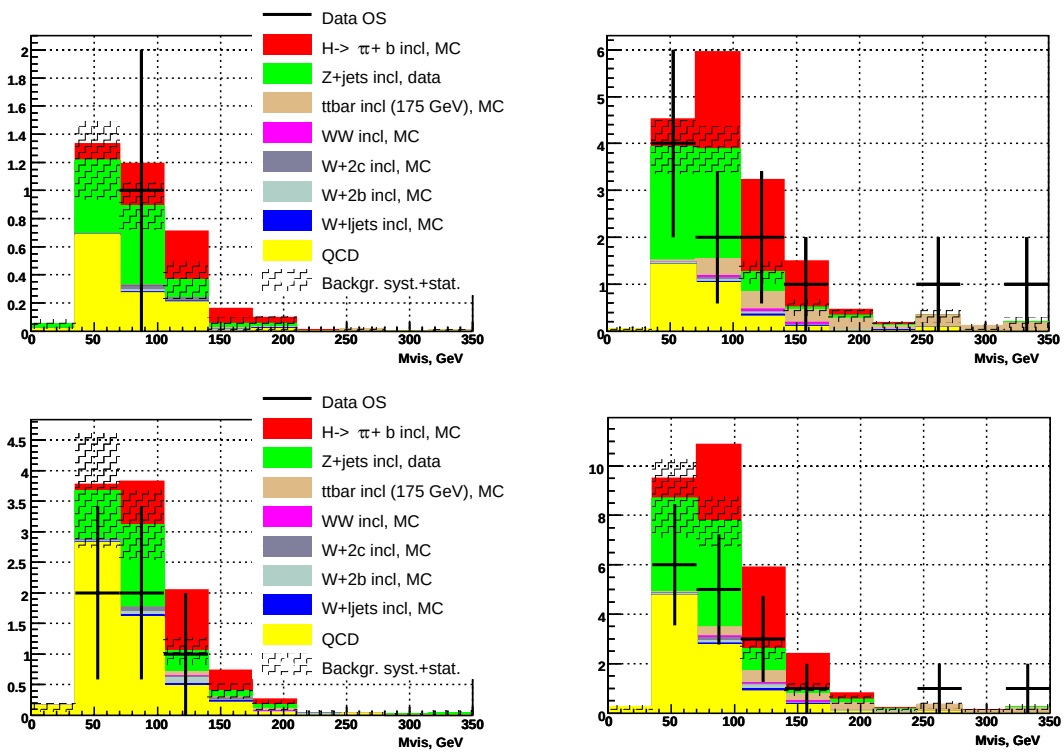

Figure 5.4. μ, τ, and $\not{E}_T$ invariant mass (visible mass) with reference final selection cuts, NN_TIGHT b-tag, and KNN cut 0.6, where $Z + jets \rightarrow ll + jets$ background is estimated from data, for the three τ-types (top left - type 1, top right - type 2, bottom left - type 3, and bottom right - all types).

which is around 6.5%, see Table 4.10, suggests using data normalization for this background, which is a procedure, alternative to those described in Sections 4.5.2-4.5.4, and described in Sec. 4.5.5. Figures 5.3, 5.4 show visible mass distibutions after reference cuts, NN_TIGHT b-tagger to further remove light flavor jets, and KNN cut of 0.6, to cut down $t\bar{t}$ events.

5.1.1 Event Cut Flow

The event yields after the various reference cuts in the data and MC are shown in Tables 5.1-5.3. The Higgs signal MC is normalized to 1 pb. We chose to show the signal MC with the mass 150 GeV as an example of the behaviour of signal acceptances with the cut flow. Its optimal sensitivity cross section is close to the minimal one observed in this analysis. $Z + b(c)jets \rightarrow ll + b(c)jets$ background is calculated using the procedure in Section 4.5.5

TABLE 5.1

DATA AND MC CUT FLOW TABLE FOR τ TYPE 1

	Data OS	QCD	$M_H = 150$ GeV	Z+jets	$t\bar{t}$	W+jets	WW
PreSel	24824	22811	6.07	1052	7.89	934.2	19.42
MuIso	5355	3342	6.04	1051	7.89	933.8	19.42
Tau Pt	2253	1212	5.12	574.3	5.70	446.7	13.81
dPhi	1970	1081	4.95	616.8	2.77	261.5	8.41
TauNN	756	164.8	3.65	520.8	1.51	62.72	6.14
TAjet	108	20.13	1.97	73.81	1.46	11.39	1.19
btag	3	1.213	0.727	1.431	0.987	0.177	0.016
KNN	1	1.111	0.633	1.306	0.041	0.098	0.009

The selection criteria are summarized below:

- PreSel: Preselection cuts (Sec. 4.4.5); $\Delta\phi(\mu, \tau_h) > 0.5$; $NN_\tau > 0.2$, $p_T^\mu > 12$ GeV.
- MuIso: muon isolation (Sec. 4.4.1).

TABLE 5.2

DATA AND MC CUT FLOW TABLE FOR τ TYPE 2

	Data OS	QCD	$M_H = 150$ GeV	Z+jets	$t\bar{t}$	W+jets	WW
PreSel	67464	61767	34.18	3370	71.23	2103	152.2
MuIso	14118	8414	34.13	3377	70.59	2103	152.2
Tau Pt	7037	2850	30.45	2786	63.96	1199.7	137.3
dPhi	6135	2556	29.82	2754	34.16	705.8	85.49
TauNN	2717	318.6	25.27	2160	27.88	137.6	72.88
TAjet	440	52.25	14.03	312.1	26.72	35.06	13.90
btag	28	3.495	5.039	6.048	16.92	0.446	0.221
KNN	11	2.94	4.253	5.332	1.896	0.328	0.144

TABLE 5.3

DATA AND MC CUT FLOW TABLE FOR τ TYPE 3

	Data OS	QCD	$M_H = 150$ GeV	Z+jets	$t\bar{t}$	W+jets	WW
PreSel	218091	209571	13.86	1272	83.17	7049	116.1
MuIso	27224	18722	13.82	1255	82.10	7049	116.0
Tau Pt	15640	9286	13.36	899.6	76.50	5272	104.8
dPhi	12559	8212	12.92	985.7	41.43	3258	60.84
TauNN	1815	529.1	9.35	1018.4	4.69	253.2	9.56
TAjet	299	93.43	4.67	145.4	4.36	52.75	3.06
btag	7	6.222	1.642	2.818	2.654	0.748	0.054
KNN	5	5.287	1.367	2.665	0.164	0.472	0.035

- Tau Pt: $E_T^\tau > 12$ GeV for τ_h type = 1,2,3.
- dPhi: $\Delta\phi(\mu, \tau_h) > 2.0$ (cut 4 in Section 4.4.2).
- Tau NN: reference $minNN_\tau$ cut (as described in Sec. 4.4.2).
- TAjet: at least one jet in the event satisfying all requirements in Sec. 4.4.3 and being taggable.
- KNN: Kinematic Neural Network 0.6 cut (as described in Section 4.5.6).
- btag: at least one b-tagged jet (NNTIGHT).

In the absence of a significant signal, upper limits for the production cross section times branching ratio are set using the modified frequentist approach [59]. In order to maximize the sensitivity, each τ_h type is treated as a separate channel, and reference cuts are optimized separately for each hypothetical signal mass. Visible mass[1] was considered the most suitable variable to exploit differences in shape between signal and background in the calculation of the limit. In each channel, the visible mass distribution is split in 10 bins. The optimal cuts were chosen by global minimization of the expected 95% C.L. limit with respect to parameters p_T^τ, $minNN_\tau$, KNN, and b-tagging working point for all τ-types simultaneously. They are summarized in Table 5.4. Two values for each of the parameters were chosen for the optimization. Optimization on a more refined grid would, in principle, give a lower value, but the difference is of the order of 1%, which is much smaller than the distance from $\pm 1\sigma$ bands, see Figure 5.5. The refinement of the grid was limited by the CPU time constraints, and multidimensional nature of the optimization. The $\pm 1\sigma$ bands show the uncertainty of the expected limit estimation. $minNN_\tau$ cuts for types 1, 3 τ were not optimized and were fixed at 0.9 for type 1, and 0.95 for type 3.

The signal acceptance, number of expected signal events, total number of estimated background events, and number of observed events, for each Higgs mass,

[1] As mentioned earlier, the invariant mass was constructed from the 4-vector momenta of the μ, hadronic τ, and missing E_T of the event.

TABLE 5.4

OPTIMAL CUTS FOR THE 95% C.L. CROSS SECTION TIMES BRANCHING RATIO LIMIT CALCULATION

	$M_H = 90$ GeV	$M_H = 100$ GeV	$M_H = 110$ GeV	$M_H = 120$ GeV
$minNN_\tau$	0.8	0.9	0.9	0.9
KNN	0.4	0.4	0.4	0.4
p_T^τ	12 GeV	12 GeV	12 GeV	16 GeV
b-tag	NNTIGHT	NNTIGHT	NNTIGHT	NNTIGHT
	$M_H = 130$ GeV	$M_H = 140$ GeV	$M_H = 150$ GeV	$M_H = 160$ GeV
$minNN_\tau$	0.9	0.9	0.9	0.9
KNN	0.4	0.8	0.4	0.4
p_T^τ	12 GeV	16 GeV	16 GeV	16 GeV
b-tag	NNTIGHT	NNTIGHT	NNTIGHT	NNTIGHT

optimized cuts from Table 5.4, and each of the three τ_h types, are shown in Tables 5.5-5.7.

TABLE 5.5

τ TYPE 1 SIGNAL ACCEPTANCES AND EVENT YIELDS FOR DIFFERENT HIGGS MASSES. THE EXPECTED SIGNAL IS NORMALIZED TO THE EXPECTED CROSS SECTION AT 95% C.L. LIMIT. QUOTED UNCERTAINTIES REPRESENT STATISTICAL AND SYSTEMATIC ADDED IN QUADRATURE

	$M_H = 90$ GeV	$M_H = 100$ GeV	$M_H = 110$ GeV	$M_H = 120$ GeV
Sig. Accept. (%)	0.036±0.009	0.041±0.010	0.051±0.012	0.041±0.009
Expected Signal	1.50±0.39	1.44±0.34	1.41±0.34	1.05±0.25
Total Bkgd	2.93±0.38	2.93±0.38	2.93±0.38	2.13±0.30
Observed	2	2	2	2
	$M_H = 130$ GeV	$M_H = 140$ GeV	$M_H = 150$ GeV	$M_H = 160$ GeV
Sig. Accept. (%)	0.060±0.013	0.039±0.009	0.058±0.012	0.065±0.013
Expected Signal	1.22±0.27	0.77±0.17	0.91±0.19	0.88±0.18
Total Bkgd	2.93±0.38	1.47±0.25	2.13±0.30	2.13±0.30
Observed	2	1	2	2

TABLE 5.6

τ TYPE 2 SIGNAL ACCEPTANCES AND EVENT YIELDS FOR DIFFERENT HIGGS MASSES. THE EXPECTED SIGNAL IS NORMALIZED TO THE EXPECTED CROSS SECTION AT 95% C.L. LIMIT. QUOTED UNCERTAINTIES REPRESENT STATISTICAL AND SYSTEMATIC ADDED IN QUADRATURE

	$M_H = 90$ GeV	$M_H = 100$ GeV	$M_H = 110$ GeV	$M_H = 120$ GeV
Sig. Accept. (%)	0.19±0.05	0.22±0.05	0.27±0.06	0.27±0.06
Expected Signal	8.01±1.92	7.54±1.72	7.40±1.68	6.86±1.48
Total Bkgd	16.00±1.31	12.70±0.95	12.70±0.95	10.67±0.80
Observed	14	12	12	12
	$M_H = 130$ GeV	$M_H = 140$ GeV	$M_H = 150$ GeV	$M_H = 160$ GeV
Sig. Accept. (%)	0.35±0.07	0.27±0.05	0.42±0.08	0.45±0.09
Expected Signal	7.17±1.46	5.34±1.09	6.57±1.29	6.16±1.16
Total Bkgd	12.70±0.95	6.47±0.54	10.67±0.80	10.67±0.80
Observed	12	8	12	12

TABLE 5.7

τ TYPE 3 SIGNAL ACCEPTANCES AND EVENT YIELDS FOR DIFFERENT HIGGS MASSES. THE EXPECTED SIGNAL IS NORMALIZED TO THE EXPECTED CROSS SECTION AT 95% C.L. LIMIT. QUOTED UNCERTAINTIES REPRESENT STATISTICAL AND SYSTEMATIC ADDED IN QUADRATURE

	$M_H = 90$ GeV	$M_H = 100$ GeV	$M_H = 110$ GeV	$M_H = 120$ GeV
Sig. Accept. (%)	0.064±0.015	0.080±0.019	0.097±0.022	0.090±0.020
Expected Signal	2.70±0.65	2.82±0.68	2.67±0.61	2.31±0.51
Total Bkgd	9.38±1.17	9.38±1.17	9.38±1.17	7.22±0.83
Observed	5	5	5	4
	$M_H = 130$ GeV	$M_H = 140$ GeV	$M_H = 150$ GeV	$M_H = 160$ GeV
Sig. Accept. (%)	0.14±0.03	0.094±0.020	0.14±0.03	0.17±0.04
Expected Signal	2.84±0.62	1.87±0.40	2.20±0.43	2.41±0.49
Total Bkgd	9.38±1.17	5.48±0.69	7.22±0.83	7.22±0.83
Observed	5	3	4	4

Figure 5.5 shows the 95% confidence level (C.L.) expected and observed limits on the $bg \rightarrow b(h/H/A) \rightarrow b\tau^+\tau^-$ production times branching ratio as a function of the Higgs mass. The observed limit was calculated for the sets of cuts that were found optimal for each signal mass. There are slight bumps in the observed limit distribution at Higgs masses of 120 GeV and 140 GeV. This behaviour can be explained by the roughness of the parameter optimization grid and abruptness of the changes in the optimal values of the paremeters. The bands indicate the $\pm 1\sigma$ and $\pm 2\sigma$ uncertainty on the expected limit.

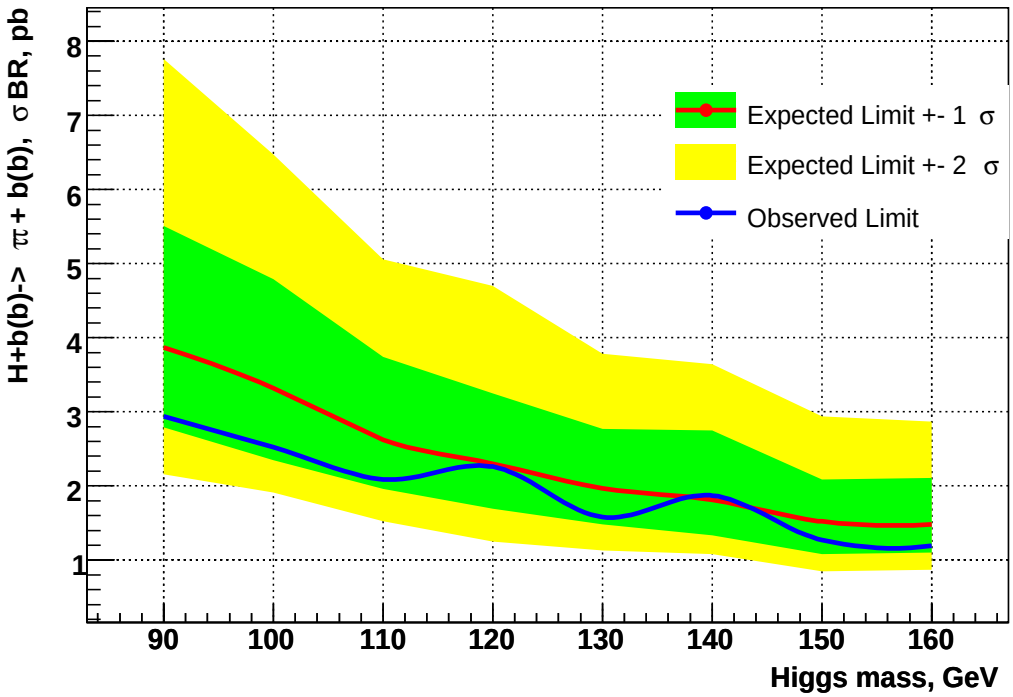

Figure 5.5. Limits on the $bg \rightarrow b(h/H/A) \rightarrow b\tau^+\tau^-$ production times branching ratio as a function of the Higgs mass.

5.2 Interpretation within the MSSM framework

Using the cross section limit for bh production [60], we can exclude regions of $(m_A, \tan\beta)$ parameter space in the MSSM. Beyond LO, the masses and couplings of the Higgs bosons in the MSSM depend (through radiative corrections) on additional SUSY parameters, besides m_A and $\tan\beta$. Thus, we derive limits on $\tan\beta$ as a function of m_A in two specific scenarios[2]: the m_h^{max} scenario (with the parameters $M_{SUSY} = 1000$ GeV, $X_t = 2000$ GeV, $M_2 = 200$ GeV, $\mu = \pm 200$ GeV, $m_g = 800$ GeV) and the no-mixing scenario (with the parameters $M_{SUSY} = 2000$ GeV, $X_t = 0$, $M_2 = 200$ GeV, $\mu = \pm 200$ GeV, $m_g = 1600$ GeV) [61]. The MSSM enhancement of the production cross sections, as well as the branching ratios, for the Higgs bosons are calculated over the mass range 90-160 GeV using the FEYNHIGGS program [62], version 2.5.1. Since at large $\tan\beta$ the A boson is nearly degenerate in mass with either the h or the H boson, their production cross sections are added. The results are shown in Figure 5.6.

[2]Both scenarios assume a CP-conserving Higgs sector.

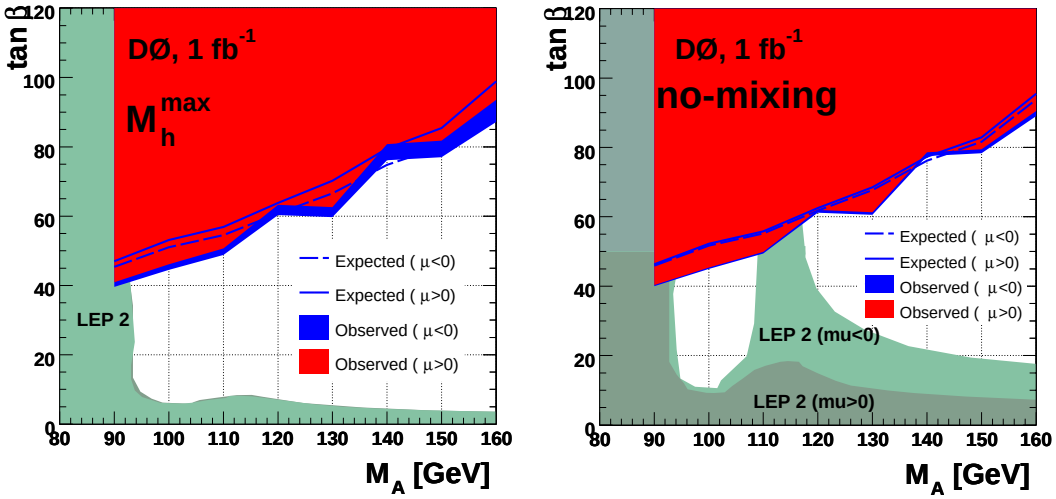

Figure 5.6. Excluded region in the $(m_A, \tan\beta)$ plane for the m_h^{max} (left) and the no-mixing (right) scenario of the MSSM, for $\mu = +200$ GeV and $\mu = -200$ GeV. Also shown is the region excluded by the LEP experiments.

CHAPTER 6

CONCLUSIONS

This analysis makes an effort to identify τ-leptons coming out of a decay of a massive particle state accompanied with one or more b-quark jets. These states include decays of Z-bosons and hypothetical Higgs bosons into τ pairs. The Higgs boson decay into τ's can be distinguished from that of the Z-boson through reconstructing the mass of the initial state by calculating the invariant mass of the decay products of both τ's, and looking for an excess of events over the sum of the backgrounds. Because the Higgs boson is a scalar and the Z-boson is a vector, differences in angular distributions can be exploited to separate decays of one from the other. However, insufficient statistics do not allow us to fully utilize this kinematic signature.

The Standard Model predicts the production of the Higgs bosons in substantially smaller numbers than is accessible in this search, see Chapter 2. On the other hand, the MSSM has regions of parameter space where the Higgs boson production is enhanced sufficiently so that it can be potentially identified at the DØ experiment.

The leading channels for the Higgs boson search are the decays of the Higgs into b-quarks and τ's, which have branching ratios of around 90% and 10%, respectively. The search in the first channel looks for as many as three b-quark jets in the event to at least keep the multijet QCD backgrounds at a manageable level, and is called the all-jet channel below. The second type of search is pursued by trying to identify

pairs of τ's, as it is done in a previous analysis, [39], or look for an accompanying b-quark jet, as is this analysis. In contrast to the $H \to \tau^+\tau^-$ search without the b-jet, this analysis is sensitive to a process of associated Higgs production with a b-quark, that has a smaller cross section. However, the important feature of this analysis has advantages for the search of the Higgs boson production at lower Higgs masses. It allows imposing looser cuts on the di-τ final state, and increasing the signal significance in the region, where the Higgs boson and Z-boson masses are close. At Higgs masses higher than the Z-boson mass, in this analysis, $t\bar{t}$ background starts to dominate, and introduces a large additional uncertainty. Methods of its suppression include developing a separate kinematic neural net[1].

Properties of τ-leptons, as reconstructed by the DØ detector, make them complementary to the b-quark jets. For example, a b-quark decay that has two to three tracks and a short secondary vertex decay length, see Section 4.1.7, would look similar to a τ-type 3, see Section 4.1.8. τ-types 1 and 2, on the other hand, cover the regions of the shower shape and track multiplicity parameter space that are not accessible to methods of conventional jet identification. Neither light-quark jets, nor b-quark jets have considerable misidentification rates as taus. The reasons for that are, that the regions of the τ and jet parameter spaces get even more significantly separated by applying the NN_τ. Also, methods of b-quark identification mostly rely on broader jets having higher track multiplicity with more energy deposited into the hadronic calorimeter, while taus are relatively narrow, one to three particle jets, typically with a significant fraction of energy going into the electromagnetic calorimeter.

A di-τ search with an accompanying b-jet, as this analysis, uses specific signatures of τ pair production. Decays of τ-leptons have to be, first of all, separated

[1]This background is not an issue in the $H \to \tau^+\tau^-$ analysis, see [39].

from the QCD multijet background. This is done with the help of the hadronic τ identification and reconstructing an isolated muon, see Section 4.4.1, which is localized almost back-to-back to the hadronic τ candidate. Their combination reduces the amount of multijet background from 92% at the preselection level to 12% after application of the NN_τ, see Tables 5.1-5.3. At this stage, large systematic errors preclude a sufficient sensitivity to the hypothetical Higgs signal. Requiring extra jets in the event, and subsequently a b-tag, keeps the multijet backgrounds almost at the same level while increasing the ratio $S/\sqrt{B}$, where S is the signal, and B is the sum of the backgrounds, as in Tables 5.1-5.3. The magnitude of this ratio roughly represents the sensitivity of the search. Levels of multijet backgrounds in the all-jet channel [3] are much higher due to the presence of irreducible backgrounds having as many real b-quark jets as come from the decay of the hypothetical Higgs signal plus the extra b-jets contained in the event. The all-jet analysis uses simulations of these backgrounds, which are hard to be properly modeled and introduce large systematic uncertainties. On the other hand, the muon-τ signature of this search is much cleaner and has a low fake rate from these backrounds. It allows retaining much more of the signal while achieving a necessary degree of background suppression. This is why the results of this analysis are comparable to those of the all-jet search despite the $9:1$ ratio in the cross section, and are complementary to them.

In the absence of a significant Higgs signal, a 95% confidence level limit is set on the production of the neutral MSSM Higgs bosons in association with a b-quark times the branching ratio of the Higgs decay into a pair of τ-leptons, ranging from ~ 3 pb at 90 GeV to ~ 1 pb at 160 GeV, which constrains the MSSM parameter $\tan\beta$, as in Figure 5.6.

Tables 5.1-5.3 show that the signal acceptances in this search are at a fraction of a percent level, which makes the SM Higgs boson search in this channel unfeasible

at the Tevatron even for a longer period of running, see [10]. However, the MSSM Higgs boson search has potential for either discovery or substantial reduction of the accessible MSSM parameter space if 4-8 times more data are accumulated.

Increasing the collision center-of-mass energy by 7 times, as will be implemented at the LHC, will increase the Higgs production cross section in this channel up to 1000 times, see [10], and will put both the SM and MSSM Higgs bosons within the range of accessibility of this search. However, searches at the LHC will be complicated by much higher multijet backgrounds coming out of hard scattering collisions dominated by gluon fusion, and also because of the higher rate of multiple interactions per beam crossing compared to the Tevatron.

Several factors can come into play at the LHC. Tau identification will have to be refined and will have to cut higher on the tau transverse energy. This will result into having more central and energetic taus, which will increase the tau time-of-flight before the decay. Sophisticated tracking tools like pixel detectors will allow better decay vertex resolution for both b-quark and, potentially, τ identification. Reaching the levels of background rejection observed at the Tevatron may necessitate constraining the Higgs boson signal parameters even more and reducing the signal acceptances. However, we expect a sufficient increase in the overall yield of the hypothetical Higgs boson events due to a significantly higher cross section despite the possibly lower acceptances.

BIBLIOGRAPHY

[1] Report of the Tevatron Working Group, hep-ph/0010338

[2] E. Galyaev, *Inclusive high-p_T b anti-b cross section measurement at $\sqrt{s} = 1.96$ TeV*, Notre Dame University, UMI-32-43287, FERMILAB-THESIS-2006-26, Aug 2006.

[3] DØ Collaboration, V. M. Abazov *et al.*, Phys. Rev. Lett. **95**, 151801 (2005).

[4] G. Altarelli and G. Isidori, Phys. Lett. B337 (1994) 141; J.A. Casas, J.R. Espinosa and M. Quiros, Phys. Lett. B342 (1995) 171; B382 (1996) 374.

[5] T. Hambye and K. Riesselmann, Phys. Rev. D55 (1997) 7255.

[6] K. Riesselmann, DESY-97-222 (1997) [hep-ph/9711456].

[7] H.E. Haber, Nucl. Phys. B (Proc. Suppl.) 62A-C (1998) 469484.

[8] K. Inoue, A. Kakuto, H. Komatsu, and S. Takeshita, Prog. Theor. Phys. 68 (1992) 927 [E: 70 (1983) 330]; 71 (1984) 413. Louis and S. Pokorski, Phys. Lett. B342 (1995) 180; F. Gabbiani, E. Gabrielli A.

[9] A. Haas, *A search for neutral Higgs bosons at high tan beta in multi-jet events from p anti-p collisions at $\sqrt{s} = 1960$ GeV*, Washington U., Seattle, FERMILAB-THESIS-2004-26, UMI-31-31160-MC Jun 2004.

[10] Dawson *et al.*, "Higgs-Boson Production with One Bottom-Quark Jet at Hadron Colliders", Phys. Rev. Lett. 94, 031802 (2005)

[11] V. Shiltsev, Status of Tevatron Collider Run II and Novel Technologies for Luminosity Upgrades, in: Proc. 2004 European Particle Accelerator Conference, Lucern, Switzerland, Vol. 1, 2004, p. 239.

[12] Tevatron Run II Handbook. URL www-bd/fnal.gov/lug/

[13] Linac Rookie book. URL http://www-bdnew.fnal.gov/operations/rookie _books/LINAC_v2.pdf

[14] Accelerator Concepts Rookie Book. URL http://www-bdnew.fnal.gov/operations/rookie _books/Concepts_v3.1.pdf

[15] Elvin Harms and Jim Morgan, "The Antiproton Source Rookie Book", (URL: http:/www-bdnew.fnal.gov/operations/rookie _books/Pbar_V1_1.pdf).

[16] V. M. Abazov *et al.* [D0 Collaboration], "The upgraded D0 detector," arXiv:physics/0507191.

[17] M. Arov, Fermilab DZero thesis, 2007

[18] R. Yarema, et al., Fermilab-TM-1892 (1994, revised 1996).

[19] P. Baringer, et al., Nucl. Instrum. Methods Phys. Res. A 469 (2001) 295.

[20] http://pdg.lbl.gov

[21] Cisco Systems, Inc. URL www.cisco.com

[22] A. Khanov, "HTF: histogramming method for finding tracks. The algorithm description." DØ Internal Note 3778, 2000.

[23] G. Borisov, www-d0.fnal.gov/global_tracking/talks/ 20030228/talk-adm-030228.ps

[24] P. V. C. Hough, *Machine analysis of bubble chamber pictures, in International Conference on High Energy Accelerators and Instrumentation* (L. Kowarski, ed.), (CERN), pp. 554556, 1959.

[25] R. E. Kalman, *A New Approach to Linear Filtering and Prediction Problems*, Transactions of the ASME - Journal of Basic Engineering 82 (1960) 3545.

[26] A. Schwartzman and C. Tully, "Primary Vertex Reconstruction by Means of Adaptive Vertex Fitting." DØ Internal Note 4918, 2005.

[27] H. Greenlee, "The DØ Kalman Track Fit." DØ Internal Note 2004, 2004.

[28] H. Greenlee, "The DØ Interacting propagator." DØ Internal Note 4293, 2003.

[29] L. Duflot and M. Ridel, "The CellNN algorithm: cell level clustering in the D calorimeter." DØ Internal Note 3923, 2001.

[30] S. Sumowidagdo, DØ Fermilab Thesis, 2007.

[31] G. C. Blazey, J. R. Dittmann, S. D. Ellis, V. D. Elvira, K. Frame, G. S., R. Hirosky, R. Peigaia, H. Schellman, R. Snihur, V. Sorin, and D. Zeppenfeld, *Run II Jet Physics*, in *QCD and Weak Boson Physics in Run II*, (Batavia), pp. 4777, 1999. hep-ex/0005012.

[32] E. Busato and B. Andrieu, "Jet Algorithms in the D Run II Software: Description and Users Guide." DØ Internal Note 4457, 2004.

[33] http://www-d0.fnal.gov/phys_id/jes/d0 _private/cb_material/p17_final/jes_note _v1.4.pdf

[34] T. Scanlon, "A Neural-network b-tagging tool." DØ Internal Note 4889, 2005.

[35] M. Anastasoaie, S. Robinson, and T. Scanlon, "Performance of the NN b-tagging tool on p17 data." DØ Internal Note 5213, 2007.

[36] T. Scanlon, *B-tagging and the search for neutral supersymmetric Higgs bosons at DØ*, PhD thesis, Imperial College, University of London, 2006. FERMILAB-THESIS-2006-43.

[37] V. M. Abazov, *et al.*, *First measurement of* $\sigma(p\bar{p} \rightarrow Z)xBr(Z \rightarrow \tau\tau)$ *at* $\sqrt(s) = 1.96\ TeV$ Phys. Rev. D 71, 072004 (2005), hep-ex/0412020.

[38] DØ collaboration, "Measurement of $\sigma(p\bar{p} \rightarrow Z)\cdot$ Br$(Z \rightarrow \tau^+\tau^-)$ with 1 fb^{-1} at $\sqrt{s} = 1.96$ TeV, DØ Conference Note 5484.

[39] V. M. Abazov, *et al.*, *Search for neutral Higgs bosons decaying to tau pairs in p anti-p collisions at* $\sqrt{s} = 1.96\ TeV$, FERMILAB-PUB-06-092-E, May 2006, Phys.Rev.Lett.97:121802,2006, hep-ex/0605009.

[40] DØ Collaboration, "Measurement of $p\bar{p} \rightarrow t\bar{t}$ in τ + jets channel", DØ Internal Note 5234-CONF, 2006. http://www-d0.fnal.gov/Run2Physics/WWW/results/prelim/TOP/T38.

[41] DØ Collaboration, V. M. Abazov *et al.*, Phys. Rev. Lett. 95, 151801 (2005).

[42] *http://www-d0.fnal.gov/Run2Physics/cs/skimming/skim_p17fixedPass2/doc_write.html*

[43] T. Sjostrand *et al.*, PYTHIA, Comput. Phys. Commun. 135, 238 (2001).

[44] S. Jadach, Z. Was, R. Decker, and J. H. Kuhn, *The tau decay library TAUOLA: Version 2.4* Comput. Phys. Commun. 76 (1993) 361380.

[45] M. L. Mangano, M. Moretti, F. Piccinini, R. Pittau, and A. D. Polosa, *ALPGEN, a generator for hard multiparton processes in hadronic collisions*, JHEP 07 (2003) 001, hep-ph/0206293.

[46] $http://www{-}d0.fnal.gov/goussiou/d0_private/btautau/prl/march/note.pdf$

[47] T. Adams, H. Sumowidagdo, DØ Internal Note 5416.

[48] DØ Collaboration, V. M. Abazov *et al.*, hep-ex/0410066.

[49] B. Tiller, T. Nunneman, DØ Internal Note 4660.

[50] P. Calfayan, DØ Internal Note 5329.

[51] M. Arov *et al.*, "τ identification with neural networks for pass2 data", DØ Internal Note 4773.

[52] S. Protopopescu and P. Svoisky, "τ identification with neural networks for p17 data", DØ Internal Note 5094.

[53] A. Harel, "Jet ID Optimization", DØ Note 4919.

[54] I. Anghel *et al.*, DØ Internal Note 5240.

[55] Y. Peters, M. Begel, E. Shabalina, and D. Wicke, "Study of the W+Jets heavy flavor scale factor in p17", DØ Internal Note 5406.

[56] A. Haas, S. Fu, "Search for $ZH \to llbb$ in p17 with NN", DØ Internal Note 5482.

[57] Certified JES for p17, DØ Internal Note 5382.

[58] S.Protopopescu and P. Svoisky, "Systematic uncertainty of τ identification neural network for p17 data", DØ Internal Note 5408.

[59] T. Junk, Nucl. Instrum. Methods Phys. Res. A **434**, 435 (1999).

[60] J. Campbell, R.K. Ellis, F. Maltoni and S. Willenbrock, Phys. Rev. D **67**, 095002 (2003), hep-ph/0204093.

[61] M. Carena, S. Heinemeyer, C.E.M. Wagner and G. Weiglein, Eur. Phys. J. C **45**, 797 (2005), hep-ph/0511023.

[62] S. Heinemeyer, W. Hollik and G. Weiglein, Comput. Phys. Commun. **124**, 76 (2000), hep-ph/9812320; FEYNHIGGS program: http://www.feynhiggs.de.